INTEGRATED CELLULAR BIOPHYSICAL MIGRATION APPROACH

By

SHEN-SHIU HUNG

A DISSERTATION PRESENTED TO THE GRADUATE SCHOOL
OF THE UNIVERSITY OF FLORIDA IN PARTIAL FULFILLMENT
OF THE REQUIREMENTS FOR THE DEGREE OF
DOCTOR OF PHILOSOPHY

UNIVERSITY OF FLORIDA

2013

To my family

ACKNOWLEDGMENTS

Recalling the six-year life in University of Florida, it was full with challenge and happiness. Here, I appreciate lots of advisors in my life. I would like to thank to my Ph.D advisor, Dr. Yiider Tseng. For his guidance and patience, I learn lots knowledge from him, not only in academic research, but also the attitude of life. Also, I am thankful to my committee members, Dr. Richard Dickinson, Dr. Tanmay Lele and Dr. Brandi Ormerod, for their valuable suggestions and expertise to make my work done well.

I wound put special thanks to my all group membranes for their assistance in many ways. In managing the lab, I wound thank for Jun Yin and Stephen's help to make the lab work well. In my experiment, Jacob Li, Kai Cheng, Jeff Kao, Ellie Fan, and Qian Peng work lots on my research. I also appreciate lots undergraduate's help, Weijie, Omar, Justin, and Jose. Without your help, these works cannot be done smoothly.

Further, I want to thank to my parents and my girlfriend for their love and support in these years. I wound share this achievement with you because this work could not have been accomplished without your support.

Finally, I truly appreciate everyone who helps me during these years.

TABLE OF CONTENTS

page

LIST OF TABLES

LIST OF FIGURES

LIST OF ABBREVIATIONS

CCD	Cellular centroid displacement
h-CCD	One hour cell displacement
m-CCD	One minute cell displacement
NCD	Nucleus centroid displacement
m-NCD	One minute nucleus displacement
R_x, R_y	Correlation between cell and nucleus in X and Y axes
R_{xy}	Summary of R_x and R_y
$NCD_{//}$	Projection of nucleus displacement on its related cell displacement
$NCD_{\perp}$	Nucleus displacement is perpendicular to the direction of CCD
CMPI	Cell migration potential index
Occur	Occurrence in regions
C-N	Cell and nucleus correlation profile
LD	Low cell density condition
MD	Medium cell density condition
HD	High cell density condition
PPMCC	Person product-moment correlation coefficient

Abstract of Dissertation Presented to the Graduate School
of the University of Florida in Partial Fulfillment of the
Requirements for the Degree of Doctor of Philosophy

INTEGRATED CELLULAR BIOPHYSICAL MIGRATION APPROACH

By

SHEN-HSIU HUNG

August 2013

Chair: Yiider Tseng
Major: Chemical Engineering

Cell migration has been considered as a critical and necessary component for cell physiology and pathology. However, current assessments to such cell activity are incomprehensive and greatly limit our understanding of cells through this aspect. Here, a cell migration analysis, utilizing the corresponding nuclear displacements as a reference to judge the effectiveness of the cellular displacement, is proposed to measure the cell migration potential. Through this approach, cell migration can be described much more comprehensive.

CHAPTER 1
INTRODUCTION

Cell Migration and Subcellular Activities

Cell migration is a fundamental cellular activity that includes detachment, protrusion and translocation, and has been studied since 1970 (Abercrombie et al., 1970; Abercrombie et al., 1971; Chen, 1981a; Chen, 1981b). Cell migration is typically characterized by a combination of three stages (Kaverina et al., 2002): 1) cells form lamellipodia and filopodia form substrate sampling to create or reinforce cell-substrate adhesions; 2) cells polarize via nuclear relocation, which is thought to help align the cytoskeletal components necessary for support and proper movement; and 3) cells detach their adhesions at the trailing end to release the cell from its former anchorage sites, allowing it to move forward. Considering the cycle of these three stages, there emerges certain unique migration patterns reflecting different migration strategies, such as random or persistent movement. Further, these motility phenomena can be explained by molecular mechanisms.

The regulation of integrin, which mediates cell adhesion to extracellular matrices and reacts to actin-cytoskeleton rearrangement, plays a critical role during cell detachment and anchorage during protrusion (Buck and Horwitz, 1987; Palecek et al., 1998; Tamkun et al., 1986). Hall, Ridley and Nobes identified that Rho GTPases, RhoA, Rac1 and Cdc42, play regulatory roles to control cytoskeleton remodeling (Nobes and Hall, 1995; Ridley and Hall, 1992; Ridley et al., 1992). This later led to progress in understanding the molecular mechanisms for migration-related subcellular activities – protrusion, detachment and translocation (Ballestrem et al., 2001; Machacek et al., 2009; Mullins et al., 1998; Ren et al., 1999). These studies construct an integrative

frame that tightly fuses subcellular activities and its underlying molecular mechanism together. This integrative concept started a new era in the study of cell migration.

The Importance of Cell Migration in Cell Biology

Cell migration is an essential cell activity for a broad range of physiological and pathological events, such as embryonic development (Richardson and Lehmann, 2010), wound healing following an immune response (Martin and Parkhurst, 2004) and cancer metastasis (Bacac and Stamenkovic, 2008).

In early embryo, three major parts of the germ, the endoderm, mesoderm, and ectoderm are classified by functional ability. Endoderm, in the internal layer of germ, is related to stomach, pancreas and thyroid development; mesoderm and ectoderm, middle and external layers of germ, separately mainly develop into muscle and neural crest. During the development process, chemotaxis-dominated cell migration plays an important role in tissue and organ development (Figure 1-1).

For example, the dorsal migration of endodermal in gastrulation of zebrafish is regulated by the Sdf1/Cxcr4 signaling pathway (Mizoguchi et al., 2008). Further, actin remodeling through Rac1 and Prex1 during endodermal cell migration has been suggested by Nodal signaling (Woo et al., 2012). Adhesion regulation, different peptide motif coatings, (Winklbauer, 1990) and PDGF chemtaxis (Nagel et al., 2004) all also play an essential role in the guidance of mesoderm migration in Xenopus gastrula. For muscle precursor cell migration, from mesoderm, the mechanism of EphA4/ephrin-A5 and Pax-3 are essential for well-developed muscle (Bober et al., 1994; Swartz et al., 2001). Furthermore, inhibition of Hif-1α in neural rest reveals a hindered migration and suggests a clue for epithelial to mesenchymal transition study (Barriga et al., 2013).

Thus, during embryonic development, a highly-coordinated cell migration defines the correct cell shape and positions in organogenesis, whereas defects from such activity will result in fatal damage (Kurosaka and Kashina, 2008).

Wound healing is a regular process in life, comprised of three basic phases: inflammation, proliferation and maturation (Figure 1-2). Inflammation happens immediately after the bleeding stops when fluids that contain plasma proteins, antibodies and blood cells are sent to wound regions. When inflammation is subsiding, fibroblasts start to enter and gather around the wounds and granulation tissue will be seen to gradually fill up the cavity. Subsequently, remodeling occurs where collagen fibers are laid down, nerve ends are re-grown and tissue rearranges itself. During the inflammation process, the immune system is activated and migrates to the wound region to work against extracellular materials. This migration mechanism was mainly suggested as being regulated by Rho GTPases and PI3K activities (Jones, 2000). Current research further suggests that PI3K inhibitors are potential agents in inflammation, especially in gamma and delta isoforms (Ellard et al., 2012; Ghigo et al., 2010).

Further, under PDGF regulation, fibro cells will move toward the wound region and release collagen, glycosaminoglycan, and collagenase (Lynch et al., 1987). In addition to PDGF, other growth factors, such as epidermal growth factor (EGF) and IGF-I, have also been suggested to play an essential role in cell migration during wound healing (Buckley et al., 1985; Lynch et al., 1989). Thus, the wound healing process involves not only growth factor-stimulated cell proliferation, but also chemokine-induced cell migration (Greenhalgh, 1996; Grose et al., 2002; Nath and Gulati, 1998).

In addition, metastasis, a process where cancer cells migrate from the original position to a distant position, mainly involved four steps (Figure 1-3). 1) Detachment from the original position, in which, the ability of cell-cell contact is greatly reduced. 2) Migration between cell-cell intervals. The cell has a more dynamic strategy to overcome the cell-cell contact issue during the migration, including MMP. 3) Intravasation, where the cancer cell reaches the blood or lymphatic vessels to penetrate into the circular system. And 4) extravasation, where under certain conditions, the cells penetrate through the wall of circular system and into the tissue or organ. Even though the cancer metastasis contains many different processes, cell migration is the critical process that changes cancer cells from their original anchorage positions to new positions to settle in a distal environment (MacDonald et al., 2002). Currently, it is thought that these migration processes adopt either mesenchymal-like or amoeboidal-like moving strategies to migrate (Wolf et al., 2003; Yoshida and Soldati, 2006).

Quantitative Approach to Cell Migration - Wound Disclosure Approach

Cell migration is essential in several physiology activities and the next research milestone is to systemically qualify these activities and integrate our understanding with various molecular mechanisms. To access cell migration, two quantitative strategies have been developed that view cells as simple objects. One approach is to use a small tip to scratch an artificial wound to monitor healing during wound recovery, and to note especially the recovery rate. This wound-like gap recovery process (generally called “wound-healing assay”) has been developed to study collective cell migration for over 40 years (Lipton et al., 1971; Todaro et al., 1965). This approach quantifies the progress of cell migration into a denuded area after a wound-like gap has been generated on a monolayer of confluent cells, mimicking the wound healing process in the body. Hence,

the different time extents required for a cell type to recover a wound-like gap under different extracellular stimuli (drugs) or intracellular alternations (mutations or expression level changes in proteins), can be used to identify disruptive factors on the wound recovery capacity of the tested cluster of cells (Lee et al., 2000).

Quantitative Approach to Cell Migration – Single Cell Trajectory

The other quantitative approach for studying cell migration is to use a mathematical method that captures cell trajectories. Through time-lapse microscopy, the distribution of cell trajectories can give direct visual information to suggest a migration pattern. Over a lengthy observation, cells can be easily seen as a single particle and its migration can be addressed through physical concepts. To investigate the trajectory information, mean square displacement (MSD) and its derived persistent random walk model, reflects the capacity for a cell to consistently move along a certain direction due to such a capacity may possess greater determination over the capacity of a cell to “hop” a greater displacement at a time interval. In 1970, a diffusion constant, D, of a two-dimensional random walk was suggested as a cell-migration characteristic when observed over a suitably long period (Gail and Boone, 1970). This study initiated an era of mathematical modeling of cell migration.

Dunn and Brown put forth a quantitative analysis with stochastic process on single-cell migration and emphasized several benefits of this quantitative analysis on cell motility: 1) a concise description of the motile process, 2) supplying a well communicated platform to make determinations, 3) introduction of a comprehensive discipline integrated with a mathematical model concepts (Dunn, 1983; Dunn and Brown, 1987). This mathematical concept was widely applied in cell migration studies, including modeling analysis of endothelial cell migration under chemotaxis (Stokes et

al., 1991) and adhesion mechanics during cell migration (DiMilla et al., 1991; Schmidt et al., 1993) and further in combination with statistical concepts to investigate cell migration (Dickinson et al., 1993).

Concurrently, another approach was pursued utilizing directionality, defined as the division of the final cellular displacement (D) during a time course by the accumulated transient displacements (T). This gives an alternative and simple method to study cell-movement patterns, whether persistence on direction or when random without directionality. If the D over T is close to 1, it suggests a persistent movement. Instead, if the ratio is far away from 1, this reveals a random movement. This approach was adopted by Yamada to examine PTEN downstream signaling, with Shc and Fak, and reveals different capacities for directional persistence (Gu et al., 1999).

With the linkage between cellular activities and underlying signaling pathways widely investigated (Huttenlocher et al., 1995; Oliver et al., 1994; Ridley and Hall, 1992; Theriot, 1994), the overall information and knowledge led to an integrated discipline platform to investigate cell migration from both molecular and physical viewpoints (Lauffenburger and Horwitz, 1996). These integrative concepts affected later research in cell migration and further clarified the connection between molecular mechanisms and endpoint cellular activities.

For example, a persistent zig-zag migration searching strategy in Eukaryotic cells was revealed when there is a deficiency in nutrients (Li et al., 2008). The stages of maturation (double positive or single positive) of developing thymocytes was quantitatively suggested by its migration capacity (Witt et al., 2005). Also, the persistence of cell migration quantified by directionality was suggested to be linked with

Rac1 activity (Pankov et al., 2005). More integrative approaches adopting microarray techniques that take abundant protein expressions into account have suggested that the migration capacity of cells is related to the expression level of HER2 proteins (Wolf-Yadlin et al., 2006).

These various approaches, however, have yet to reveal the relation between the contributed subcellular activities and the underlying signaling pathways. Therefore, these approaches cannot effectively unveil multi-factor induced pathological problems, such as those occurring in cancer. In addition, as cancer cells can adopt either mesenchymal-like or amoeboidal-like movement strategies to migrate (Wolf et al., 2003; Yoshida and Soldati, 2006), and mesenchymal-like movement is known to include several different cell migration patterns (Sahai and Marshall, 2003; Sanz-Moreno et al., 2008; Yamazaki et al., 2009), the contents of the subcellular activities assembling the cell migration patterns cannot be overlooked when pursuing cell-migration characterization.

The Relationship between Cell and Nucleus

Cell migration is a highly dynamic process, in which a fine force balance is required among all subcellular compartments, including the nucleus that occupies a significant portion of the cell volume and weight, to properly maintain the overall coherence of the cell when it migrates.

It has been understood that Rho GTPases are also involved in nuclear positioning during neuron development (Heasman and Ridley, 2008). Recent studies further suggest that the nucleus and the cytoskeleton have a tight physical association, which is a common cell phenomenon and not limited to neurons. It has been found that the actin network can form a “cap,” surrounding the apical nuclear and perinuclear

region to provide structural support to the nucleus that further guides the nuclear shape and regulates its position (Khatau et al., 2009).

Further, it has also been shown that the actin cap is composed of actomyosin filaments on the top nuclear region that connects to the nucleoskeleton (Khatau et al., 2009) through the LINC complex (Crisp et al., 2006), including nesprins and SUN proteins. Since the nuclear shape and movement, i.e., translocation and rotation, are tightly regulated by the nucleoskeleton-cytoskeleton connection (Lee et al., 2005), it is clear that the activities of Rho GTPases would also be involved in nuclear positioning during cell migration. Hence, a deeper study of nuclear movement, in particular the correlation between nuclear movement and cell movement, provides us another reference to understand cell migration.

Another Rho GTPases, RhoA, works locally at the trailing edge of cells where the nucleus has been observed to be located due to polarization. Since it was shown that the actin cap contains actomyosin filaments in the apical nuclear region and it is believed that the nucleus is connected to the cytoskeleton through the LINC complex (Crisp et al., 2006), nucleus movement could be controlled by RhoA activity through ROCK (Khatau et al., 2009). This hypothesis could be supported by the recent observation that the rearward movement of the nucleus was enhanced by the LPA treatment in the edge of wounds (Gomes et al., 2005) and the LINC complex could transmit a force to facilitate nucleus movement (Luxton et al., 2010).

Rho GTPases Signaling Pathway in Cell Migration

A multi-scaled cell activity such as cell migration is usually accomplished through a complicated signaling network controlled by proteins at certain nodes within the network (Gimona, 2008; Zhang et al., 2011). A nodal protein could exist that responds

to its collective upstream signals and distributes the ensemble activity accordingly to the pathways downstream from the nodal point. In the case of cell motility, the Rho GTPases family of proteins, RhoA, Rac1 and Cdc42, act as the three critical nodal proteins in cytoskeletal remodeling (Small et al., 1999). They usually work together to accomplish a cell-remodeling event, such as cell protrusion (Machacek et al., 2009) or cell division (Yoshizaki et al., 2003).

Studies using fluorescent resonance energy transfer (FRET) demonstrated that the activities of RhoA, Rac1 and Cdc42 reach a dynamic spatiotemporal harmony to coordinately achieve cell sampling (Machacek et al., 2009). However, the signaling crosstalk between RhoA and Rac1 is far more complicated (Burridge and Wennerberg, 2004). It has been suggested that the activity of Rac1 can activate RhoA for serum-starved cells (Ridley et al., 1992) and inhibit RhoA through the oxygen radical-p190RhoGAP pathway (Nimnual et al., 2003) or through downstream signals of Rac1 (Sander et al., 1999; van Leeuwen et al., 1999). Because RhoA and Rac1 activity have a specific local effect in cells and they mutually regulate each other through multiple signaling pathways (Scita et al., 2000), it is difficult to precisely predict overall cell behavior such as its migration status based only on the activity of one protein or even the activity profiles of a group of proteins that belong to the pathways of the Rho GTPases.

Despite elucidation over the past two decades and abundant knowledge about the structures and functions of proteins and the interactions among proteins that belong to the Rho GTPases' signaling pathways, a full understanding of overall cell migration at the cellular level is still unavailable.

Integrated Concept for Cell Migration

An integrative concept for studying cell migration emerged in the 1980s. This approach tried to use molecular mechanisms and mathematical modeling to decipher cell migration. From a molecular viewpoint, cell migration can be tightly managed from its collective subcellular activities, which can be smoothly explained by upstream molecular interactions, such as the dynamics of Arp2/3 (Mullins et al., 1998) or integrins (Tamkun et al., 1986) and actin remodeling, and further links to migration nodal proteins, such as Rho GTPases (Hall, 1998; Nobes and Hall, 1995; Ridley and Hall, 1992; Ridley et al., 1992). However, this complex signaling crosstalk cannot be effectively utilized to unveil certain issues in cell migration. For example, the feedback mechanism in molecular interaction is difficult to detect and may play a determining step in the regulation of cell migration. Mathematical modeling in cell migration may also overlook subcellular activities and cannot completely describe true migration behaviors.

Unfortunately, apart from qualitatively distinguishing movement patterns, there is no advanced approach relevant to biological aspects that can quantitatively analyze these movement patterns. Hence, an integrative approach is needed which has the capacity to decipher cell migration patterns to their subcellular activities. This type of approach can further connect subcellular activities with the underlying signaling pathways to fill the huge gap between cellular and molecular knowledge.

Closing this gap would have a tremendous impact on biomedical research, as evidenced by the highly cited numbers associated with those articles focusing on cell migration. Therefore, we are developing a tool to directly connect cell migration and its underlying signaling pathway to address the gap between molecular and cellular considerations. This approach utilizes individual nuclear displacements as indices to

screen out effective coupled cellular displacements as the contribution components for cell migration.

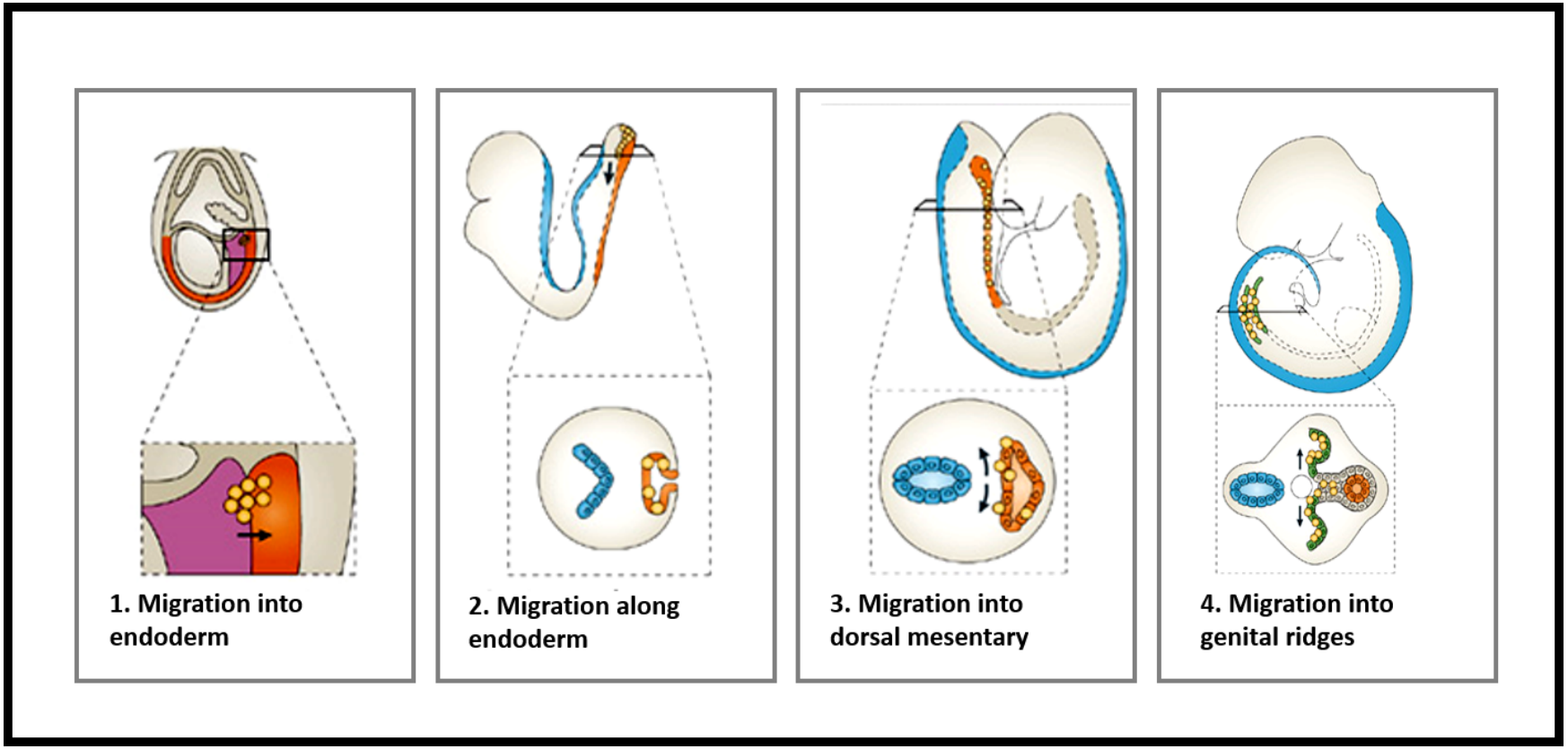

Figure 1-1. Cell migration in embryonic development (modified from Richardson, B. and Lehmann, R. (2010). Mechanisms guiding primordial germ cell migration: strategies from different organisms. Nature Reviews Molecular Cell Biology 11, 37-49).

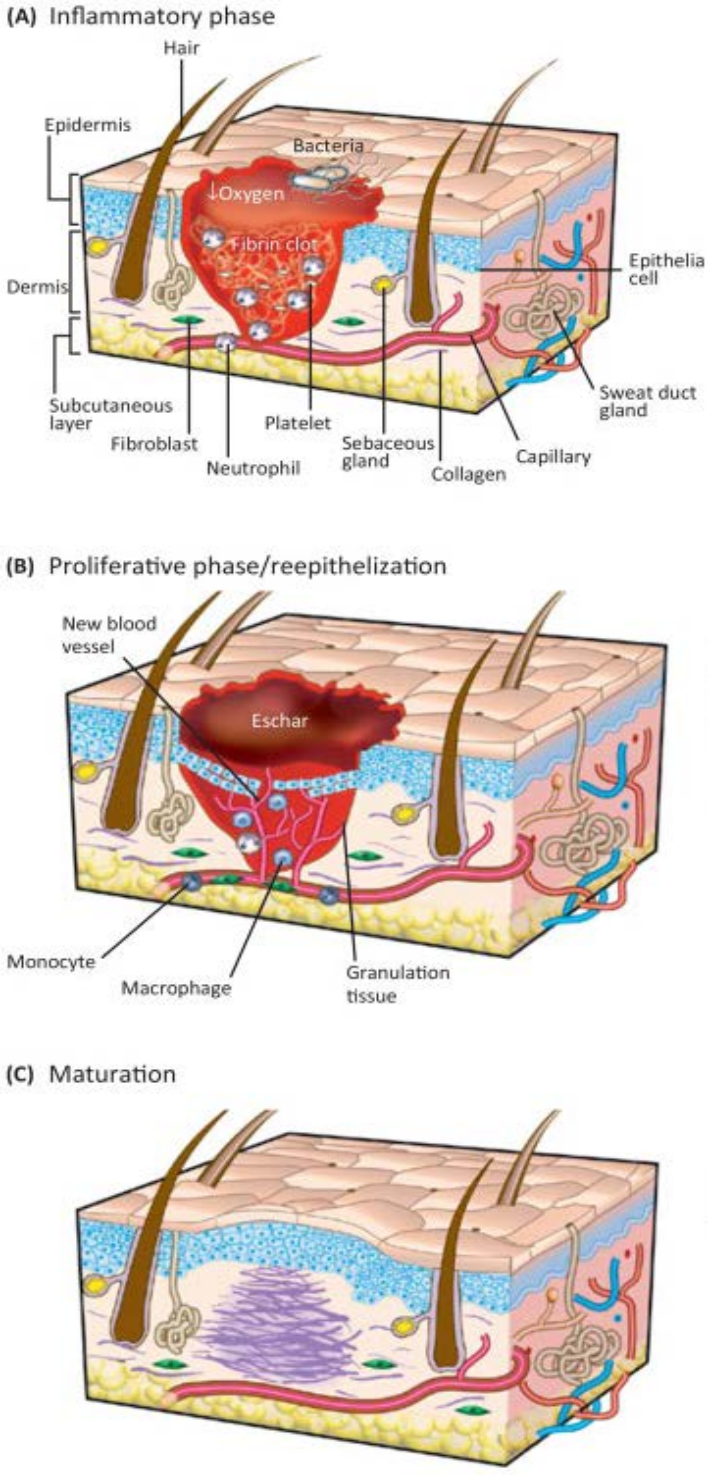

Figure 1-2. Cell migration in wound healing (adapted from Stein, C. and Küchler, S. (2013). Targeting inflammation and wound healing by opioids. Trends Pharmacol Sci 34, 303-12).

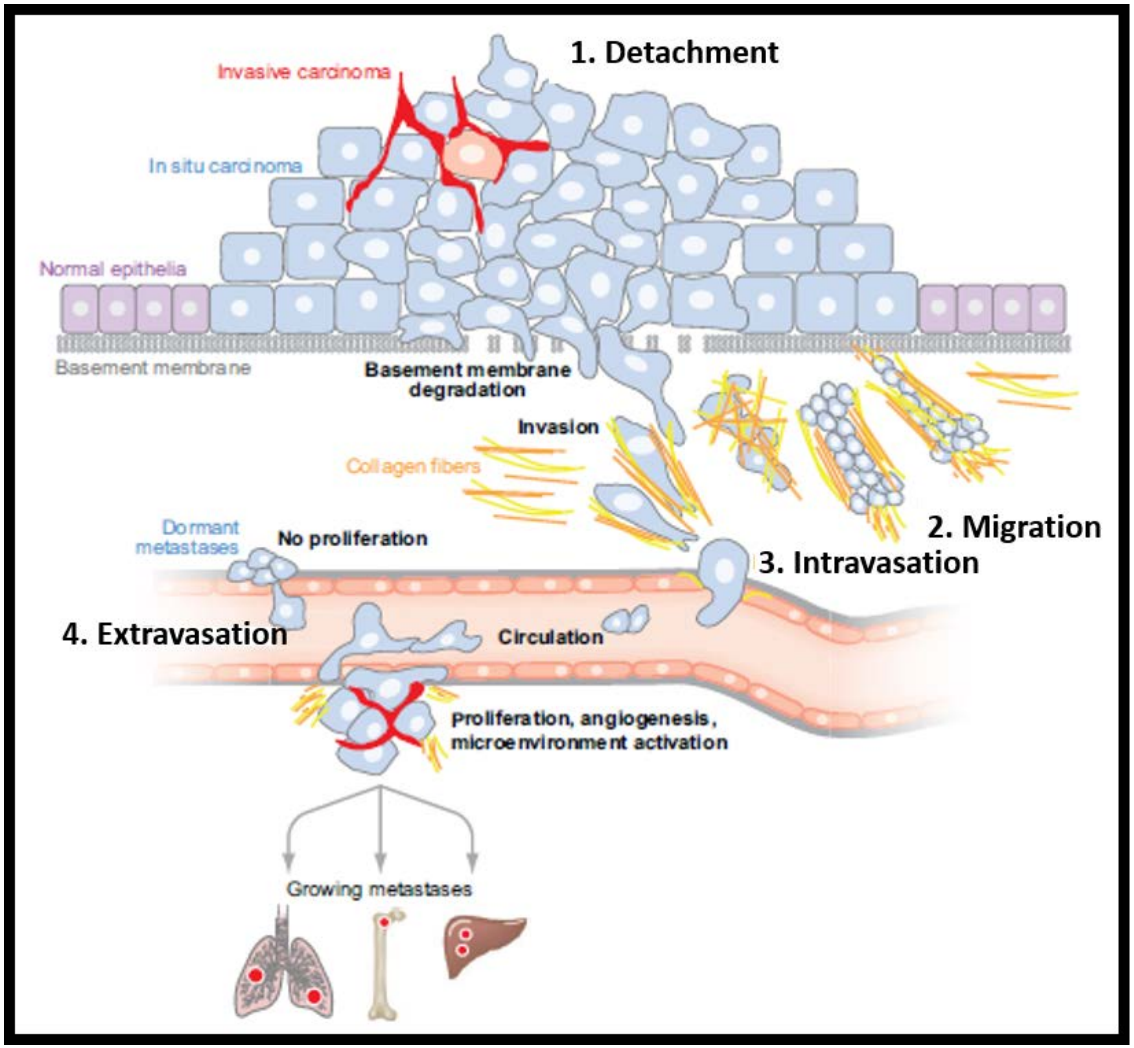

Figure 1-3. Cell migration in metastasis (modified from Bacac, M. and Stamenkovic, I. (2008). Metastatic cancer cell. Annual Review of Pathology-Mechanisms of Disease 3, 221-247).

CHAPTER 2
MATERIAL AND METHODS

Cell Cultures and Plasmid Transfection

NIH 3T3, Swiss 3T3 and human foreskin fibroblasts, MDA-231 cells (all purchased from ATCC, Manassas, VA), and MDA-231 derived E-cadherin-introduced stable cells (a generous gift from Denis Wirtz, The Johns Hopkins University) were cultured in DMEM containing 10% fetal bovine serum (FBS) and 1% L-glutamine (Mediatech, Manassas, VA). OSE-10, OVCAR-3 and SKOV-3 cells (generous gifts from Le-Ming Shih, The Johns Hopkins Medical Institute) were cultured in RPMI 1640 medium with 10% FBS, 1% L-glutamine and 1% penicillin-streptomycin (Mediatech). U-2 OS cells (ATCC) were cultured in McCoy's 5a medium with 10% FBS and 1% L-glutamine (Mediatech). Cultured cells were maintained in a humidified incubator at 37 °C and 10% CO2.

Plasmid Delivery and Drug Treatment

Cells were cultured to around 70% confluency before plasmid delivery. The transfection procedure was followed by a general protocol with Lipofectamine 2000 (Invitrogen, Carlsbad, CA). Plasmid, pRFP-R-CS (Origene, Rockville, MD) containing a red fluorescent protein gene, was used to confine the cell boundary. HuSH RhoGTPasse RNA interference constructs against RhoA, Rac1, and Cdc42 in the pRFP-R-CS plasmids were purchased from Origene. The other shRNA constructs were separately cloned in the vector, pLKO.1, to be against Tiam1 (target sequence, GACATCAAGGAGACAGACATC), HOXD10 (target sequence, GCAAGTGATCTGTAATCCCTA) and Arp2 (target sequence, GCAGTTATCCATTATAGGGAT) mRNA (from The Open Biosystems Expression Arrest

TRC library, Thermo Scientific, Waltham, MA) and were provided by the Interdisciplinary Center for Biotechnology Research (ICBR), University of Florida. The miRNA precursor hsa-miR-10b-5p was purchased from Invitrogen. For pLKO.1 shRNA plasmids and miRNA transfection, an additional one tenth of pRFP-R-CS was applied. Y27632 (Millipore, Billerica, MA) and Nocodazole (Millipore) were applied separately with 20 μM and 1 μg/ml (final concentration) on cell for 30 minutes before image taking. For the PI3K inhibitor, LY294002, and PI3Kδ inhibitor, IC87114, the working concentration were separately 5 μM and 0.1 μM, and both were purchased from Chemdea (Ridgewood, NJ). Afterward, the transfected cells were seeded on fibronectin (BD Biosciences, San Jose, CA)-coated glass bottom dishes for 24 hours prior to image acquisition. For live-cell nuclear stain, H33342 nucleus dye (Sigma-Aldrich, St. Louis, MO) was applied to the probed cells 5 minutes prior the image acquisition.

Microscopy and Image Acquisition for Single Cell

A Nikon TE-2000 microscope (Nikon, Melville, NY), equipped with a X-Cite 120PC fluorescent light source (EXFO, Ontario, Canada), a Cascade: 1K CCD camera (Roper Scientific, Tucson, AZ) and an on-stage incubator with a CO2 supplementary system (In Vivo Scientific, St. Louis, MO), was used to acquire cell and nucleus images. The image acquisition environment was kept at 10% CO2 and 37 °C during experiments.

The images of the red fluorescent cells and their corresponding blue fluorescent nuclei were sequentially acquired using a 20× objective lens (Nikon) at a frequency of one-minute per cycle. For CMPI determination, the cell and nuclear images were acquired for one hour and for persistence time calculation, the nuclear images were

acquired for ten hours with a 10X objective lens. The parameter settings for microscopy were 100 ms exposure time, 3×3 bin size and 25% light source power.

Wound Healing Assay

Cells were loaded to the fibronectin-coated glass bottom dishes at a loading density of 1×10^5 cells/per well with a culture-insert (Ibidi, Verona, WI) to create the standard width of a wound gap. When the cells were grown to confluence after 16 hours, the culture-insert was removed and the culture medium was replaced with fresh complete medium. Thereafter, the closure process of the wound-like gap was recorded every 30 minutes for 12 hours using differential interference contrast (DIC) microscopy. To examine the cell density effect on wound recovery, cells were loaded at 1×10^5, 3×10^5, and 5×10^5 cells/per well and the nuclei were stained using Hoechst 33342 to record nucleus images. Cell density was estimated by counting the number of nuclei in the field of view for each frame.

Single-cell Trajectory Analysis

The geometric centers of the imaged nucleus were determined using a custom-made program in the MATLAB platform (The Mathworks, Natick, MA). The nucleus trajectories were determined when the geometric centers from the same nucleus were linked by the order of the imaging acquisition time. Those nucleus trajectories further served as the source information to calculate persistence time using another custom-made program in MATLAB. The persistence time of each cell type was gained by fitting the mean square displacement, $< r^2 >$, with speed, S, using the persistent random walk equation: $< r^2 > = 2S^2P[t - P(1- e^{-t/P})]$ (Dunn, 1983; Othmer et al., 1988), where P and t are the persistence time and time interval, respectively.

Immunoblotting

Cultured SKOV-3, OSE-10, OVCAR-3, MDA-231, and U-2 OS cells were separately scraped from the tissue culture dishes and the suspensions were subjected to centrifugation. Then a lysis buffer (The Cytoskeleton, Denver, CO) was added to the cell pellets to lyse the cells. The lysates were subject to centrifugation to obtain the supernatant, for which a DC Protein Assay Kit (Bio-Rad Laboratories, Hercules, CA) was used to determine the total protein concentrations. The proteins samples were mixed with Laemmli Sample Buffer (Bio-Rad) with 100 mM DTT (Thermo Fisher Scientific, Waltham, MA) before being boiled for 5 minutes. Then 10 μg of total protein from each supernatant was individually loaded to a sample well of a 12% polyacrylamide gel for electrophoresis. The proteins in the gel were then transferred to PVDF membranes (Bio-Rad). The membranes were blocked by 5% nonfat milk in a TBST buffer and then separately probed with mouse-raised monoclonal E-cadherin (BD Biosciences) or N-cadherin (Invitrogen) antibodies, which were diluted 1,000 fold by TBST buffer, containing 2% nonfat milk. After washing with TBST buffer, these membranes were incubated with horseradish peroxidase (HRP)-conjugated goat anti-mouse IgG (Jackson ImmunoResearch, West Grove, PA), which was in 10,000× dilution. In the blotting, GADPH was chosen as the reference protein and immunoblotted by HRP-conjugated GADPH (Santa Cruz Biotechnology, Santa Cruz, CA), which was in 500× dilution. A Super Signal West Pico Kit (Thermal Scientific, Rockford, IL) was used to enhance the signal of probed proteins for 10 minutes. Finally, the protein amounts were measured by the signals and developed using Biomax XAR films (Carestream Health, Woodbridge, CT).

Rho GTPases Activity Assay

Cell lysate was prepared by scraping cultured cell from tissue culture dishes with the addition of a lysis buffer (Cytoskeleton, Inc., Denver, CO). After the lysate was centrifuged, the total protein concentration of the supernatant was accessed by a DC Protein Assay kit (Bio-Rad Laboratories, Hercules, CA). For individual Rho GTPases pull down assays, a 200-µg protein sample at 1 µg/µl concentration was mixed with 20 µg PAK-PBD-conjugated beads or 30 µg Rhotekin-RBD-conjugated beads (The Cytoskeleton) and further processed following the manufacturer's protocol. Then 2X Laemmli Sample Buffer (Bio-Rad) and 100 mM DTT (Thermo Fisher Scientific, Waltham, MA) were added to the protein samples or active Rho GTPases binding beads before the mixture was boiled for 5 minutes. Proteins were then separated using a 12% polyacrylamide gel and transferred to the PVDF membrane (Bio-Rad). The membrane was blocked by a 5% nonfat milk TBST buffer and separately probed with anti-mouse RhoA (Santa Cruz Biotechnology, Santa Cruz, CA), Rac1 (Millipore), and Cdc42 (Cytoskeleton, Inc.) antibodies, which were diluted by a 5% nonfat milk TBST buffer at 100×, 500× and 100× dilution, respectively. After TBST washing, the membrane was incubated with horseradish peroxidase (HRP)-conjugated goat anti-mouse IgG (Santa Cruz), in 2000× dilution by a TBST buffer containing 5% nonfat milk. A Super Signal West Pico Kit (Thermal Scientific) was applied for 10 minutes to enhance signals.

CHAPTER 3
RESULTS AND CONCLUSIONS

The Change in Consistence between the Cell and Its Coupled Nucleus Trajectories under Different Time Scales

For a long time period, during the cell translocation, there is a higher consistence between the nucleus and cell. The nucleus cannot be wiped out from the cell migration. This consistence, however, may be altered over a short time period. Take SKOV3, which is involved in invasive ovarian cancer, as an example (Figure 3-1). The green and blue lines separately represent the cell and nucleus trajectories, in which the red empty circle marked the end points of each particular time frame. High consistence between the cell and nucleus displacement is shown in the ten-hour trajectories. With the monitored time reduced, however, there was a reduced consistence as shown in the one-hour cell and nucleus trajectories. Further, while taking ten-minute time periods, significant non-consistence appears in the cell and nucleus trajectories. This indicates that carefully study of the consistence between cell and nucleus displacement at proper times may reveal more information about the regulation of sub-cellular activities during cell migration.

The Consistence between Cell and Nucleus Displacement Suggests Different Migration Patterns

Cell migration is a slow process; even a fast migratory cell, such as MDA-231, a breast cancer cell, generally still moves at a speed of less than 1 μm/min (or ~ 0.8 pixels/min in our camera setup). Hence, in this study, single cells and their coupled nucleus were alternatively recorded as a cycle at 1 frame/min temporal resolution for a one-hour span to compose the cellular and coupled nuclear trajectories. Accordingly, three outstanding trajectories of NIH 3T3 fibroblasts and OSE-10 ovarian cells were

analyzed since they displayed visually distinguishable patterns (Figure 3-2). Green and blue lines separately represent the cell and nucleus trajectories, in which the red empty circles mark end points for a 60-minute time period. There was a more straight-forward displacement and highly consistence between cell and nucleus displacement in NIH 3T3.

In contrast, random movement and reduced consistence between cell and nucleus showed up in OSE10. This implies that the consistence between the cell and nucleus could be a potential index for cell migration ability, and directional or hindered movement. To further examine the correlation between cell translocation and the consistence between cell and nucleus displacement. The average of a one-hour cell centroid displacement, < h-CCD >, of 20 randomly picked NIH 3T3 fibroblasts, calculated as 10.92 μm, was much greater than that of the same amount of randomly picked OSE-10 cells, which was 4.17 μm.

Highly Correlated Cell and Nucleus Reveals Longer Displacement

Previous results suggest that the consistence between cell and nucleus could help determine cell migration capacity. To access this issue, X and Y components of the cell and nucleus were examined through a correlation coefficient. Here, the person product-moment correlation coefficient (PPMCC) was used to judge the correlation between these two variables (cell and nucleus) and give a value, R. Meanwhile, the correlation between the minute cell centroid displacements, *m*-CCDs, and their nuclear counterparts, *m*-NCDs (NCD refers to nuclear centroid displacement, *m*-NCD is at a one-minute time interval), in the x- and y-coordinate direction were independently assessed using the correlation coefficient, denoted as R_x and R_y, respectively. Afterwards, the overall correlation between *m*-CCDs and *m*-NCDs could

be defined as $R_x + R_y$, or R_{xy}. In this regard, the mean value of R_{xy}, $< R_{xy} >$, for those randomly picked NIH 3T3 and OSE-10 cells were determined as 1.4175 and 0.4837, respectively. The results indicated that a cell type with a greater $< R_{xy} >$ might have a greater < *h*-CCD > as well.

The relationship between the Rxy and h-CCD at the level of individual cells within the same cell type was also separately examined. The Rxy value and the corresponding h-CCD value of each cell were plotted against the ascending ranking of its h-CCD magnitude among either NIH 3T3 fibroblasts or OSE-10 cells (Figure 3-3). Based on the observation that both Rxy and h-CCD have an inclined trend, a correlation between the coordination of cell and nuclear motion and cell migration capacity was clearly presented.

A Cell-Nucleus (C-N) Displacement Correlation Setup

Following the analysis, the correlation between a *m*-CCD and the coupled *m*-NCD was systematically investigated. Here, *m*-CCD, indicated by the green arrow, is set as a reference direction for its concomitant *m*-NCD (blue arrow), which is divided into two orthogonal components. One is projected on the *m*-CCD direction, denoted as *m*-$NCD_{//}$ (black dash arrow) and the other is perpendicular to the *m*-CCD direction (black dash arrow) (Figure 3-4, Left). In this case, the physical interaction between the cell and its contained nucleus is through the connection of the cytoskeleton, in which the correlation between the *m*-CCD and *m*-$NCD_{//}$ reveals direct meaning. Meanwhile, a *m*-CCD vs. *m*-$NCD_{//}$ plot can be used to describe a correlation between a *m*-CCD and its concomitant *m*-$NCD_{//}$ (C-N correlation) in cell migration events (Figure 3-4 Right). Red solid dots represent the *m*-CCDs and their coupled *m*-$NCD_{//}$s over a monitoring time of 60 minutes. Each cell was monitored for 60 minutes with a cell sample size of 20.

Biophysical Cellular Activities on C-N Correlation

Using the concept of mesenchymal migration, the likely relation of an instantaneous cellular and nuclear displacement could be roughly described and linked with a region of the CCD *vs*. $NCD_{//}$ plot (Figure 3-5). For example, when the trailing edge detaches, the rear of the cell abruptly loses its substrate adhesions and the cell centroid moves rapidly in the opposite direction of the detachment. The nucleus shows a similar centroid displacement because it is typically found at the rear of polarized cells before loss of adhesion, and is propelled forward along with the rest of the cell's trailing end. Hence, the area corresponding to positive cellular and nuclear displacement ($CCD < NCD_{//}$) in the CCD *vs*. $NCD_{//}$ plot was termed as Region *I*, which reflects the trailing end detachment event of cell migration.

However, abrupt forward cell movement due to the loss of trailing-end substrate adhesion may not always occur in a drastic fashion. Cells maintain several simultaneous substrate adhesions of various strengths and can manage forward motility while avoiding the rapid motion reflected in Region *I* of the CCD *vs*. $NCD_{//}$ plot. In this instance, the nuclear displacement is expected to be not as large as the cellular displacement, although the two could still be correlated and lie within the first quadrant of the CCD *vs*. $NCD_{//}$ plot. We termed this Region *II*, which reflects a forward moving cell that has some loss of trailing-end adhesions, but maintains several other connections with the substrate so that the overall nuclear displacement is damped ($CCD > NCD_{//}$).

Sometimes, migratory cells were found to exhibit a sampling behavior that involved the development of non-directed, broad, flat lamellipodia. Cells were slightly less elongated in this period of time and any transient protrusion affected the

immediately apparent direction of the CCD, but this sampling activity did not significantly displace the nuclear centroid. Therefore, the area of the CCD *vs*. $NCD_{//}$ plot near to the CCD axis, where the absolute magnitude of $NCD_{//}$ is very small, was assigned as Region *III*, which reflects the state of cell sampling.

Finally, since cells do not perpetually move in straight lines, but often turn or pause to reposition their nuclei, the remaining area of the CCD *vs*. $NCD_{//}$ plot in the second quadrant could be associated with turning behaviors. During a turn, the cell developed a protrusion with a significant perpendicular component to its previous trajectory, causing the greater portion of the NCD to be perpendicular to the CCD at that moment. Simultaneously, forward protrusions were in a state of retraction, and together the abrupt change in CCD direction caused an $NCD_{//}$ that was negative, or opposed to the CCD. Furthermore, cells were not always moving and were frequently stationary for a period of time during tracking. However, the nucleus was actively repositioned inside the cell during this time and exhibited $NCD_{//}$ that appeared to counteract the CCD, but this was in reality an effect of the small transient changes in the stationary cell boundary. Together, turning behavior and a more stationary status were classified into Region *IV* of CCD *vs*. $NCD_{//}$ plots, which is defined as most of the second quadrant. Here phi, ϕ, donates the angle turning from the first quadrant to the second quadrant.

Colorful Barcode Gives a Quick Screening

Cell migration is a continuous process, which was mixed up by different cellular activities, including protrusion, cell body translocation and detachment. To further understand the time sequence issue and have a quick screening tool for cellular behavior, a colorful barcode was designed. Videos of individual cells with their C-N correlations predominantly located on one specific region of the CCD vs. NCD// plot

should be the best resources to identify whether a region could be mapped to a genuine subcellular event of cell migration.

Hence, a barcode was designed for the purpose of quickly screening a special attribute of the C-N correlations of individual cells so that the corresponding cell videos can be used to associate the biophysical trait to a region. In a barcode (an example shown in Figure 3-6), each C-N correlation datum was presented as a bar, which was sequentially aligned by its occurrence time from left to right and placed at the row corresponding to the region it belongs to. The bars at the same row showed by the same color and the rows from top to the bottom presented Region I to Region IV, respectively.

Specific Subcellular Activity in Cell Migration

Thereafter, the barcodes of randomly picked NIH 3T3 fibroblasts were surveyed to identify special barcodes having the data mainly fall on a special region of the CCD vs. NCD// plot (Figure 3-7, first column, from left to right). Hence, the subcellular activity associated to a certain region could be elucidated from the corresponding video. As we mentioned before, cell migration is a slow process. With an increase in time interval, the outstanding features of these subcellular activities can be magnified. When the time lag was increased from 1 minute to 3 minutes (Figure 3-7, second column), a simple single color barcode sequence was revealed. The corresponding fluorescent images of the cell (left) and its coupled nucleus (right) at a 20-min interval (at 1st, 21st, 41st, and 61st minute) were shown from top to bottom and the boundaries (red, green, yellow and black traces, respectively) and centroids (black circles) of these images were indicated by arrows (red: cell, blue: nucleus) showing the cellular behavior progression (Figure 3-7, third and fourth column).

The cell trajectories from the stack images of the videos were further analyzed (Figure 3-7, fifth column). The trajectories of the cell (red) and nucleus (blue) for each region support arrows by the boundary sketches. This revealed that a cell mainly moves along a persistent direction with continual trailing edge detachments when the C-N correlations are mainly located on Region I, and with a continuous development of rich, dynamic lamellipodia features at both the front edge and the trailing edge when the data was mainly located on Region II. Further, the C-N correlations in Region III and IV correspond to a cell undergoing cell sampling and making a turn, respectively. From the arrows and the related trajectories, the biophysical meanings of the CN correlation located in each region were elucidated.

C-N correlation as A Cellular Parameter

To further carefully investigate these images, in a pure trailing edge detachment event we found that the amount of a $NCD_{//}$ is always greater than that of a coupled CCD; hence, a C-N correlation generated from such an event will locate in the region between 10° - 40° when using the spherical coordinate (e.g., the $NCD_{//}$ axis is along the 0° direction and the CCD axis is along the 90° direction) to describe the direction (Figure 3-8). A red cross and a yellow star separately represent the center of the nucleus and cell. The red and yellow arrows represent the magnitude and direction of nucleus and cell. For a pure protrusion event, the nucleus usually possesses a minimal forward movement ($NCD_{//} \sim 0$); while a considerable CCD is contributed by a sheet of lamellipodium and/or the extension of filopodia, which significantly is in the leading edge; therefore, C-N correlation data that corresponded to this event is located in the first quadrate and close to the CCD axis (~ 90°) (Figure 3-9). When cells perform pure

membrane ruffling, the quick fluctuation of the CCD value and direction makes the small NCD// swing between positive and negative values and their C-N correlations cover a small semicircle region with the center of diameter at the origin of the CCD vs. NCD// plot (Figure 3-10).

Always, cell migration is a continuous process and frequently more than one dynamic feature is present in a cell at a certain time (Figure 3-11). For example, a cell could have a predominant trailing edge detachment event occur simultaneously with a mild protrusion around the leading edge. In this case, the extra event will enhance or reduce the CCD value, respectively, but won't change its direction from a pure trailing edge detachment accompanied with cell body translocation; also the NCD// will retain around the same value. Hence, the C-N correlation presenting this mixed event will shift upward (with a same direction protrusion), up leftward (with a large side protrusion), and leftward (with small side protrusion) (Figure 3-11, Right).

In other cases, for example if the predominant feature during a time interval is the formation of cell protrusion, a minor trailing edge detachment will increase the CCD value. More importantly, it will add a non-negligible value to the NCD// because of the cell body translocation, which is the consequence of the detachment event. As a result, the C-N correlation will shift the location up rightward from that in the pure protrusion event (Figure 3-11, left).

Unlike a protrusion event, a sole significant retraction event almost always won't happen to a mesenchymal cell. As we observed from the large amount of samples, the retraction events are most frequently accomplished with a side protrusion; whereas the overall CCD most of the time will be redirected to an obtuse angle compared to the

NCD because the nucleus still carries the inertia to move toward the original direction. Hence a considerable size of negative NCD// is yielded accordingly to the new CCD direction. A less frequent case is when a predominant retraction event occurs coincidently with a trailing edge detachment event, in which the amount of CCD would be smaller than that of the retraction event alone. Since the NCD// is negative, the location of the C-N correlation is shifted toward a greater angle than where a pure retraction would be. In both cases, the C-N correlations with a predominant retraction event are located in the second quadrate ($\phi > 90°$) of the CCD vs. NCD// plot (Figure 3-12).

Cell Migration Potential Index (CMPI)

The time that a cell spends at each stage of movement would dictate how many points would lie in each corresponding region of the CCD vs. $NCD_{//}$ plot; thus, C-N correlations directly relate to the cell's migration behavior. Still, if migration is mainly concerned with effective cell displacement, then migration events like sampling or turning might only obscure the true potential of a cell to effectively move. From that perspective, a cell's migration potential might be better measured by focusing on events that effectively displace the cell. Since the C-N correlations located in Region *I* and *II* positively contribute to the R_{CN} of a migratory cell, and since a greater < *h*-CCD > is associated with a larger < R_{CN} >, the occurrences (denoted as *Occur*) and the average values of m-CCDs (< *m*-CCD >) for both regions were used to evaluate the cell migration potential using a weighted sum (Figure 3-13). Thus, only the portions of the cell trajectory that directly contributes to the overall cellular displacement are used to create the cell migration potential index (CMPI), defined as:

$$\text{CMPI} = \Sigma_{i\,=\,\text{Region } I,\ \text{Region } II}\ Occur_i \times \langle m\text{-CCD} \rangle_i$$

Here, we suggest a cell with a greater CMPI should migrate faster than a cell having a smaller CMPI. Three fibroblasts, NIH 3T3, Swiss 3T3, HF, and five epithelial cell lines, including one normal, OSE-10, and four cancer cell lines, SKOV-3, OVCAR-3, MDA-231, U-2 OS, were used to examine this approach (Table 3-1). The results indicated that MDA-231 had the highest migration potential ability followed by NIH 3T3, SKOV-3, OSE-10, Swiss 3T3, U-2 OS, OVCAR-3, and HF.

Cell Trajectories Was Set as a Gold Standard of Cell Migration

Cell migration potential predicts the migratory ability of a cell type during a reasonable time frame. Currently the most acceptable method to evaluate such potential for single cells is persistence time, in which the extracted results need to be ensured as being much shorter than the monitored time for the probed cell trajectories. Usually a persistence time study utilizes nuclear centroid trajectories that are documented at around a 10-hour length. With this time frame, the correlations between a 10-hour CCD (10*h*-CCD) and a 10-hour NCD (10*h*-NCD) for any cell type studied here are generally greater than 0.97 (data not shown). Hence, the average values of the 10*h*-NCDs (or < 10*h*-NCD >) were chosen here as the gold standard for the comparison of CMPI and persistence time.

The 10-hour nuclear trajectories (10h-NCD) of at least 10 cells from each of the 8 probed cell types exhibited distinct migration patterns (Figure 3-14). Each color trajectory represents a 10-hour cell trajectory where a red empty color represents the end point of each cell trajectory. A black solid circle represents the average of a 10-hour cell displacement. The 10-hour displacement distribution of each cell line is shown

below each trajectory pattern. The black solid circle represents the 10-hour displacement of each cell, where the black and red dashed line separately represent the mean and the standard value of the 10-hour displacement, respectively. For all cell types, most of the cells traveled a distance within one standard deviation of the < 10h-NCD >, but some do not, this suggests that the 10h-NCD is not a normally distributed parameter. Of the fibroblasts, NIH 3T3 fibroblasts demonstrated straighter trajectories and were one of the most migratory cell types. Human foreskin fibroblasts, in contrast, demonstrated trajectories that remained near to the initial position. Meanwhile, the trajectories of Swiss 3T3 fibroblasts were usually not as straight as that of NIH 3T3 fibroblasts, but still were more extensive than that of human foreskin fibroblasts. Similar differences in migration patterns were observed in the other 5 cell types probed in this study as well. Invasive MDA-231, SKOV-3 and U-2OS cancer cells migrated more directionally, while normal OSE-10 cells and non-invasive OVCAR-3 cancer cells appeared to have hindered mobility and did not demonstrate significant migration away from their initial positions.

Persistence Time Cannot Give a Stable Estimation on Cell Migration Ability

Among the 8 cell types, NIH 3T3 fibroblasts possessed the greatest < 10h-NCD >, followed by MDA-231, SKOV-3, OSE-10, Swiss 3T3, U-2 OS, OVCAR-3, and human foreskin fibroblasts, which had the lowest < 10h-NCD > value. The persistence time was gained from persistent random walk theory with mean square displacement and speed fit. The < 10h-NCD >, represented by the solid blue bar, of each cell type was plotted with an averaged persistence time, represented by the empty circle (Figure 3-15). The correlation between < 10h-NCD > and 10-hour persistence time had a correlation coefficient value (R-value) of 0.51. However, if the persistence time was extracted from

the same trajectories in a 9-hour period instead of 10-hour, the value could alter significantly for some cell types (such as SKOV-3 cells and Swiss 3T3 and human foreskins fibroblasts). In addition, the R-value between the < 10h-NCD > and the 9-hour persistence time also dropped to 0.39, indicating the instability of an approach using persistence time to evaluate cell migration.

CMPI, a Better Estimation on Mesenchymal Cell Migration

The cell migration potential ability of eight cell lines were suggested by CMPI (Table 3-1). In order to evaluate its ability, the < 10h-NCD > of the various cell lines were plotted against its CMPI. The linear fitting revealed a slightly stronger correlation value of 0.59 for all cell types. With further investigation of cell migration patterns, the correlation value was seen as increasing up to 0.87 if only considering the cell types that predominantly undergo mesenchymal migration (non-invasive OVCAR-3 cancerous cell types and normal epithelial OSE-10 have been excluded) (Figure 3-16). Hence, CMPI grants an improved estimation of a cell's 10-hour migration ability over 10-hour persistence times. Importantly, the CMPI only requires one hour of cell tracking. This provides a time advantage and also improves the probability that a cell would not migrate out of the frame during tracking, drastically increasing the sample size that can be acquired per hour.

The Stability of CMPI

To further investigate the variance and stability of CMPI, a random sample was picked up from each pool of the cell lines. For variance estimation, the average of CMPI was determined by choosing a random pickup sample size twenty times. Further, for stability, the sample size was increased up to 50. The CMPI of the top-three fastest migratory cell types (MDA-231, NIH 3T3 and SKOV-3) and one slow migratory cell type

(OVCAR-3) shows a diminishing standard deviation as the sample size is increased with the OVCAR-3 demonstrating the quickest convergence. This suggests that reliable CMPI values could be attained quickly and easily to rapidly assess the migration potential of a cell type (Figure 3-17).

In conclusion, CMPI can quantitatively evaluate the change in cell migration without the interference of cell-cell interactions. In contrast to persistence time, which simply provides a quantity to distinguish cell migration without integrating direct insight about the cell migration process, the C-N correlation defines a solid foundation to characterize a cell migration pattern. A detailed cell migration mechanism can be described by C-N correlations, which can be further linked to the molecular mechanisms that contributed to the cellular activities, such as lamellipodia formation, actomyosin contraction and cell polarity. This will significantly promote the current effort in taking a systems approach to biomedicine and to appropriately describing the intrinsic cell migration potential for different cell types.

Collective Approach, Wound Closure Assay, Used to Judge Cell Migration and Consistency with CMPI

To evaluate whether the CMPI is an effective index to describe a cell's migration potential, five different non-fibroblast cell types, MDA-231, OSE-10, OVCAR-3, SKOV-3, and U-2 OS cells, were subjected to the wound-like gap closure assay (Figure 3-18, top). Cells were loaded with optimal density to reach the confluent monolayer cell after 12 hour in two wells of insert, which has a 500-μm gap between two wells. Ten hours after a 500-μm gap was created in a confluent cell monolayer, the order of the average width of the remaining gap for an individual cell type from the smallest to the largest was MDA-231, SKOV-3, OSE-10, U-2 OS, and OVCAR-3 (Figure 3-18, bottom). The

recovery percentage was calculated by the difference between the original gap area and remaining area divided by the original gap area. This recovery order was consistent to that of CMPI, calculated from the C-N correlation data of each cell type over a one-hour period (Figure 3-19).

Further, the gap recovery rates during the gap closure process were not constant, as revealed from the gap recovery plot. When the slopes of each gap recovery curve were calculated by its 2th, 6th and 10th hours, and normalized by the initial slope, it showed that the evolution of the slopes could be used to classify the cell types into two groups: MDA-231, OSE-10 and U-2 OS cell types, which had their slopes decline; and SKOV-3 and OVCAR-3, which had their slopes incline (Figure 3-20).

Cell-Cell Interaction in Wound Closure approach Can Be Illustrated by CMPI

The most likely reason for the change in the gap recovery rates should be from interference of the cell-cell interactions. On the one hand, cells in a crowd could push neighboring cells toward the void space, therefore enhancing the cell migration rate. On the other hand, the activities of cadherin family proteins could produce different degrees of interaction strength in hindering cell migration (Kim et al., 2005; Panorchan et al., 2006). To better illustrate the effects of cell-cell interactions, the percentages of gap recovery of the 5 cell types at different time extents were plotted against their CMPI (Figure 3-21). Curve fitting revealed that the regressions were consistently improved by a longer time extent, in which the influences of cell-cell interactions were gradually downplayed. Furthermore, during the wound-like gap closure process, MDA-231 cells moved toward the void via a single-cell format, while the OVCAR-3 cells moved as a group (Figure 3-22). The other three cell types mainly moved in a similar pattern as the

OVCAR-3 cells, but occasionally displayed single-cell migration. These indicate the cell-cell interaction plays a critical role in wound closure.

To further examine the cell-cell contact issue, western blotting using antibodies against the cadherin family proteins, E- and N-cadherin, could provide an explanation for the difference in the migration patterns among the five cell types. The results suggested that all cell types, except MDA-231, contain cadherin proteins that can initiate cell-cell interactions (Figure 3-23).

Also, in order to demonstrate that cell-cell interactions through the cadherin proteins could conceal the intrinsic cell migration potential, a wound-like gap closure experiment was applied again to a stable MDA-231 cell type derivative, in which E-cadherin was recombinantly introduced into the MDA-231 cells. The discrepancy between the MDA-231 derivative and its original counterpart for the gap closure at the same time frame clearly addressed the effect of cell-cell interactions on the gap closure process (Figure 3-24). The recovery percentage at 10 hours dropped to around 50% due to the introduction of E-cadherin.

Cell Density, another Potential Issue for Wound Closure Approach

The cell density effect on wound-like gap closure was also evaluated. All different cell densities (from high, medium to low density) reached a confluent monolayer cell before the insert was removed. Two ovarian cell lines were chosen, OSE10, the normal epithelial ovarian cell, and OVCAR-3, the benign ovarian cancer. The results showed that OVCAR-3 cells in a more dense state possess a better wound-like gap closure effect than the otherwise faster moving OSE-10 cells (Figure 3-25, left). The nucleus was dyed with H33342 and fluorescent images of the nucleus was used to represent the

condition of cell density (Figure 3-25, right). These results suggest that the wound closure approach should be processed with well density control.

Taken together, the involvement of cell-cell interactions and cell-density in a wound-like gap recovery assay can complicate the interpretation of the experimental results and obscure a simple explanation. In contrast, CMPI provides a compatible and much clearer cell migration index that is assessed in a single-cell context without the interference of cell-cell interactions. Hence, CMPI can fully replace the wound-like gap recovery assay to probe the change in the intrinsic cell migration capacities between a cell type and its derivative.

CMPI Has Distinct Advantages over Existing Migration Evaluations

Taken together, the involvement of cell-cell interactions and the physical crowding effect in a wound-like gap recovery assay can complicate the interpretation of the experimental results. Meanwhile, persistence time provides a quantity to distinguish cell migration without integrating direct insights about the cell migration process. In contrast, CMPI is assessed in a single-cell context without cell-cell contact to deliver a compatible cell migration index with much clearer migration details.

Hence, CMPI can be used independently and in a complementary manner with the wound-like gap recovery assay to obtain the full spectrum of migration information, including intrinsic cell migration potential and the effect of cell-cell interactions on collective migration for various cell types. The C-N correlation during cell migration also defines a solid foundation to characterize cell migration patterns thru a detailed description of the cell migration mechanism, which can be further linked to the molecular mechanisms that contributed to the cellular activities, such as lamellipodia formation, actomyosin contraction and cell polarity. Hence, this will significantly promote

the current effort in taking a systems approach to biomedicine that appropriately describes the intrinsic cell migration potential for different cell types.

A Cellular Parameter for Distinguishing Cells

Co-existing cellular dynamic features represented by occurrence and time-sequence comprises the cell migration patterns. For example, a ballistic cell migration is assembled with a sequence of continuous leading-edge protrusions and trailing-edge detachments, working harmonically to allow a cell body to move forward. Thus, the C-N correlation profile of a ballistic cell migration will have C-N correlation data that is mainly distributed in the first quadrate of the CCD vs. NCD// plot. Cell sampling is composed of membrane ruffling, pure protrusion and pure retraction. Hence, C-N correlation data for cell sampling is primarily distributed along the CCD axis of the CCD vs. NCD// plot. During a cell turning event, the sequence evolves from a lamellipodia-rich, directional migration to predominant cell sampling events, and ends up with another directional migration in a different direction. During this process, retraction will be a predominant event in the mixture of dynamic features at certain time so that the occurrence of the C-N correlations at the time will be located in the second quadrat away from the CCD axis. Hence, a turning event always contains a sequence of C-N correlations switching back and forth between the first and second quadrate, but away from the CCD axis. Taken together, the distinct distribution pattern of C-N correlation data of a probed cell type can be mapped with its unique migration pattern once ample amounts of C-N correlations are available.

We further tested whether the C-N correlation profile can serve as a cellular parameter for a cell type. First, two independent groups of NIH 3T3 fibroblasts, 50 cells each, were probed for one hour at the same culture condition to construct their C-N

correlation profiles. Since the C-N correlations for similar cellular dynamic features are located around the same conical region classified by similar angles in the CCD vs. $NCD_{//}$ plot, the Student T-tests were subjected to these two profiles to compare the occurrence (Figure 3-26, Top) and the CCD quantities (Figure 3-26, Bottom and Insert) by different distribution angles. The results suggested that these two profiles are highly consistent.

We further constructed the C-N correlation profiles for 8 different cell types (3 fibroblasts: NIH 3T3, Swiss 3T3 and human foreskin fibroblast, 3 mesenchymal invasive cancer cells: MDA-231, U2-OS and SKOV3, 1 epithelial non-invasive cancer cell: OVCAR-3, and 1 normal epithelial cell: OSE-10) and the occurrences of these C-N correlations against the distribution angles were compared by pairs (Table 3-2). The results suggested that eight pairs of those cells have s similar angle distribution for their C-N correlations. Hence, the quantities of the CCDs of the C-N correlations were further cross-compared by their angular groups using student T-tests, which showed that, even two cell types might have the same angular distribution, and the magnitude of the CCD in those C-N correlations were still different (Figure 3-27). It is noteworthy that the main dynamic features of Swiss 3T3 fibroblasts, which are protrusion (red crosses), and OVCAR-3 cells, which are membrane ruffling (blue crosses), can be easily distinguished by the averaged CCDs along 90° as discussed in the previous section (Figure 3-28).

Cellular Activities Disrupted by Drug Treatment Alter the C-N Correlation

To support this concept, we separately applied Y-27632, which inhibits ROCK and further prevents actomyosin contraction, and nocodazole, which disrupts microtubules, and used a RNA interference technique on knockdown Arp2/3, which is

essential for lamellipodial formation, in NIH 3T3 fibroblasts. The effects of these on NIH 3T3 fibroblasts were studied comprehensively. Hence, we examined whether the changes in the dynamic features of NIH 3T3 fibroblasts under these conditions can be reflected in their C-N correlation profiles. For each condition, twenty cells were documented to construct the corresponding CCD vs. $NCD_{//}$ plots.

When the CCD vs. $NCD_{//}$ plot of the NIH 3T3 fibroblasts under the presence of Y-27632 to inhibit the actomyosin contraction was compared to that of the normal NIH 3T3 fibroblasts (Figure 3-29), the C-N correlations locating on the area where the dynamic features associated to the actomyosin contraction, such as the trailing edge detachment or large-angle cell turning, were completely depleted from their original positions. In addition, the magnitudes of the CCD of the C-N correlations mapped to the protrusion and retraction regions was decreased, suggesting that the leading edge protrusive event after the contraction force is diminished, and tested at a one-minute interval, is not as aggressive as the normal condition. It was reported that the inhibition of ROCK causes the fibroblasts to increase membrane ruffling in the active lamella (Omelchenko et al., 2002), but the focal adhesions and stress fibers are unable to form to stabilize the protrusion (Rottner et al., 1999; Uehata et al., 1997). Hence the small magnitudes of the CCD along the CCD axis were in agreement with the literature and mapped well with the ruffling events.

Further, the knockdown of the expression level of Arp2/3 impeded lamellipodial formation, but still allowed filopodial formation, which is critical for lamellipodial formation, and the knockdown of the expression level of Arp2/3 in the NIH 3T3 fibroblasts will demolish lamellipodial formation. A comparison of the locations of the C-

N correlations in the CCD vs. $NCD_{//}$ plot between the normal cells and the cells with the Arp2/3 knockdown indicated that the C-N correlation data disappears from the protrusion and retraction region (Figure 3-30); hence, it suggested again that the distribution profile of the C-N correlations in the CCD vs. $NCD_{//}$ plot can faithfully describe the dynamic activities of cells (Suraneni et al., 2012).

Further, after nocodazole disrupted the microtubule-cytoskeleton in the NIH 3T3 fibroblasts, the occurrence of the C-N correlations declined in the locations associated to the trailing edge detachment event and increased in the locations associated to the protrusion and retraction events; also, the CCD magnitudes of the C-N correlations associated to the protrusion and retraction were elevated (Figure 3-31). This observation strongly supported the conclusion of the study suggesting that Calpain-6, a microtubule-stabilizing protein, is released from the surface of a microtubule and interacts with guanine nucleotide exchange factor, GEF-H1, to activate Rac1 upon microtubule de-polymerization at the leading edge of NIH 3T3 fibroblasts (Tonami et al., 2011).

The Contribution of This Work

Cell migration has attracted interest since 1970; however, the current measurement approach, which is irrelevant to biological aspects, is incapable of *qualitatively* analyzing these moving patterns and can only *quantitatively* assess them. Furthermore, the role played by the nucleus in regulating cell migration is still obscured since the importance of the nucleus in actin remolding has been emphasized.

In this work, a relationship was successfully identified between physical measurement during cell migration and the underlying signaling of subcellular activities, which offers a multi-scale perspective on cell migration. This approach avoids

overlooking the essence of subcellular activities during cell migration since this information has been overlooked by the other two quantitative approaches for decades. Through this bridging, a straightforward analysis can be achieved that connects physiological activities and molecular reactions.

Furthermore, a new quantitative approach for estimating cell migration capacity was extracted to enrich the current approaches. A substantial amount of cell migration capacity can be deciphered in minutes instead of hours, and at a high level of quality. This quantitative information emphasizing the essence of these cellular characteristics during cell migration promotes our recognition of cell migration. Moreover, through this correlation, unique migration pattern assembled by subcellular activities which represented different cell lines can be used to distinguish between cells, especially in cancer cell research.

It is difficult to directly access molecular changes in living cells and to clarify the simple role of protein under complex signaling crosstalk; however, this work may provide some clues to estimate the protein activity level, because these characteristic are directly contributed from their upstream molecular mechanism. Furthermore, the regulatory nodal protein in signaling pathways can be elucidated.

This study sets forth a framework of “top-down integrative biology” that only monitors cell and nucleus movements to understand the status of the controlling pathways. Through such integrative work, a new era in cell biology can be expected.

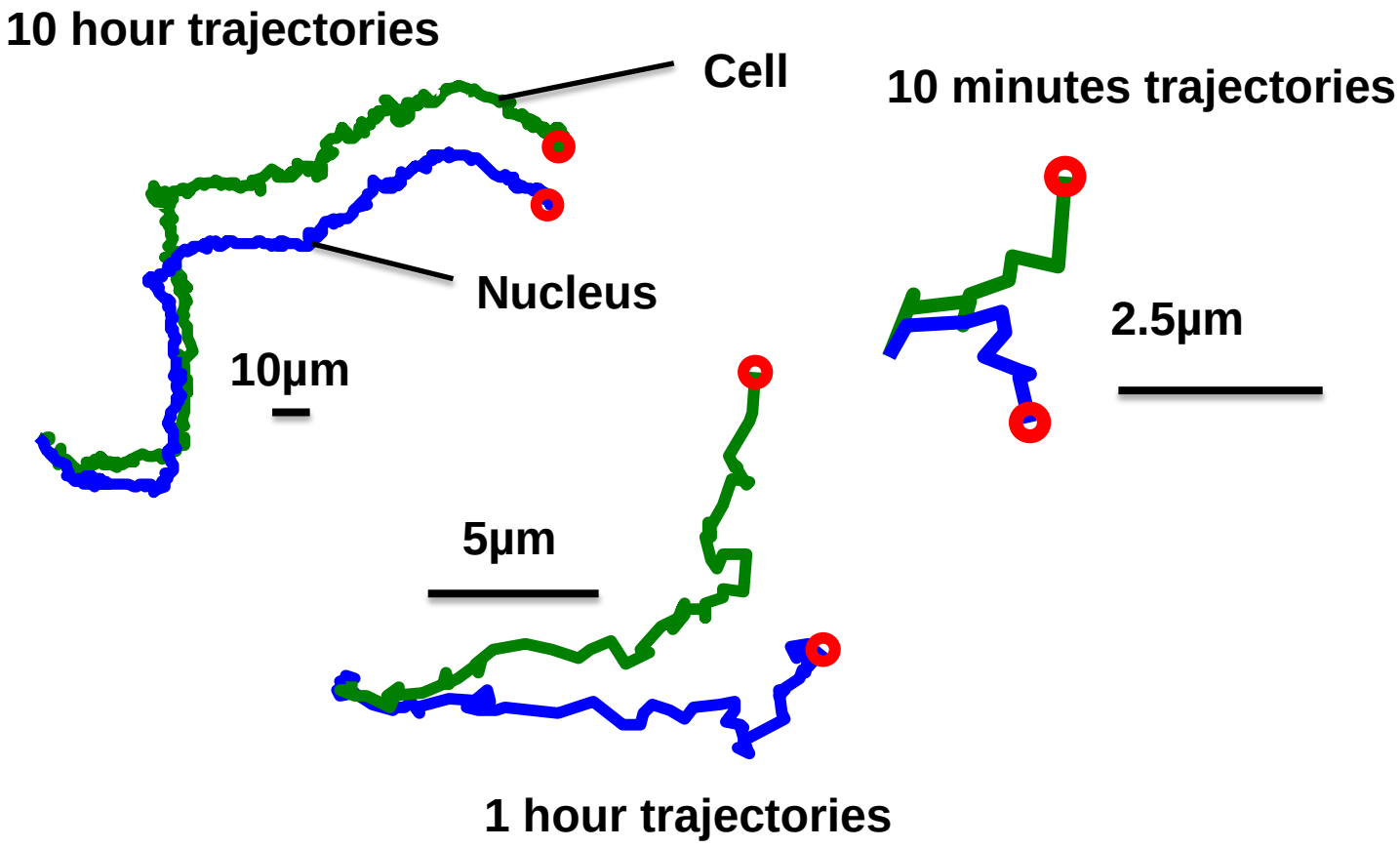

Figure 3-1. The consistence between cell and nucleus trajectories at different time period. A highly correlation exists between 10 hour cell and nucleus trajectory (Left panel). With the time scale reduced to 10 minutes, the consistence between cell and nucleus is significant decreased (Right panel).

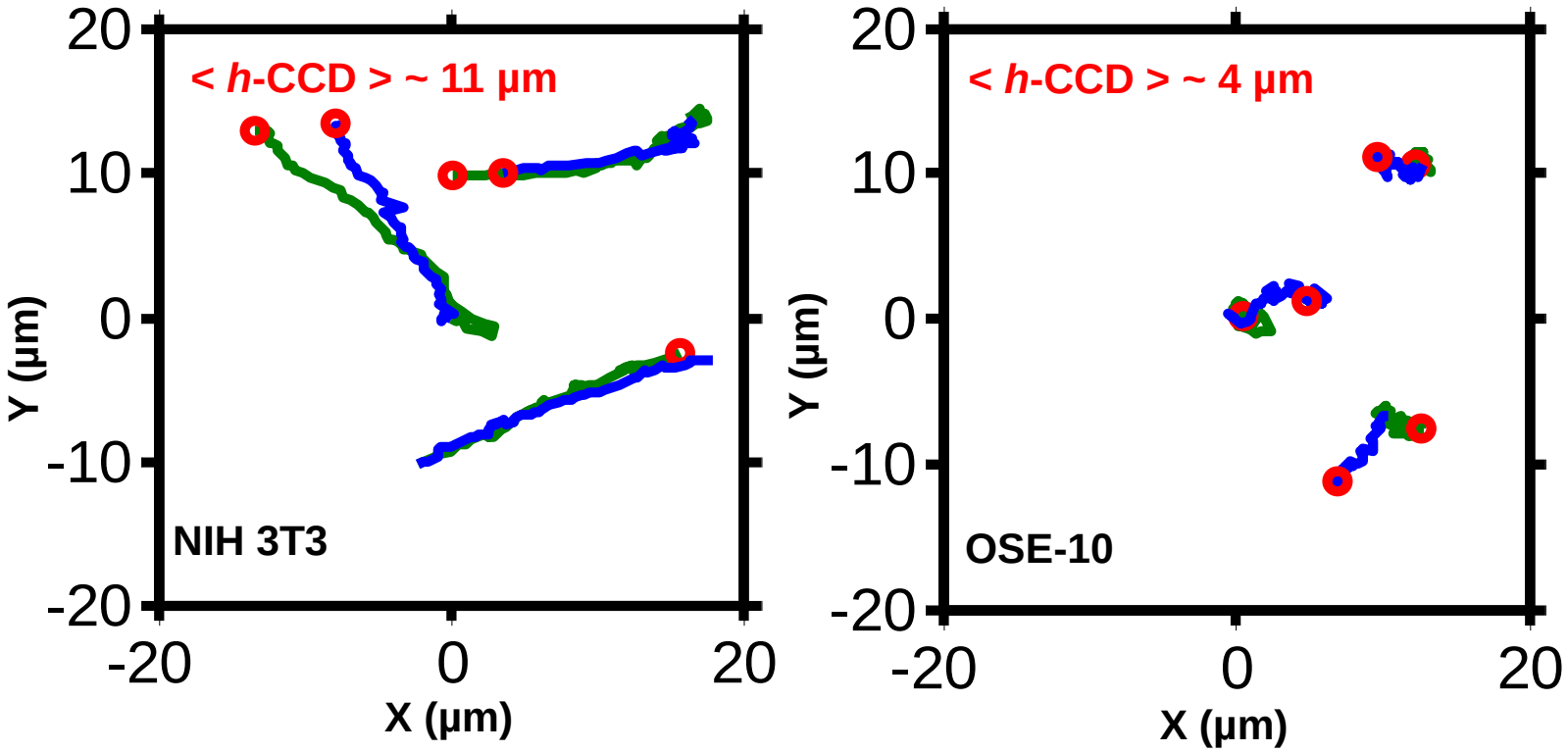

Figure 3-2. Consistence of cell and nucleus trajectories suggests longer cell displacement. NIH 3T3 revealing higher cell and nucleus consistence has longer displacements. Instead, OSE-10 having less consistent in cell and nucleus results in short translocation. Three representing cells were used for NIH 3T3 and OSE-10 separately. Average displacement of each cell line was calculated from 20 random pickup samples.

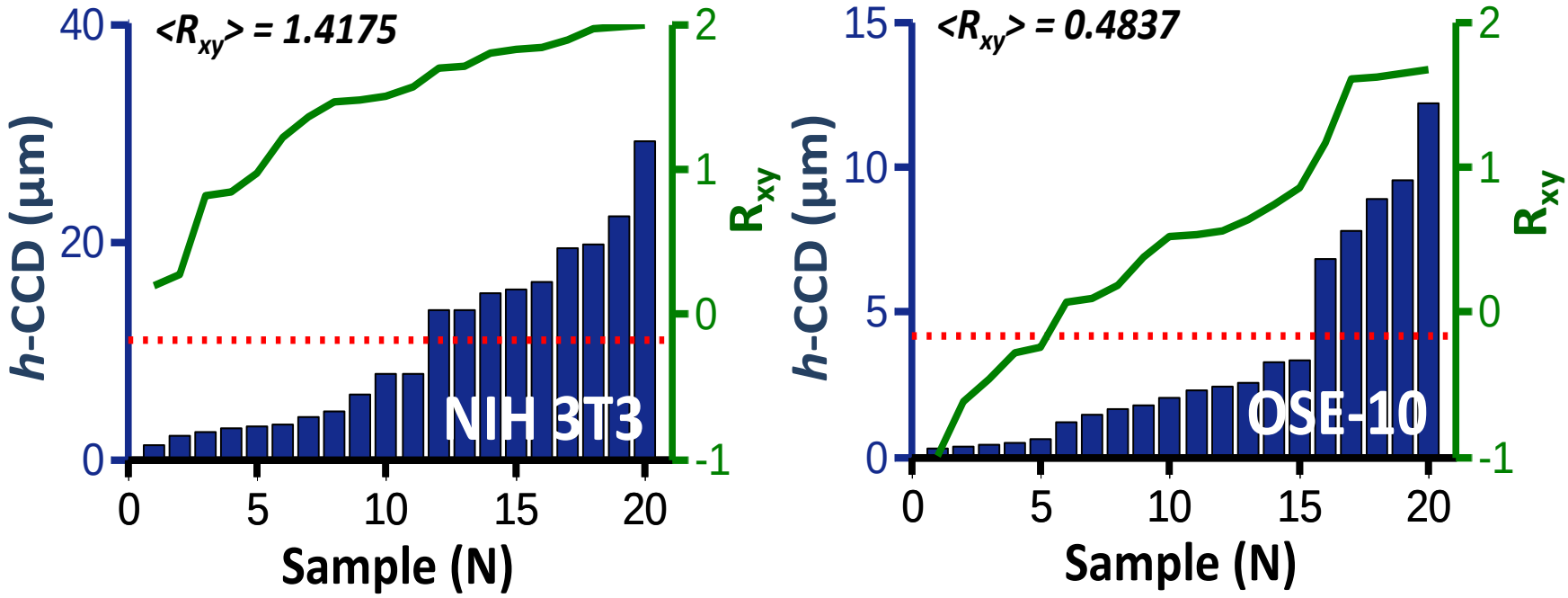

Figure 3-3. Highly correlated cell and nucleus reveals longer displacement. The correlation of cell and nucleus in X and Y axes was represented as Rxy. Comparison of Rxy and its cell displacement reveals that higher correlation has longer displacement in NIH 3T3 and OSE-10. From 20 random pickup cell samples, NIH 3T3 has larger average correlation than OSE-10. The correlation coefficient (R) is determined by PPMCC.

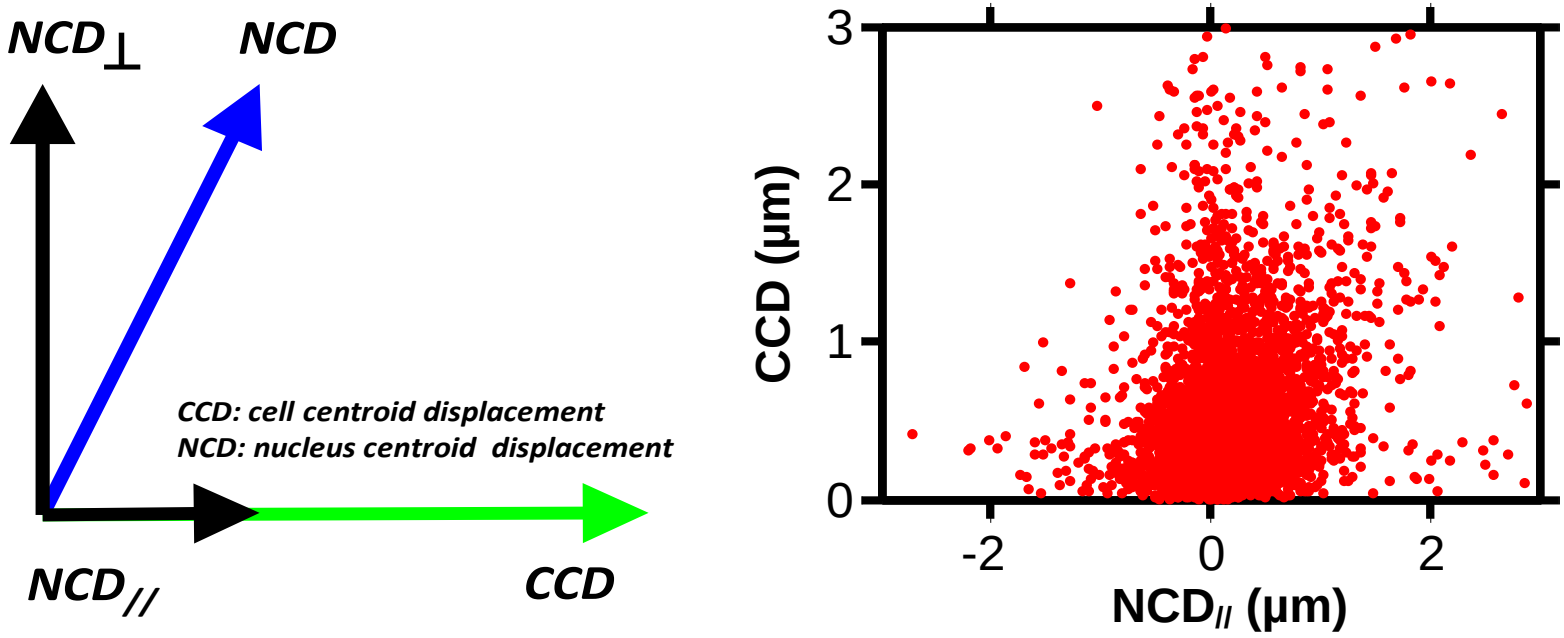

Figure 3-4. Correlation between cell and nucleus displacement. A nuclear centroid displacement (NCD) is divided into two orthogonal components, NCD//, which is paralleled to the direction of cellular centroid displacement (CCD), and NCD⊥, which is perpendicular to the direction of CCD. Meanwhile, the CCD and it corresponding NCD// can be used to construct a correlation (C-N correlation) through a Cartesian correlation system to describing cell migration events (Right). Red solid dots represent CCD and their coupled NCD// over a monitoring time of 60 minutes. Cell was monitored for 60 minutes with a cell sample size of 20.

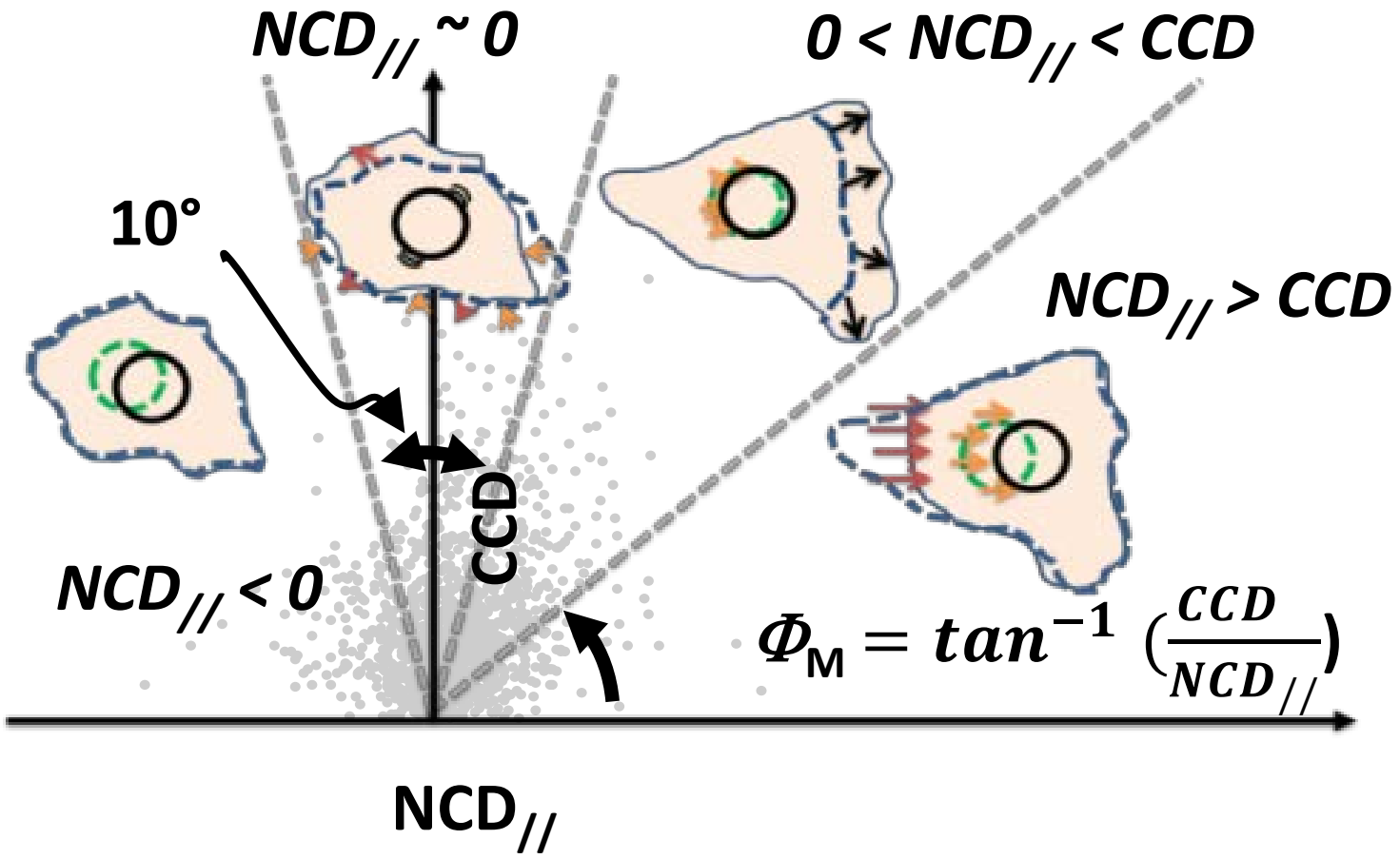

Figure 3-5. The relations between the CCD and NCD// can be built in a NCD// vs. CCD plot. When ϕ is defined as the angle from the x-coordinate to a line in the counterclockwise direction, four regions can be defined: Region I: 0° < ϕ ≤ 45°, Region II: 45° < ϕ ≤ 85°, Region III: 85° < ϕ ≤ 95°, and Region IV: 95° < ϕ ≤ 180°. For Regions I and II, it means the NCD are contributed to the whole cell displacement; for Region III, NCD ~ 0 and the cells are sampling; and for Region IV, nucleus motion is against cell motion.

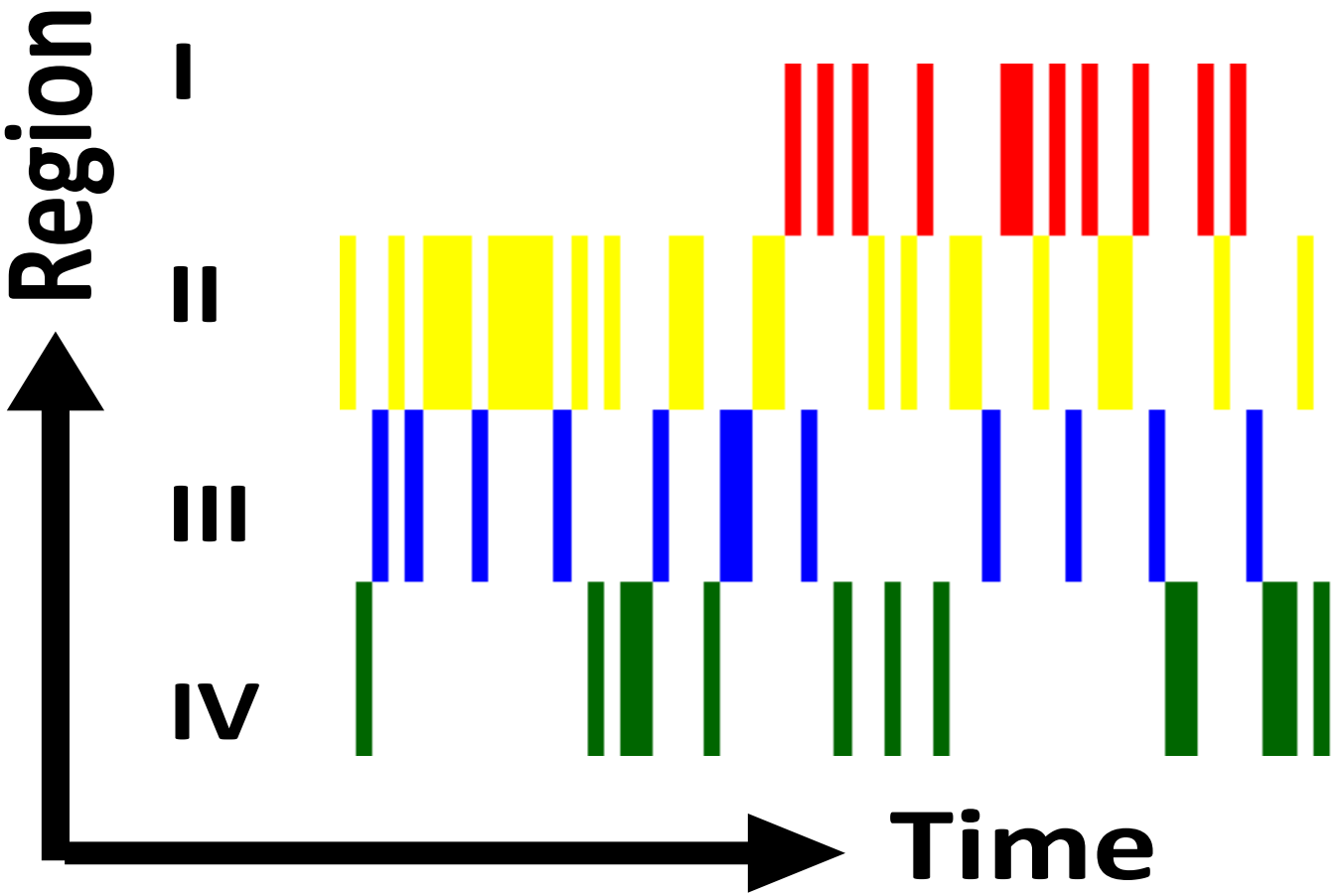

Figure 3-6. Colorful barcode representing migration behaviors. A barcode was created to present a group of CN correlation data generated from monitoring a cell for one hour. Individual datum in the group was presented as a bar, aligned following both its occurrence order in the group, from left to right, and its location in the CCD vs. NCD// plot, colored as red, yellow, blue, and green for Region I, II, III and IV from top to bottom, respectively.

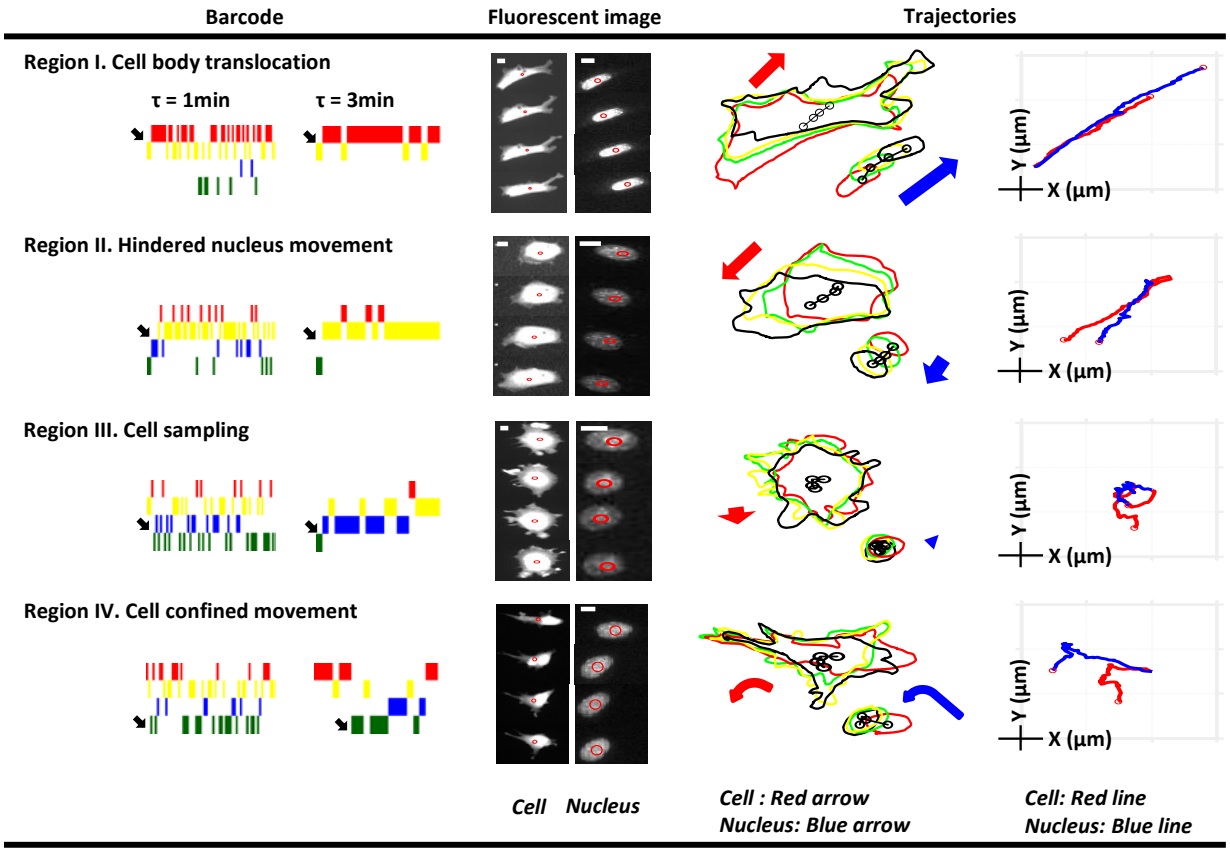

Figure 3-7. Colorful barcodes with their related cell migration behaviors. The analysis results of the four special cases were presented by individual panels, listed from Region I to IV to correspond to each barcode. These special cases were used to identify the unique cell migration pattern associated to the four regions. When the time interval was increased to 3 min to construct those barcodes, the predominant effects were further signified compared to 1 min interval time.The fluorescent images of the cell (left) and its nucleus (right) at a 20-min interval (at 1st, 21st, 41st, and 61st minute) were showed from top to bottom. Scale bar is 10 μm. The progressions of the boundaries (red, green, yellow and black traces, respectively) and centroids (black circles) of these images were indicated by arrows (red: cell, blue: nucleus). The trajectories of cell (red) and nucleus (blue) for each Region support arrows aside by the boundary sketches. From the arrows and its related trajectories, the biophysical meanings of the CN correlation located in each region were elucidated.

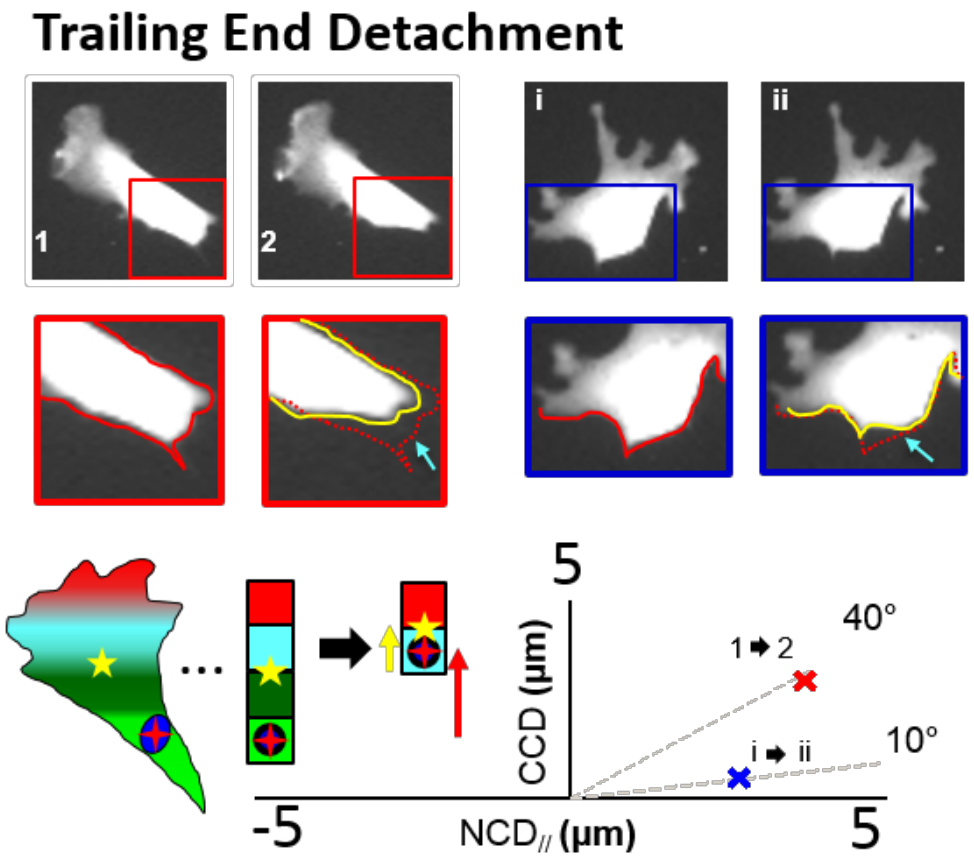

Figure 3-8. Trailing-end detachment on C-N correlation. Through screening images, pure detachment events can be seen from the continuous images and it corresponding cell and nucleus displacement can be mapped on C-N correlation profile between 10° and 40°. Red and Blue crosses separately represent the left and right images. The bottom sketch was used to describe the event, where a red cross and a yellow star separately represent the center of the nucleus and cell. The red and yellow arrows represent the magnitude and direction of nucleus and cell. Footnote in images represent the time series.

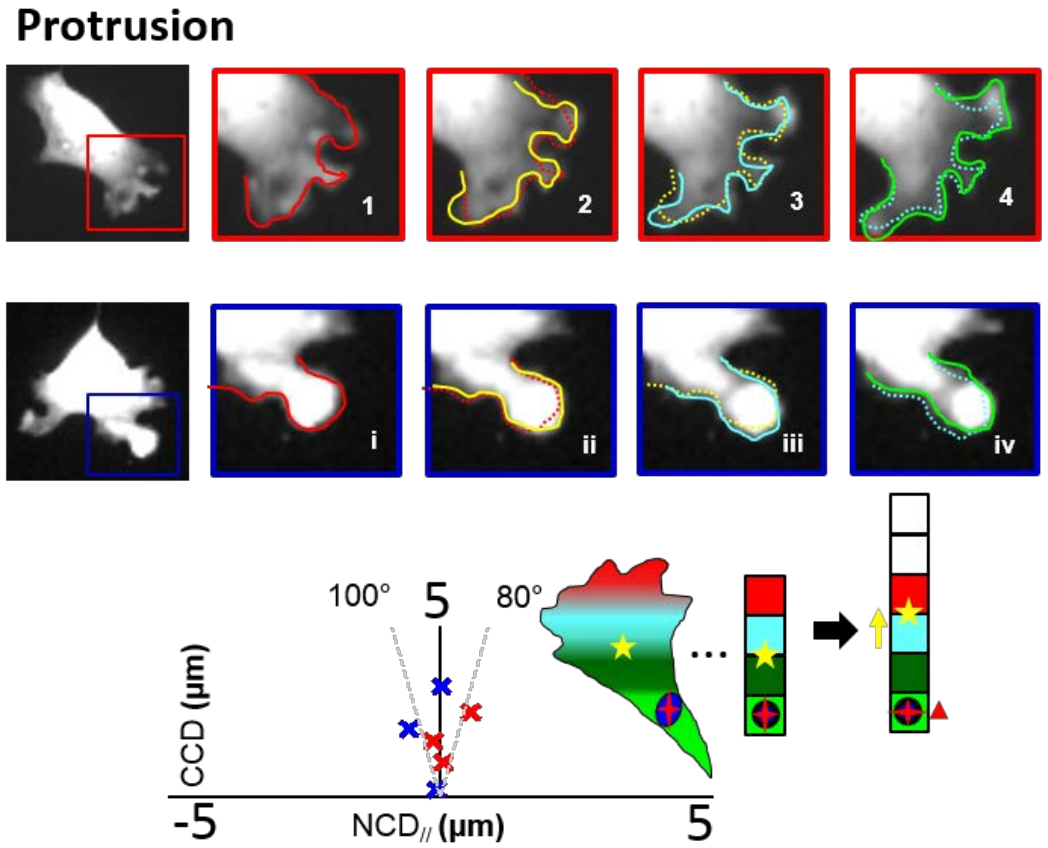

Figure 3-9. Protrusion on C-N correlation. Pure protrusion events can be seen from the longer continuous images and their corresponding cell and nucleus displacements can be mapped on C-N correlation profile between 80° and 100°. Red and Blue crosses separately represent the top and bottom images. The bottom sketch was used to describe the event, where a red cross and a yellow star separately represent the center of the nucleus and cell. The red and yellow arrows represent the magnitude and direction of nucleus and cell. Footnote in images represent the time series.

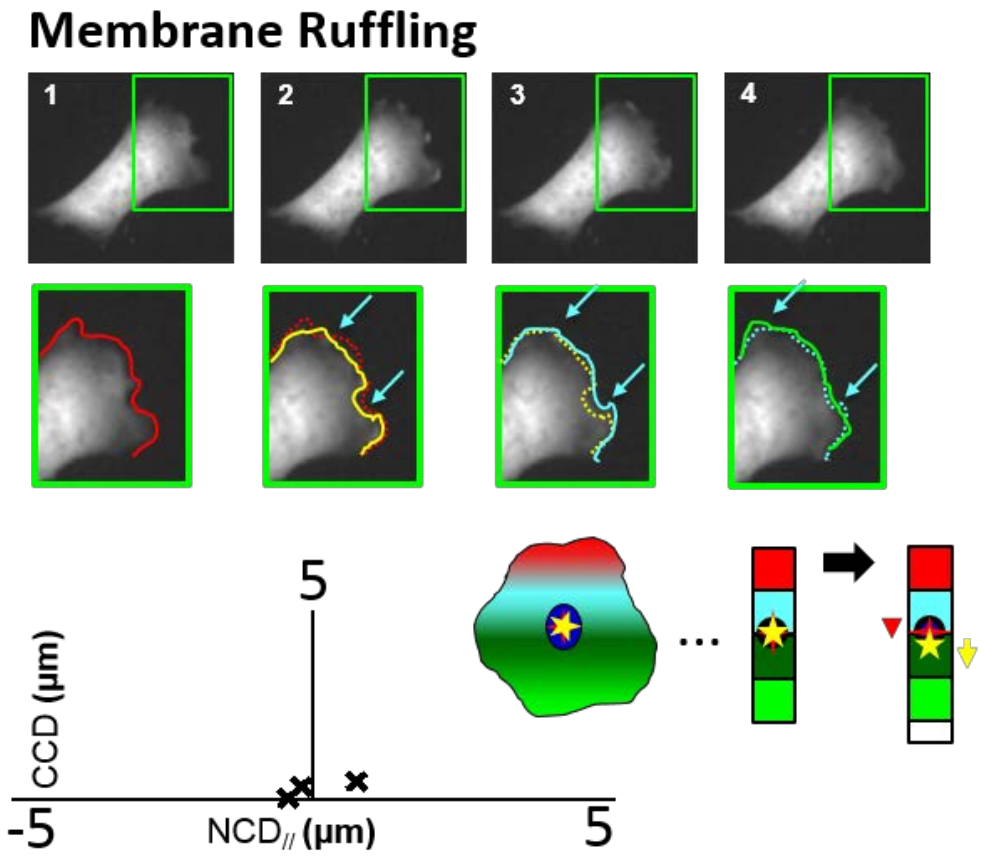

Figure 3-10. Membrane ruffling on C-N correlation. Ruffling events shows high frequency of dynamic protrusion and detachment at peripheral edge of cell with stationary nucleus movement. It corresponding cell and nucleus displacements can be mapped on C-N correlation profile with smaller magnitude but all range from 0° and 180°. The bottom sketch was used to describe the event, where a red cross and a yellow star separately represent the center of the nucleus and cell. The red and yellow arrows represent the magnitude and direction of nucleus and cell. Footnote in images represent the time series.

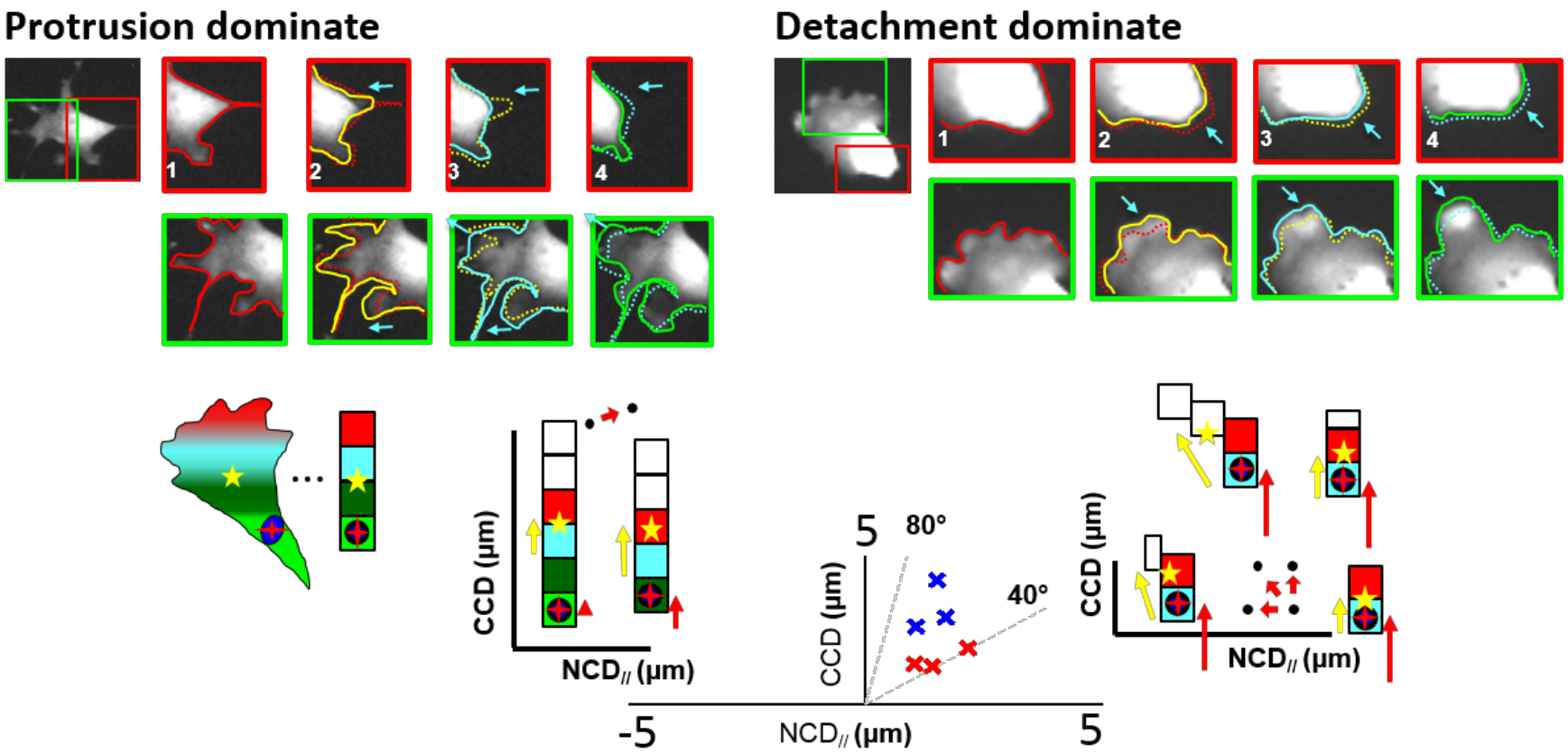

Figure 3-11. Complexity subcellular activities on C-N correlation. A forward movement usually includes a mixture of detachment and protrusion activities. Left and right panel separately shows the protrusion and detachment dominating migration process. Their corresponding cell and nucleus displacements mapping on C-N correlation separately represented as blue and red crosses and between 80° and 100°. The bottom sketch was used to describe the event, where a red cross and a yellow star separately represent the center of the nucleus and cell. The red and yellow arrows represent the magnitude and direction of nucleus and cell. Footnote in images represent the time series.

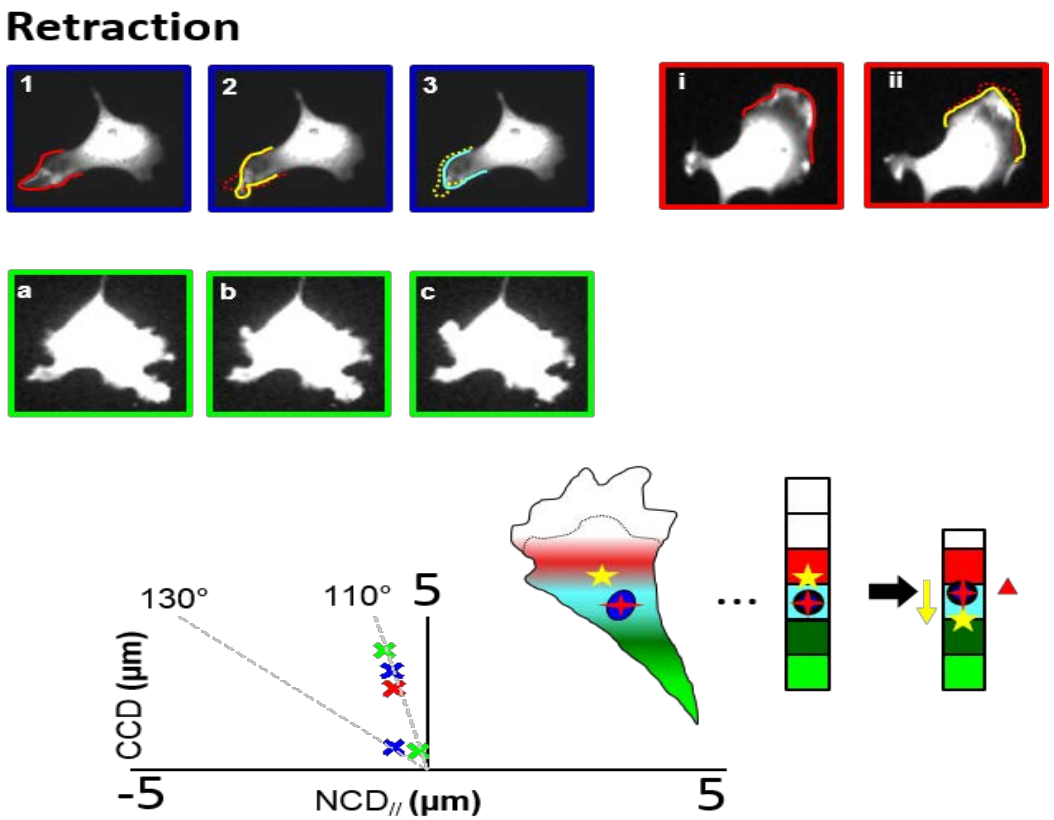

Figure 3-12. Retraction on C-N correlation. Retraction is not a solely effect and always happens after protrusion. Three image series show a retraction effect after protrusion and their corresponding cell and nucleus displacements mapping on C-N correlation separately represented as blue (Left top), red (Right top), and green (Left bottom) crosses and between 110° and 130°. The bottom sketch was used to describe the event, where a red cross and a yellow star separately represent the center of the nucleus and cell. The red and yellow arrows represent the magnitude and direction of nucleus and cell. Footnote in images represent the time series.

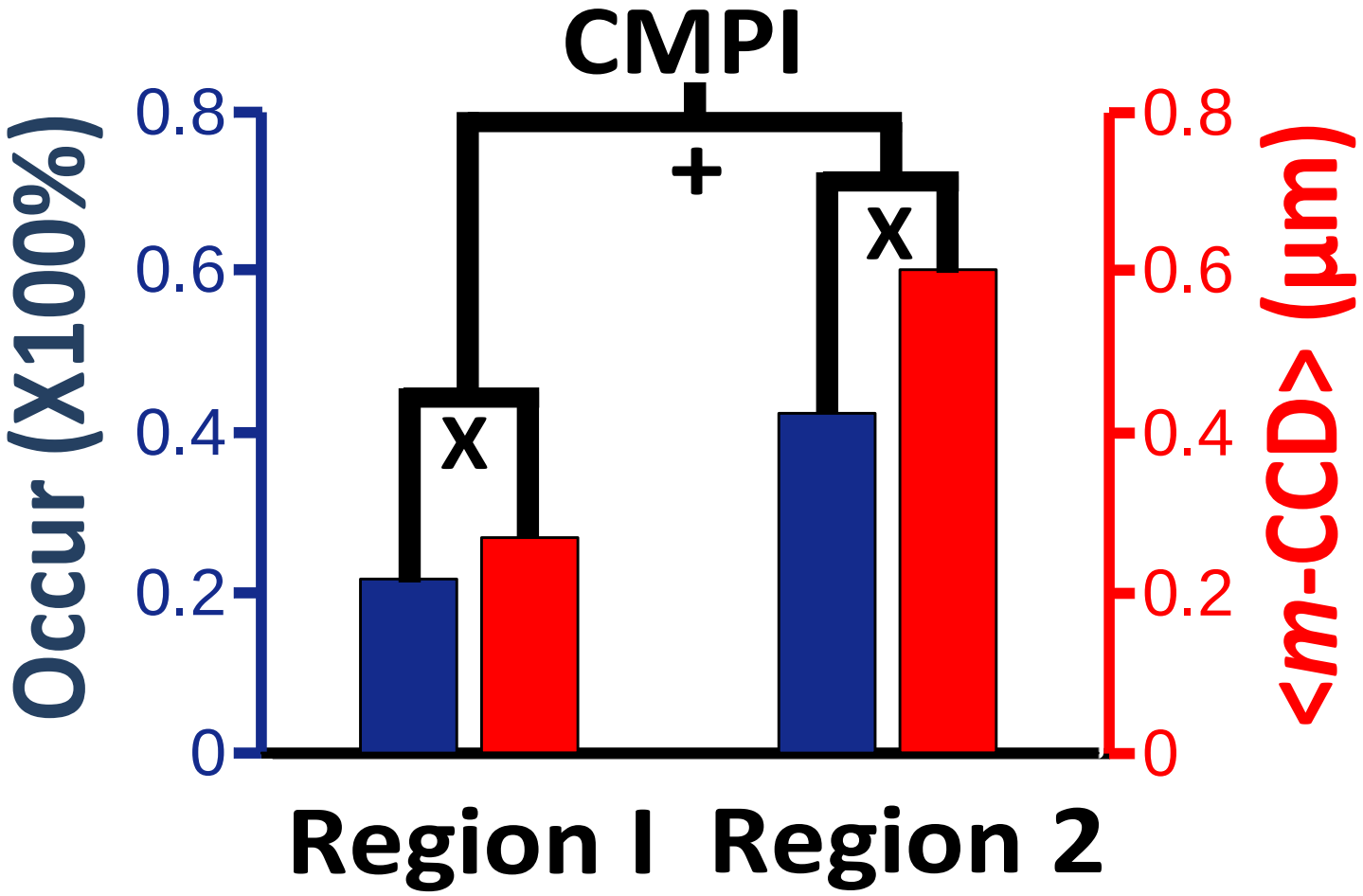

Figure 3-13. Sketch of calculation of CMPI. CMPI was determined by summary of occurrence (Occur) plus average cell displacement (<m-CCD>) in Region I and II. Blue and Red bars are separately represented occurrence and average displacement

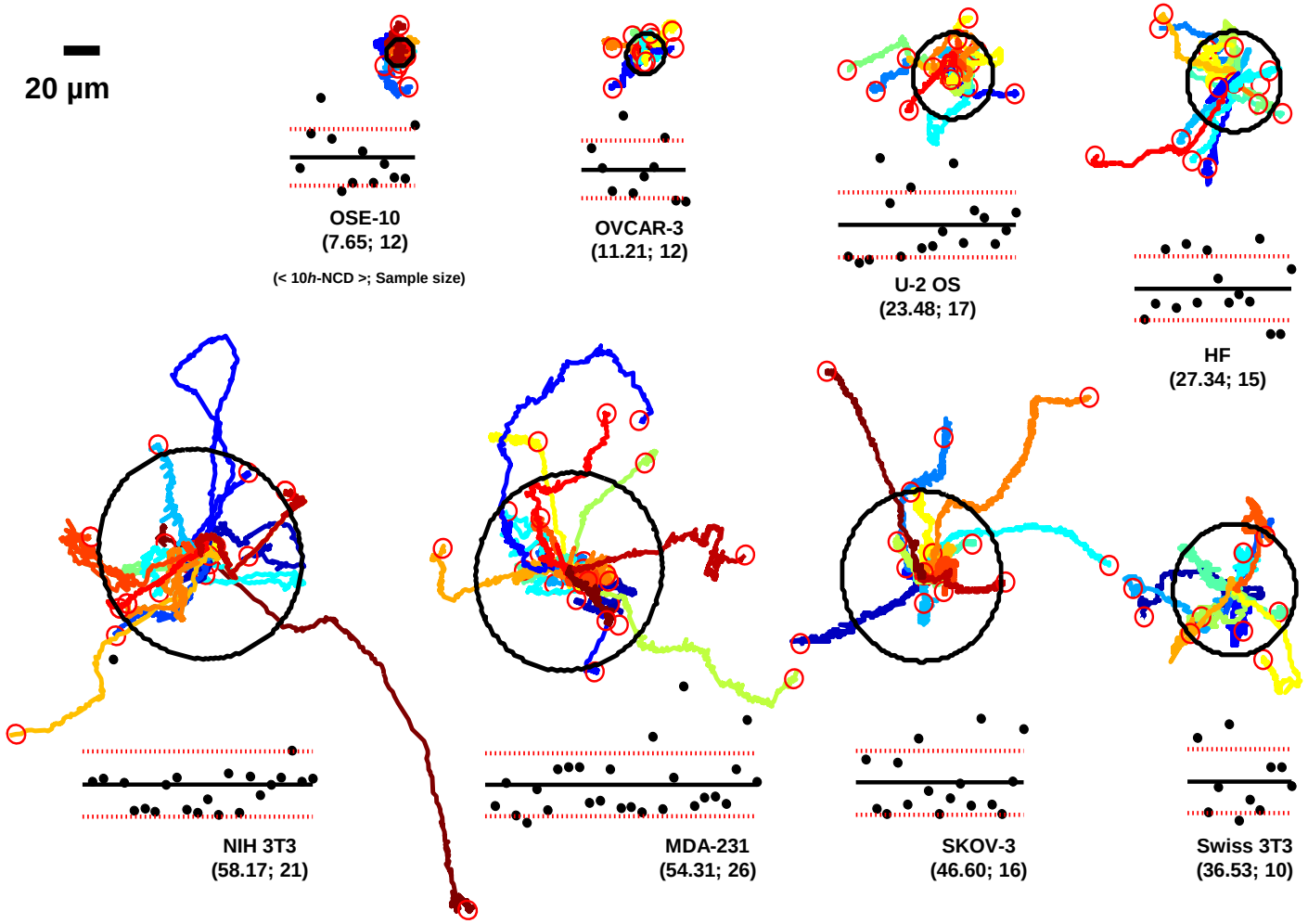

Figure 3-14. Trajectory as gold standard for cell migration. Displacements started at the center of the reference circle (yellow), the radius of which represents the average 10 hour displacement. The horizontal black and dotted red lines indicate the < 10h-NCD > and one standard deviation, respectively, for all the cells, and the points plotted correspond to the individual 10h-NCD values of each cell. The values of < 10h-NCD > and sample size are indicated in the parenthesis, respectively, following by the name of each cell type.

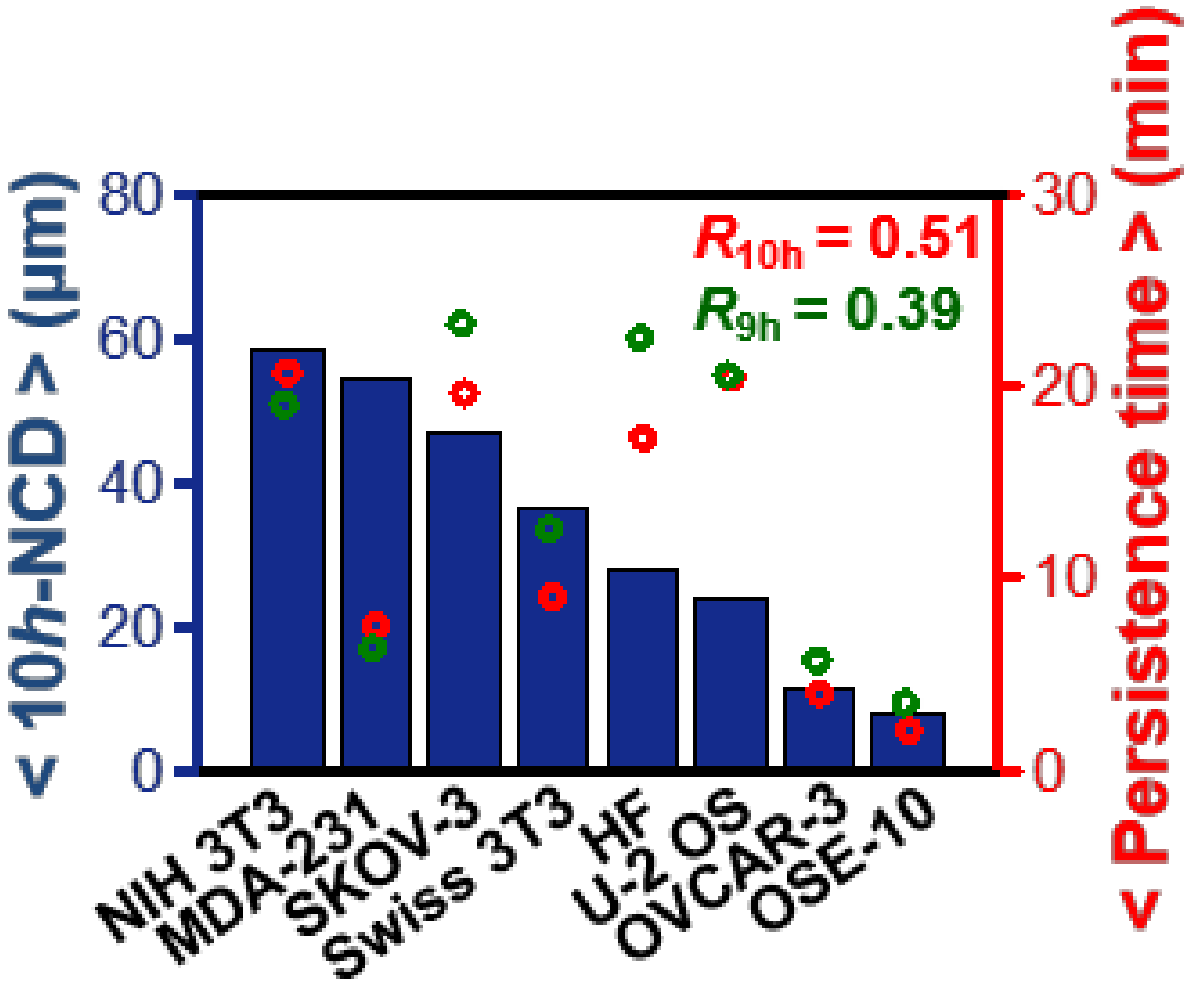

Figure 3-15. The correlation between < 10h-NCD > and persistence time. < 10h-NCD > of each cell type (bars) is compared against the extracted persistence time from 9 (green circles) and 10 (red circles) hours of trajectories. The correlation shows 0.39 and 0.51 separately. The correlation coefficient (R) is determined by PPMC.

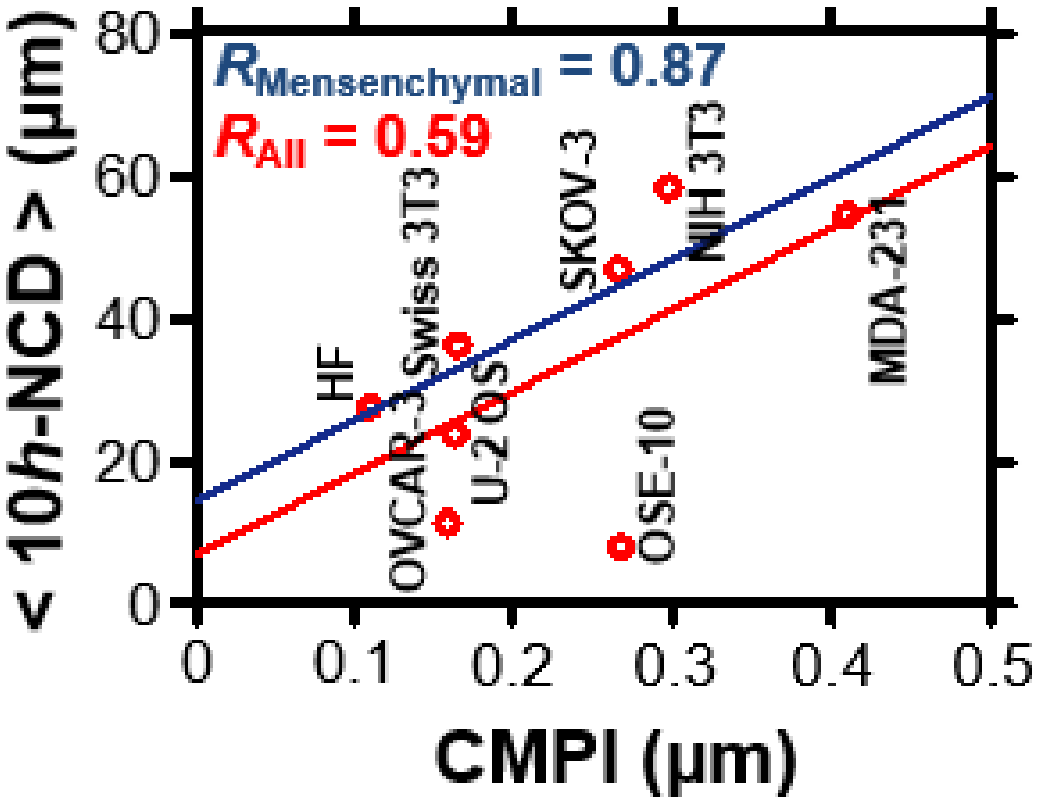

Figure 3-16. The correlation between < 10h-NCD > and CMPI. The correlation coefficient (R-value) between < 10h-NCD > and CMPI improves from 0.59 to 0.87 when only considering cell types that mainly rely on mesenchymal mode to migrate. The correlation coefficient (R) is determined by PPMC.

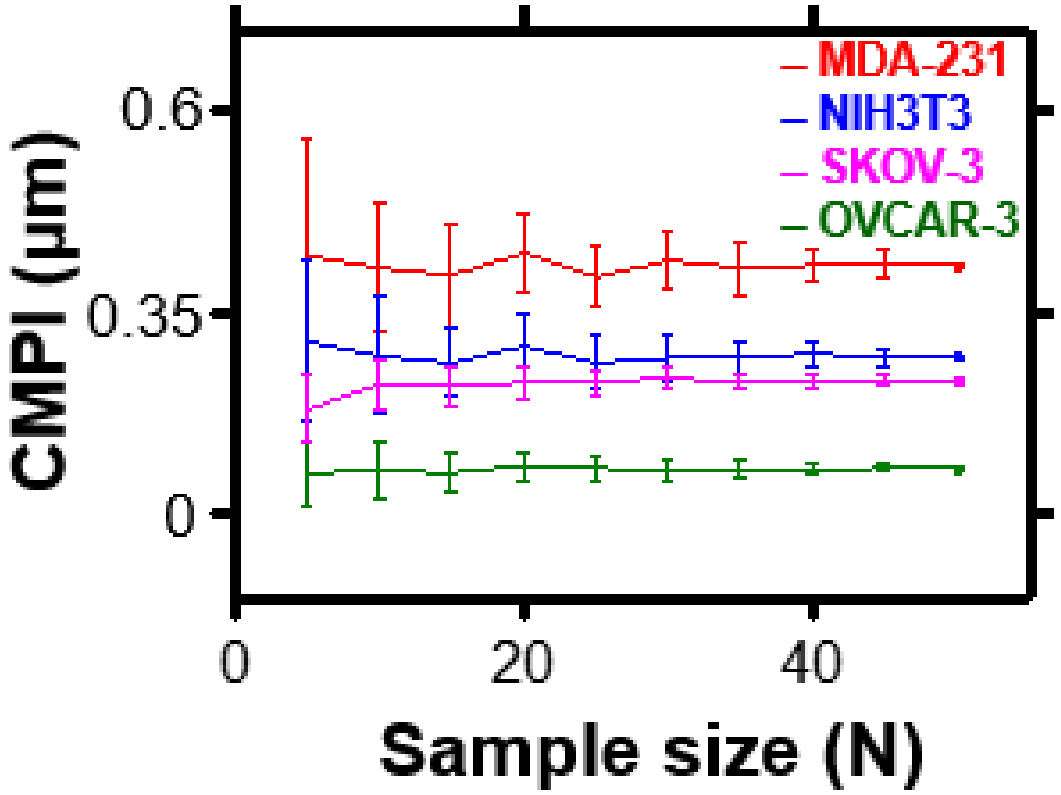

Figure 3-17. The stability of CMPI. CMPI variance reduces as sample size increases for MDA-231, NIH 3T3, SKOV-3 and OVCAR-3, supporting that CMPI stabilizes when sample size increase to at least 20 cell. Error bar represents the STD.

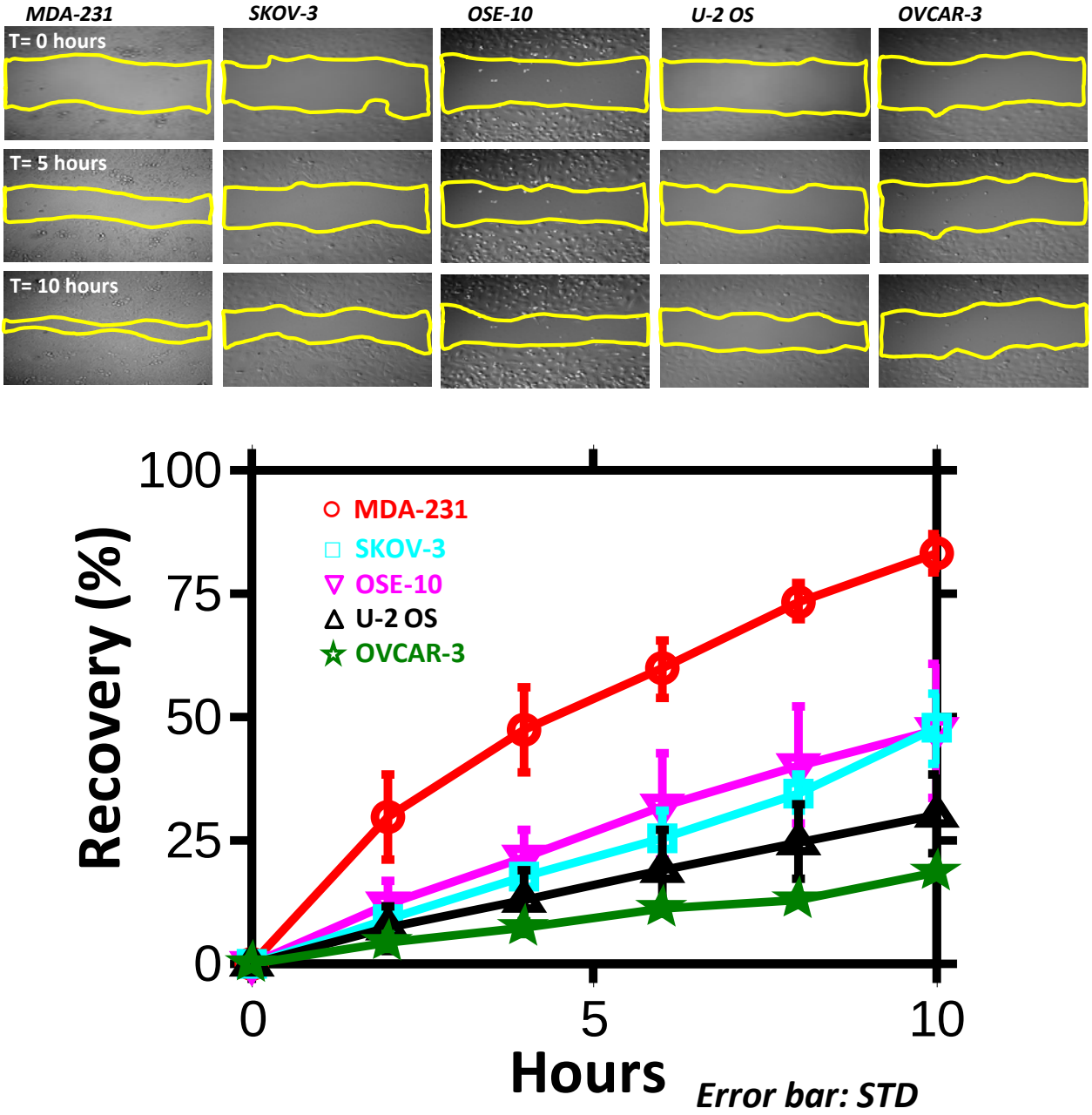

Figure 3-18. Wound recovery image and recovery rate of epithelial cells. The wound-like gap closure processes of 5 different epithelial cells were analyzed by their videos (examples on left panels) and the results were presented as the percentage of gap recovery over a 10-hour period (right panel). Error bar represents the STD.

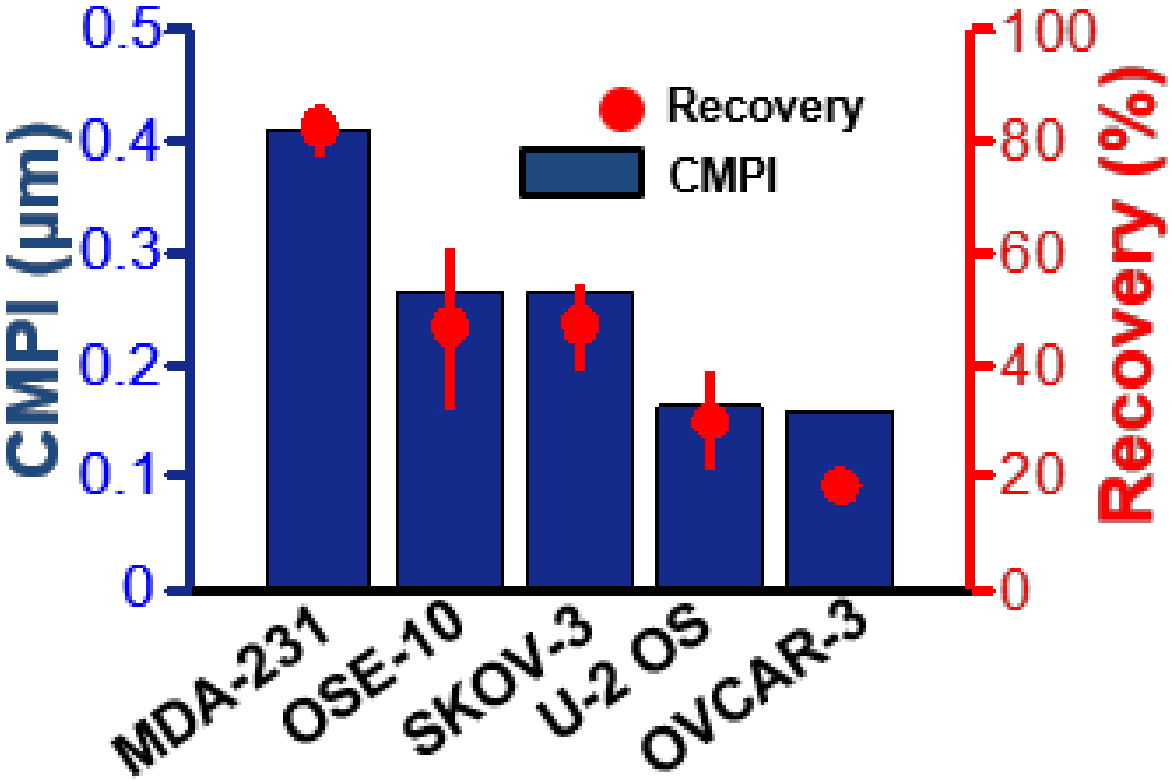

Figure 3-19. Well correlation between CMPI and recovery rate. Well correlation between CMPI and recovery rate. The cell migration potentials of the 5 epithelial cells directly determined by their CMPI were highly consistent to the results gained from 10 hours after the wound-like gap processes. Error bar represents the STD.

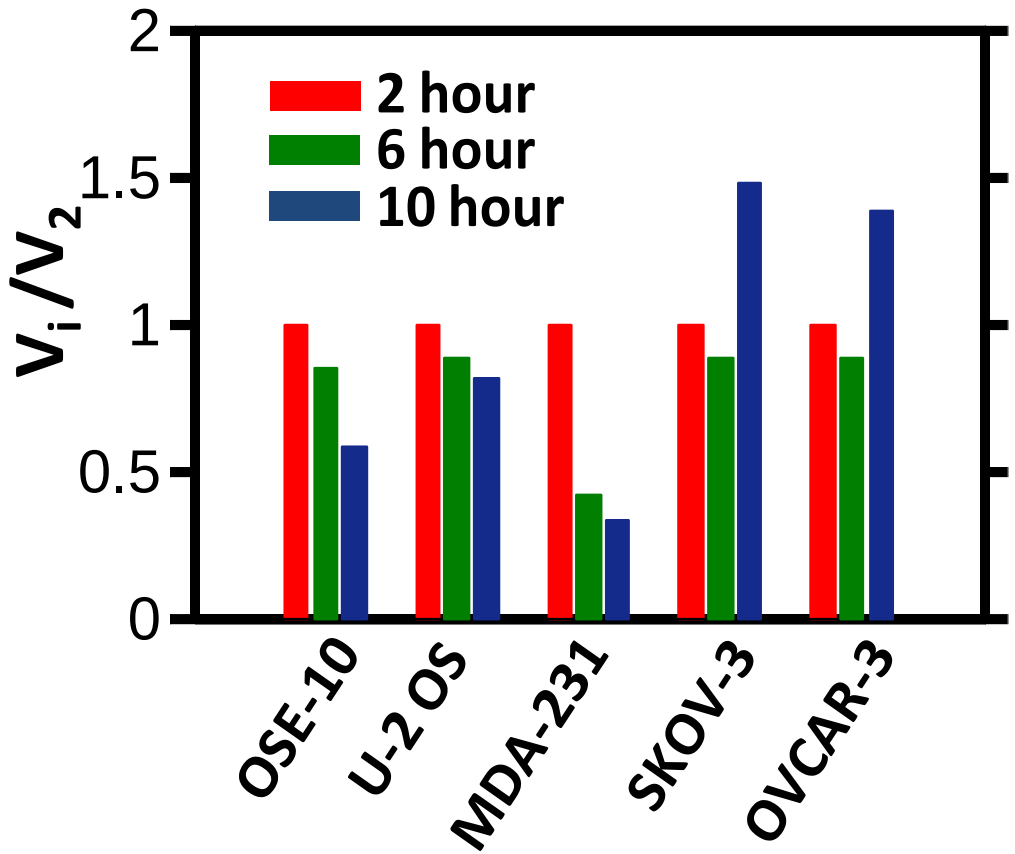

Figure 3-20. Recovery rate at different time point suggests cell-cell contact effect. Each of the wound-like gap recovery process of the 5 epithelial cells was not at constant rate. The rates of 3 cell types were inclined, while those of 2 cell types were declined.

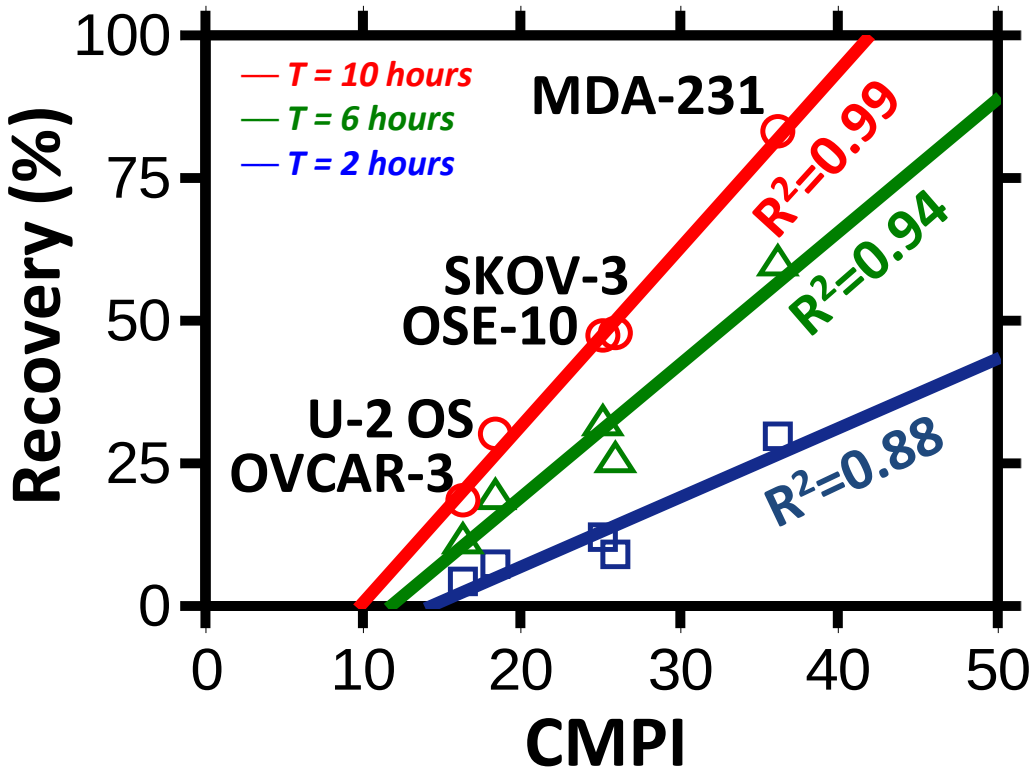

Figure 3-21. Correlation between recovery rate and CMPI at different time points. The linear correlation curves of the wound-like gap recovery percentages at 2, 6 and 10 hours vs. CMPI values for the 5 probed epithelial cells (left panel). The linear regressions were 0.88, 0.95 and 0.99, respectively (right panels). The correlation coefficient (R) is determined by PPMC.

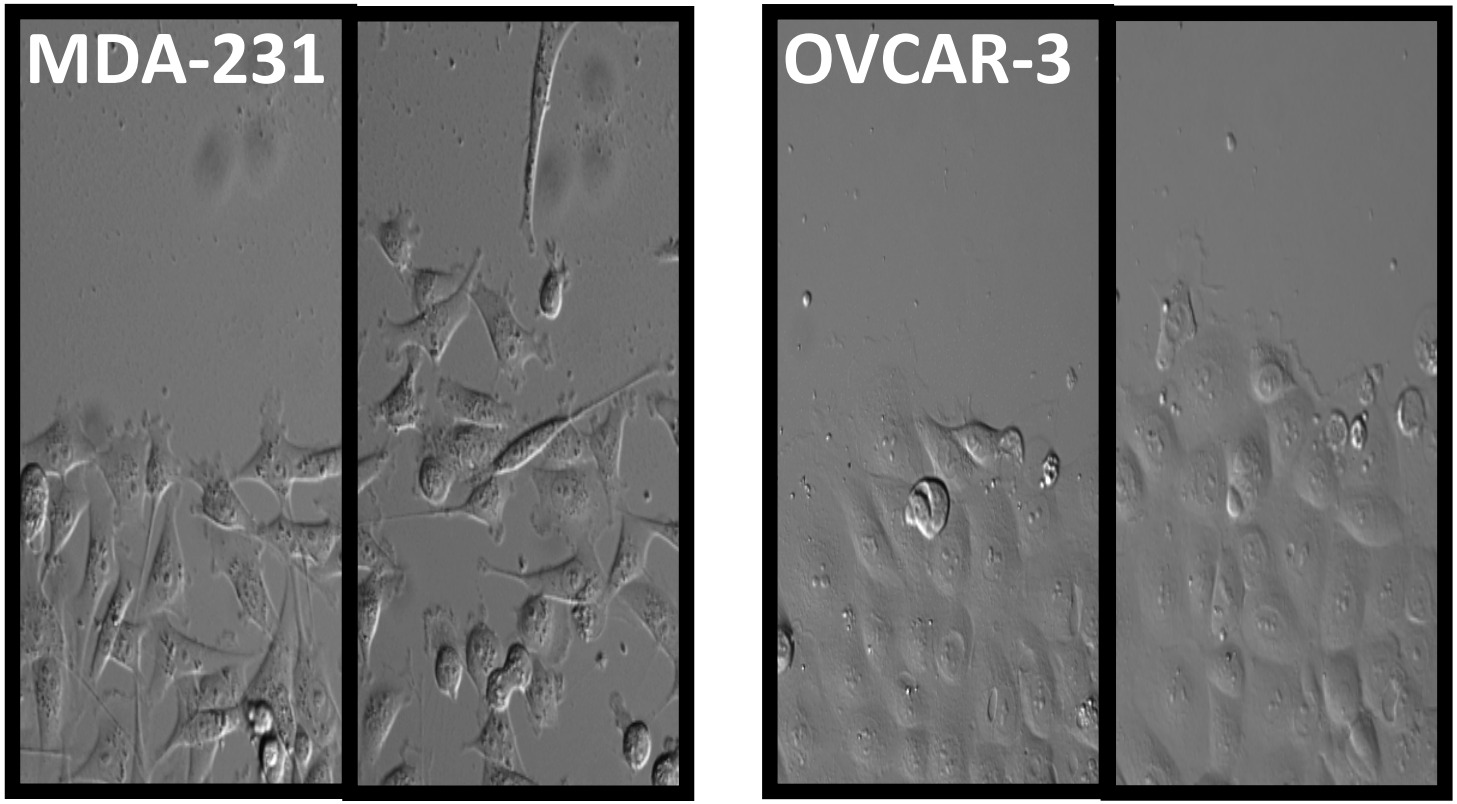

Figure 3-22. Different migration pattern during wound disclosure. MDA-231 moves toward single instead of collective movement, such as OVCAR-3.

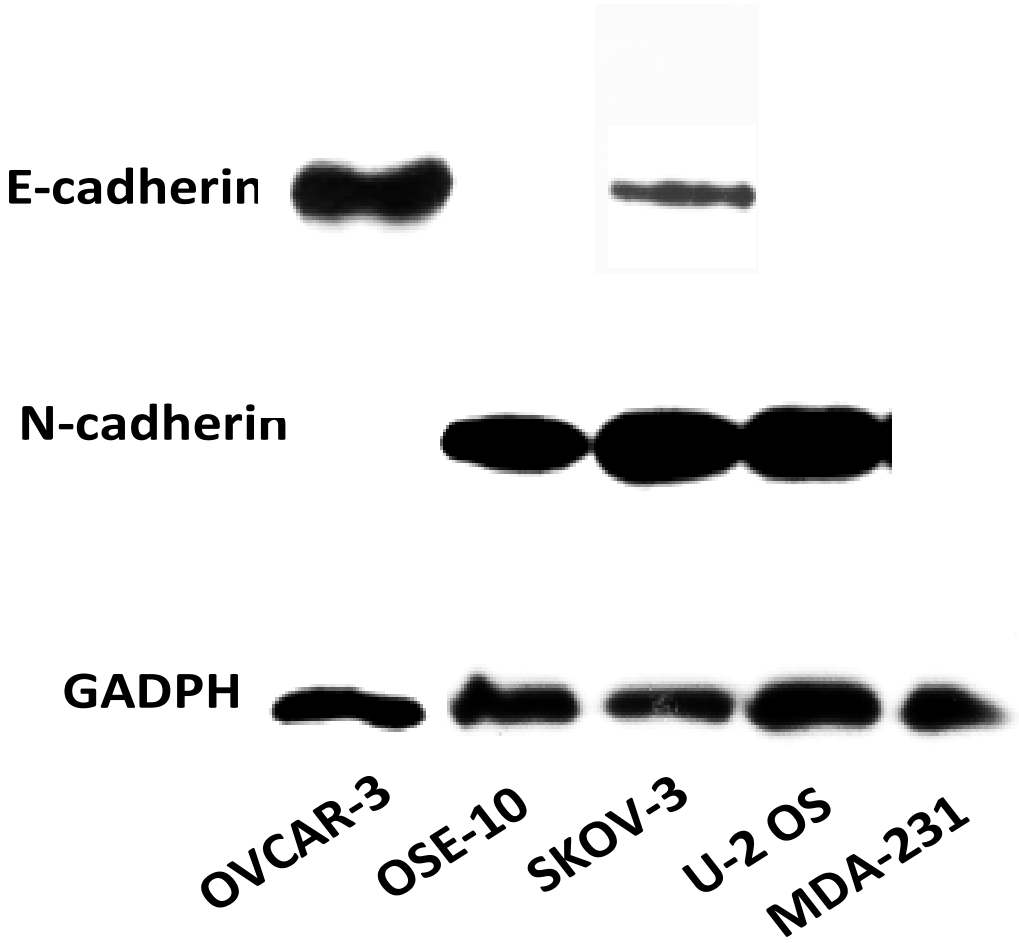

Figure 3-23. Western blotting supports the cell-cell contact issue. The western blotting of the 5 cell types against E- and N-cadherin revealed the expression levels of these proteins in the cell samples. The same blotting used housekeeping protein, GADPH, as a reference protein.

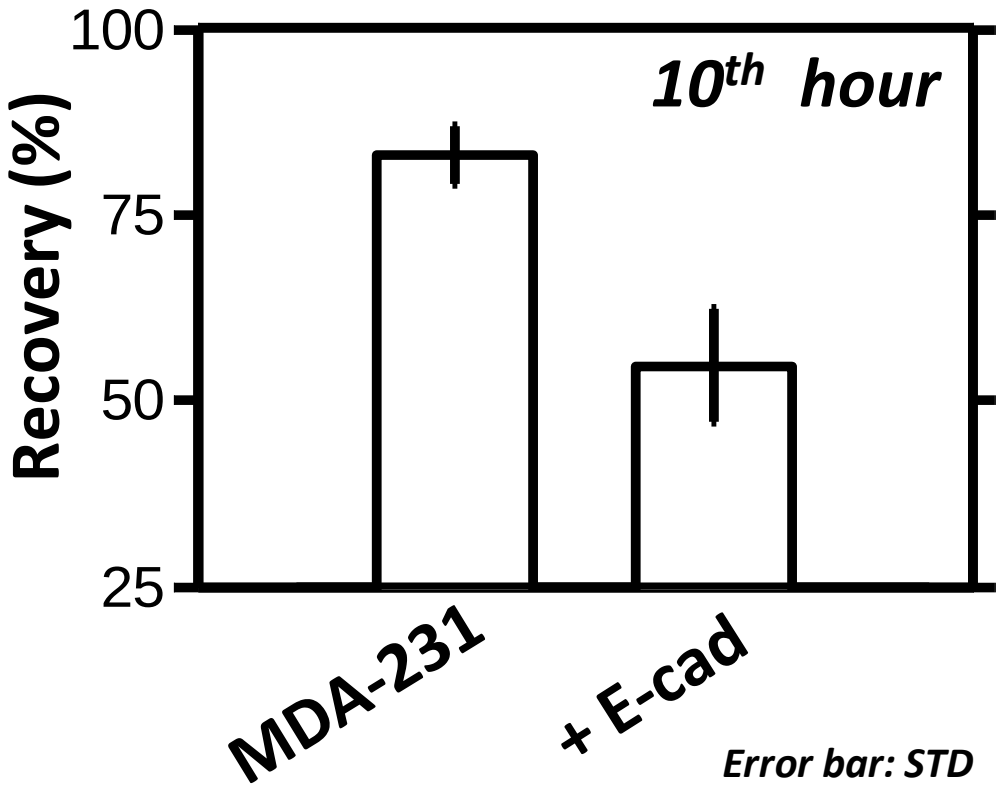

Figure 3-24. The introduction of E-cadherin into MDA-231 cells hindered the wound-like gap recovery process. After E-cadherin delivered into MDA-231, MDA-231 (E-cad) was culturing in insert under general process (see material and method). MDA-231 with E-cadherin delivery shows less recovery rate comparing with wild type (around 50%). Error bar represents the STD.

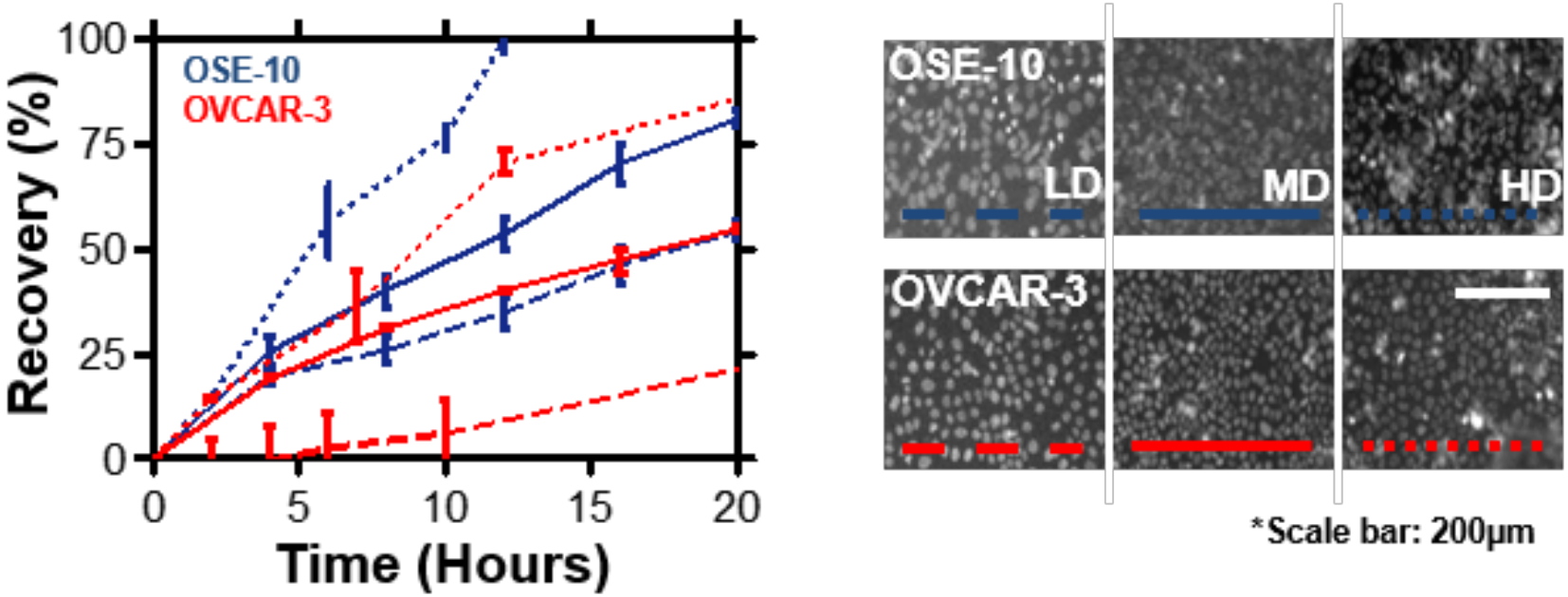

Figure 3-25. Cell density plays roles in wound healing assay altering migration ability. Wound-like gap recovery at different initial cell densities alters the apparent migration ability of OVCAR-3 and OSE-10 cells (Left). Cell density was estimated through staining and counting the number of nuclei in the initial frame. All scale bars represent 200 μm and error bars represent standard deviation (Right). LD, MD and HD separately represent different seeding densities.

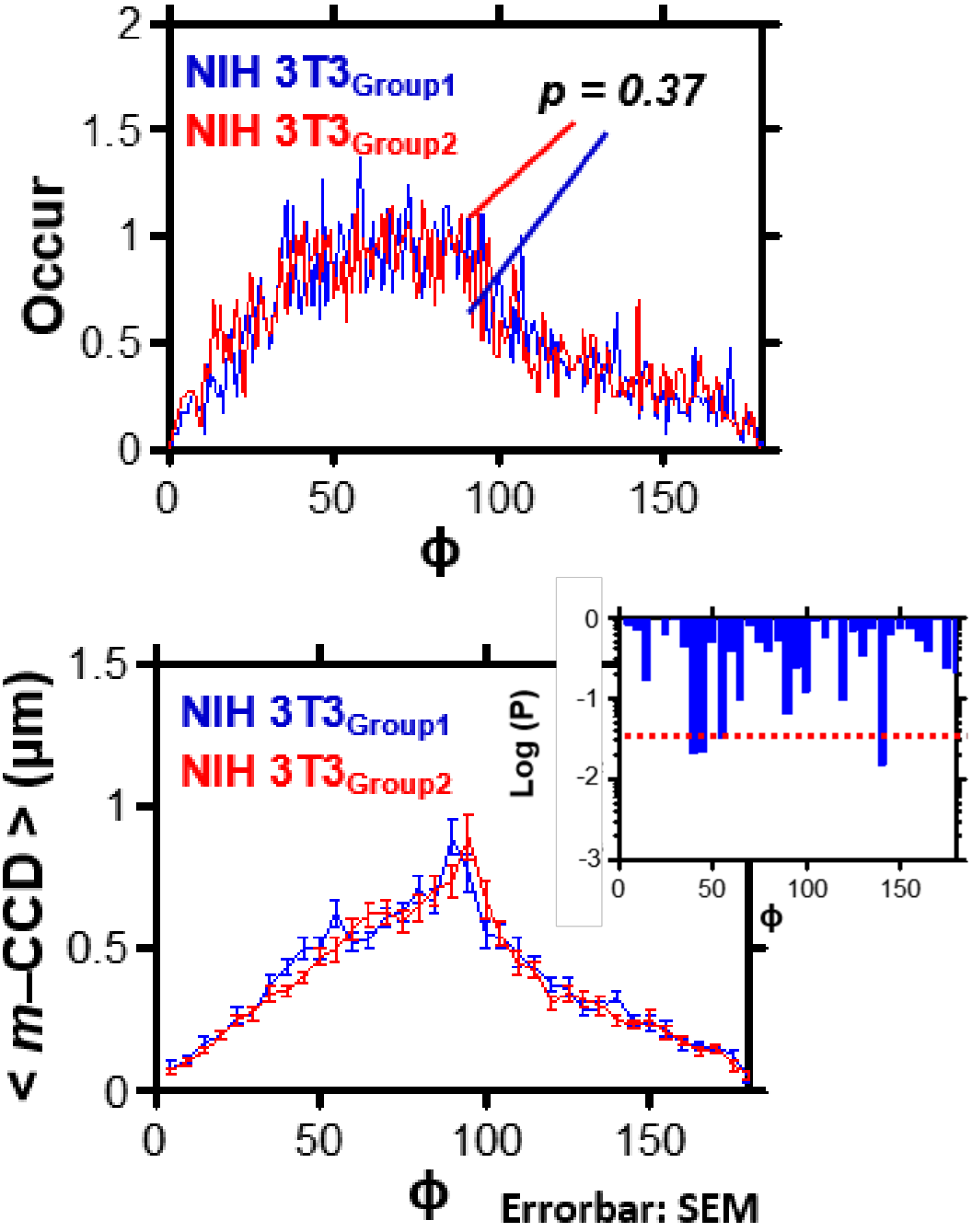

Figure 3-26. C-N correlation suggests a highly correlated between two NIH 3T3 groups. The occurrence profile (Top) between two NIH 3T3 groups are correlated with a p value around 0.37 with 1 degree spanning. The magnitude of cell displacement (<m-CCD profile>, Bottom)) also gives a good correlated result between two NIH 3T3 groups with 5 degree spanning. The corresponding student t-test in every 5 degree spanning was shown in the right-top corner. The red dash line represents the p value is 0.05.

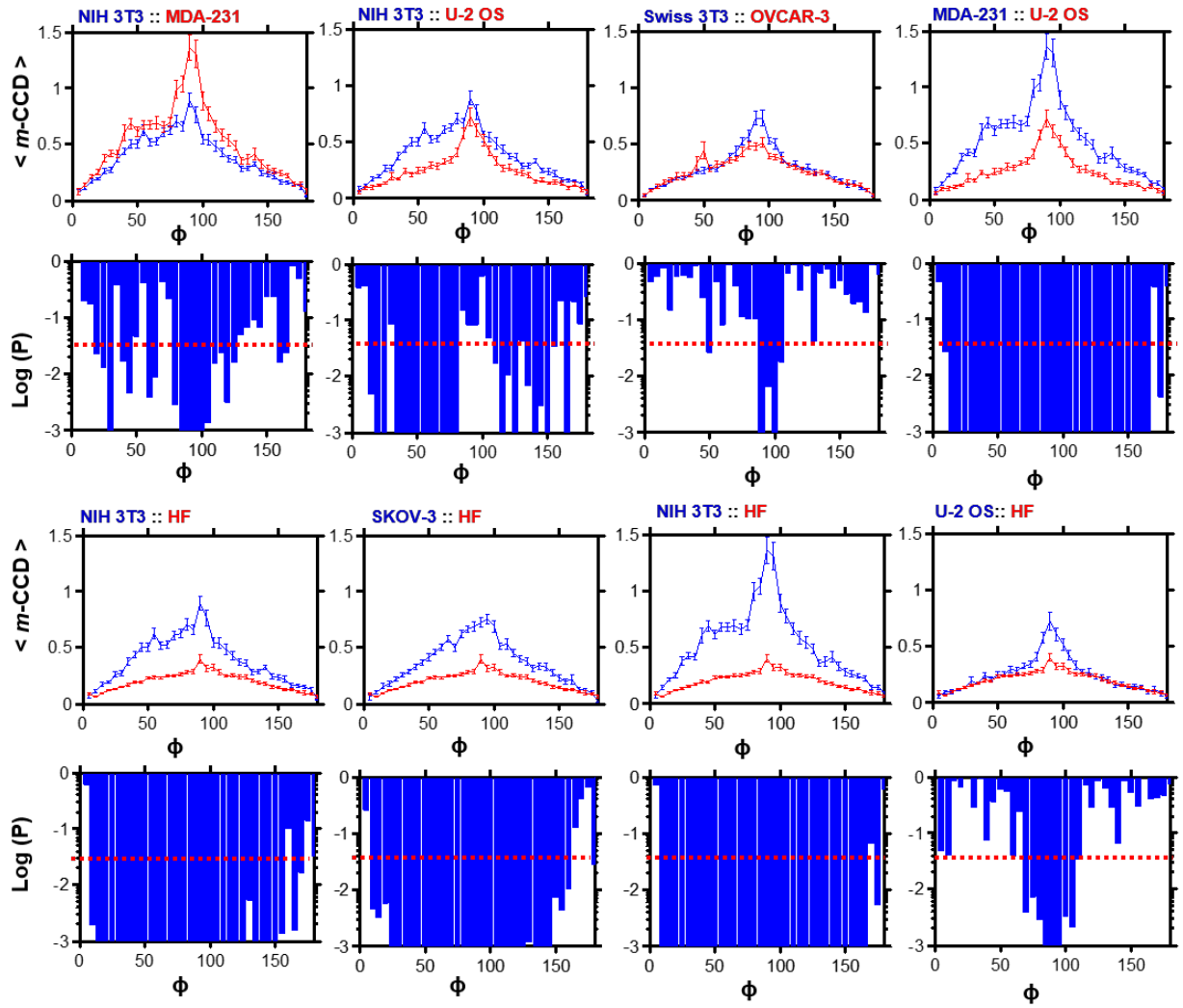

Figure 3-27. Similar angular distribution but significant different in magnitude of the CCD in C-N correlation. The above paired cells cannot not be distinguished by occurrence profile but show a significant difference through cell displacement profile (<m-CCD>). This suggests that C-N correlation has the cell distinguishing ability as one of cellular parameter.

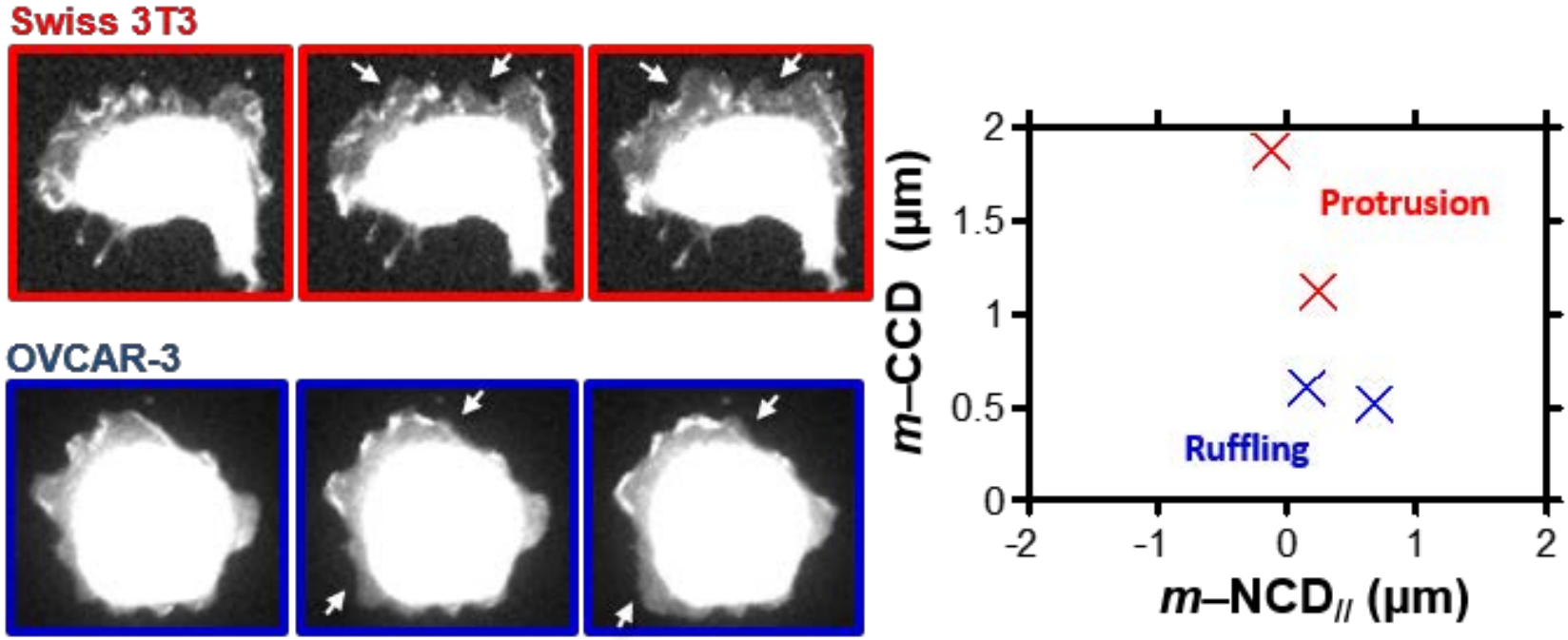

Figure 3-28. The distinguishing between protrusion and ruffling in Swiss 3T3 and OVCAR-3. The significant difference between Swiss 3T3 and OVCAR-3 is the magnitude along the Y-axes on the C-N correlation. From the continuous images of Swiss 3T3 (Top) and OVCAR-3 (Bottom), Swiss 3T3 has large magnitude displacement at the peripheral edge of cell as protrusion activity. In contract, OVCAR-3 has minor peripheral edge displacement but more dynamic activities there.

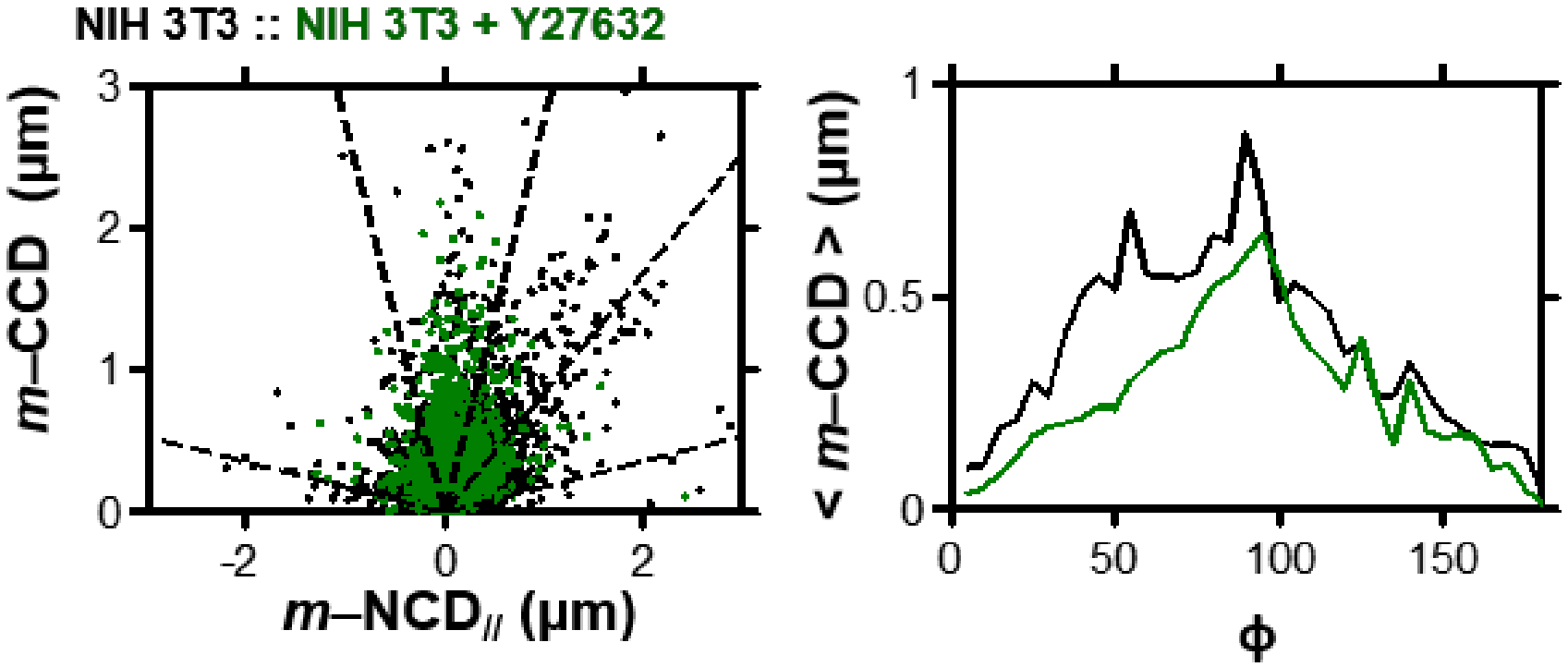

Figure 3-29. Cellular activities disrupted by Y27362 alter the C-N correlation. To investigate if the C-N correlation can respond to the change in the subcellular activities, Y27632, the ROCK inhibitor was applied. From the C-N correlation mapping, Y27632 treated NIH 3T3 (green dots) shows a decrease density between 10° and 80° comparing with wild type (black dots) (Left panel). Further, it shows a significant decrease in magnitude between 10° and 90°, which may mainly due to the loss of focal adhesion.

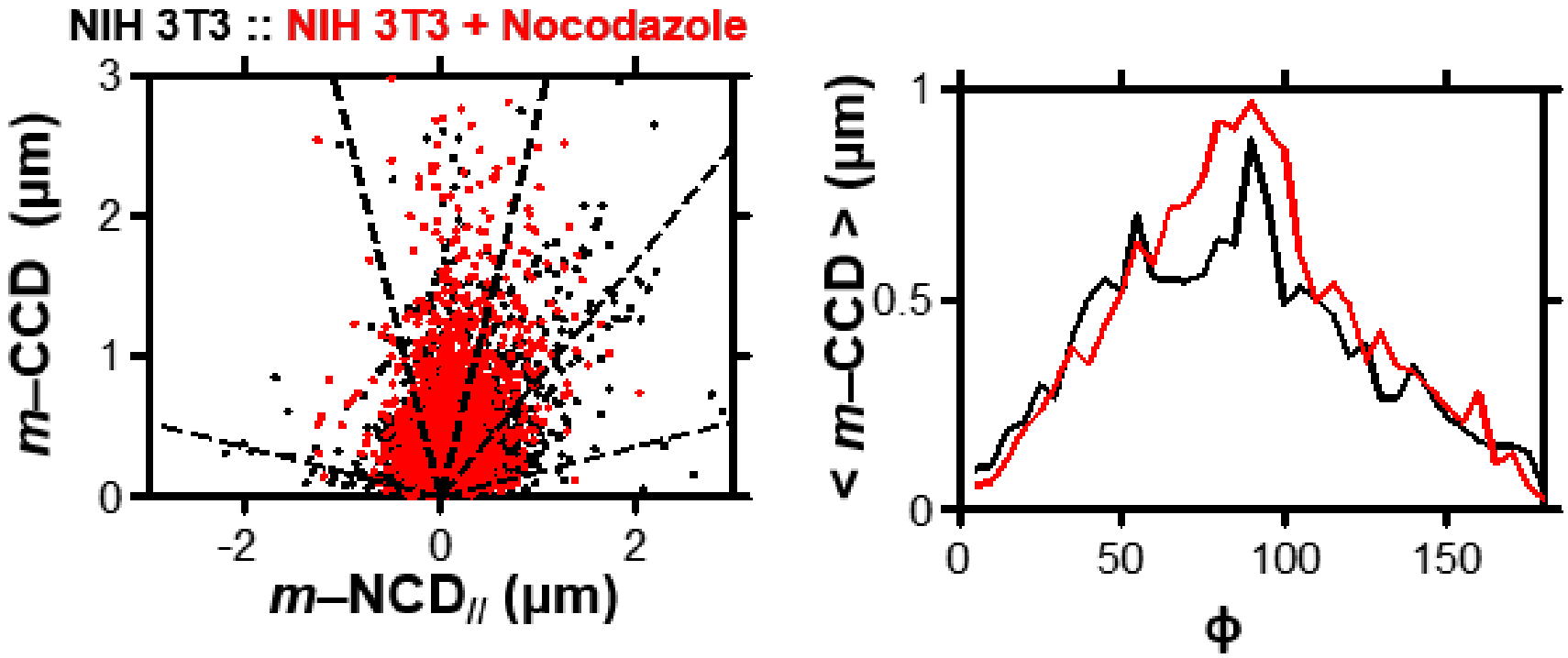

Figure 3-30. Cellular activities disrupted by Nocodazole alter the C-N correlation. Also, Nocodazole, the microtubule inhibitor was further applied to examine the correlation. From the C-N correlation, it shows no significant difference between wild type (black dots) and Nocpdazole applied NIH 3T3 (red dots). However, it shows an increase in magnitude between 80° and 100°, which may due to the disruption of microtubule turnover.

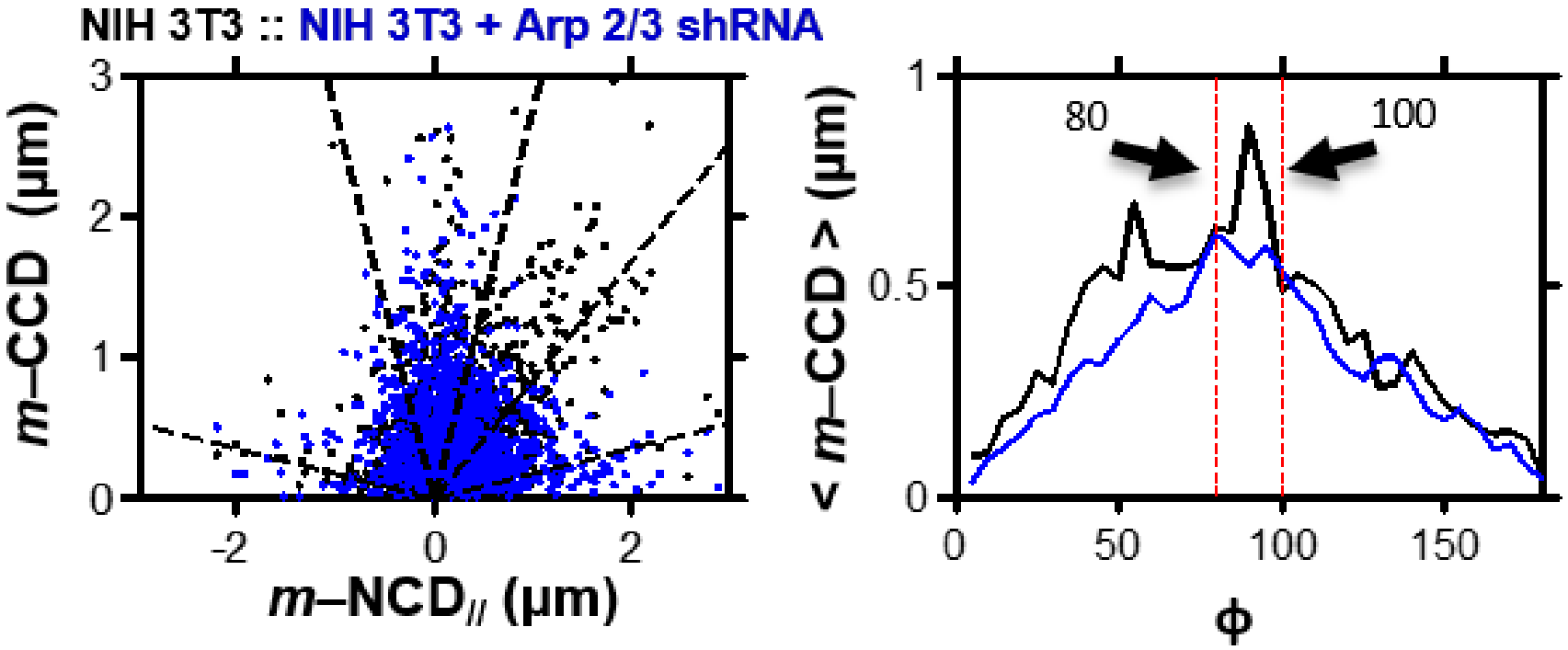

Figure 3-31. Cellular activities disrupted by Arp2/3 shRNA alter the C-N correlation. With Arp 2/3 shRNA delivery, the C-N correlation shows a reduced density (blue dots) between 40° and 80° comparing to wild type (black dots) (Left panel). Further, it shows a decrease in magnitude between 80° and 100°, which may due to the disruption of lamellipodia (Right panel).

Table 3-1. The composition of occurrence and average cell displacement in region I and II of different cell lines and their related CMPI.

	MDA-231	NIH 3T3	SKOV-3	OSE-10	Swiss 3T3	U-2 OS	OVCAR-3	HF
OccurRegion I (%)	24.05	28.93	18.03	17.93	18.50	25.54	17.60	23.52
< m-CCD >Region I (μm)	0.57	0.32	0.28	0.27	0.19	0.17	0.21	0.14
OccurRegion II (%)	35.81	34.63	38.56	38.60	32.50	35.27	32.40	31.67
< m-CCD >Region II (μm)	0.76	0.59	0.56	0.56	0.40	0.34	0.38	0.24
CMPI	0.41	0.30	0.27	0.27	0.17	0.16	0.16	0.11

Table 3-2. Student T-test between cell lines in occurrence profile

P value	NIH 3T3	OVCAR-3	SKOV-3	MDA-231	U-2 OS	Swiss 3T3	HF	OSE-10
NIH 3T3	1	< 0.0001	0.0134	0.5931	0.5257	< 0.0001	0.3381	< 0.0001
OVAR-3		1	< 0.0001	< 0.0001	< 0.0001	0.3990	< 0.0001	0.0052
SKOV-3			1	0.0030	0.0026	< 0.0001	0.1658	0.0701
MDA-231				1	0.9126	< 0.0001	0.1459	< 0.0001
U-2 OS					1	< 0.0001	0.1256	< 0.0001
Swiss 3T3						1	< 0.0001	0.0163
HF							1	0.0023
OSE-10								1

CHAPTER 4
FUTURE WORK

A Potential Approach for miRNA Assay

MicroRNAs (or miRNAs) play an important role as a master regulator to the cell. Each type of miRNA utilizes up to 8 of its total ~22 nucleic acids to recognize and bind to the complementary sequence appearing in messenger RNAs (mRNAs) for post-transcriptional regulation. The working mechanism of miRNAs occur at the post-transcriptional level, and the proteins, modulated by a specific type of miRNA via such a mechanism, do not necessarily possess similar functions or co-exist at the same signaling pathway. Hence, miRNAs can simultaneously alter the activities of several different signaling pathways that have no known physical connection. Currently, at least 800 miRNAs have been identified in the human genome (Bentwich et al., 2005).

For example, miR-10b has been reported to promote cancer metastasis, in which cancer cells undergo epithelial-mesenchymal transition (EMT) and migrate to a remote site (Gee et al., 2008). Hence, proteins encoded from the mRNAs that are the post-transcriptional targets of miR-10b have been heavily studied in an attempt to understand their effects on promoting metastasis.

Two of those proteins, HOXD10 and Tiam1, have been separately investigated in breast cancer cells using cell migration (wound healing) and cell invasion assays (Ma et al., 2007; Moriarty et al., 2010). These studies have suggested that the knockdown of HOXD10 increases cell migration speed while that of Tiam1 hinders migration. Hence, these two proteins give rise to opposite effects on miR-10b's role in metastasis and how those effects would join other similar effects from other proteins, of which the mRNAs are the targets of miR-10b, to reach to a collective outcome for metastasis. However,

this result seems to disobey the notion that two or more proteins are regulated by the same mechanism and the same macromolecules, but adopt opposite effects toward the same biological activity to maintain a balanced state for a biological process.

Here we used miR-10b, Tiam1 shRNA and HOXD10 shRNA to examine migration capacity through persistence time and CMPI on NIH 3T3. Following the previous described methods, the results showed both assessments on cell migration are well estimated, with around a 0.97 and 0.90 correlation coefficient to a 10-hour nucleus distance. HOXD10 shRNA and Tiam1 shRNA separately promotes and hinders cell migration capacity. The introduction of miR-10b revealing the slowest migration pattern implied that Tiam1 and HOXD10 may not be the only two downstream signaling proteins of miR-10b. This strategy may suggest a potential approach for studying miRNA.

Pattern Recognition

The distinct subcellular activities in cell migration are all governed by Rho GTPases, but individually with different activity profiles. For example, the trailing edge detachment is mainly governed by RhoA activity with the involvement of microtubules (Kaverina et al., 1999; Rid et al., 2005). Protrusion is a result of all three Rho GTPases activities with precise spatial separation and timing (Machacek et al., 2009). Meanwhile, membrane ruffling is produced mainly by Rac1 and Cdc42 activities. Hence, the changes in the C-N correlation profiles possessed by a cell type can also reveal the changes in the mean activity profile of the Rho GTPases (or that of their pathways) for the cell type. This capacity can reveal the instantaneous changes in the Rho GTPases activity profile for their response to remote extracellular and/or intracellular signal(s) and bypass the complex signaling crosstalk. Hence, the three Rho GTPases might also

serve as an “antennae” to understand the response of a cell to perturbations once the connections between the activity profile of the Rho GTPases and other major cell activities such as cell proliferation and apoptosis are built.

The direct prediction of activity changes in individual Rho GTPases from the redistribution of the C-N correlation data might be not straightforward. The previous example blocking the ROCK activity is easy to understand because the perturbation happens downstream of RhoA. Due to the crosstalk among the Rho GTPases (Cdc42 can activate Rac1 (Nobes and Hall, 1995), and Rac1 and RhoA mutually inhibit each other (Arthur and Burridge, 2001; Nimnual et al., 2003; Ohta et al., 2006; Rottner et al., 1999) and the crosstalk between individual Rho GTPases and other signaling pathways, a upstream signaling event leading to the changes in one of the Rho GTPases will most likely affect its counterparts. Therefore, the resulting changes in the C-N correlation profile from a remote perturbation might not be directly linked to the changes in the activity profile of Rho GTPases.

In order to solve this issue, a pattern recognition approach was adopted. The RhoA, Rac1 and Cdc42 were separately knocked down using specific shRNAs in NIH 3T3 fibroblasts and the corresponding C-N correlation profiles were constructed to compare to that of normal NIH 3T3 fibroblasts (Figure 4-2). The results showed that these manipulations individually possess unique C-N correlation profiles that can be used for “pattern recognition” to identify the changes of individual members of the Rho GTPases.

The “pattern recognition” principles obtained from comparing the redistributed C-N correlation patterns of the individual Rho GTPases’ knockdown to the normal patterns

are: (1) lower Cdc42 activity will shift the distribution of the C-N correlation data from being skewed toward a smaller angle to more symmetry at 90° (a strong Cdc42 activity will make polarity clear with more straightforward directional migration); (2) a higher CCD peak around 90° means weaker the Rac1 activity; and (3) stronger RhoA activity is signified by having more C-N correlation data with larger $NCD_{//}$ value between 10° and 40°.

Application of Pattern Recognition: Rho GTPases Activity under PI3K Inhibitors

Using previous principles, we assessed the C-N correlation profiles of NIH 3T3 fibroblasts with a treatment of 0.1-μM IC87114 and 5-μM Ly294002, which is a specific PI3K p110δ inhibitor and a broad spectrum PI3K inhibitor, respectively (Figure 4-3). The results obtained from the "pattern recognition" suggested that the inhibition of PI3Kδ can decrease the activities of RhoA, Rac1 and Cdc42, while the inhibition of all PI3 Kinases can increase the activity of RhoA and Rac1, but decreases Cdc42. We further probed NIH 3T3 fibroblasts under the same conditions using Western blotting and pull down assays against Rho GTPases (Figure 4-3, right panels). The results validated and confirmed our biophysical analysis. These results are also in agreement with various studies in the literature (Ferreira et al., 2006; Papakonstanti et al., 2007; Polizio et al., 2011). Therefore, our novel approach is an effective method that can bypass the signaling crosstalk and faithfully reflect the changes in the activity profile of Rho GTPases under various and instantaneous perturbations.

The above studies show that analysis thru a C-N correlation profile is a novel and extremely powerful top-down cellular approach, enabling us to tightly link cell migration capacity to the underlying Rho GTPases pathways. In practical cases such as

disease states, the expression level of the three Rho GTPases could be much more complicated. Nevertheless, the C-N correlation profile can link the phenotype and molecular information and facilitate an effective comparison between abnormal cells and the normal counterparts.

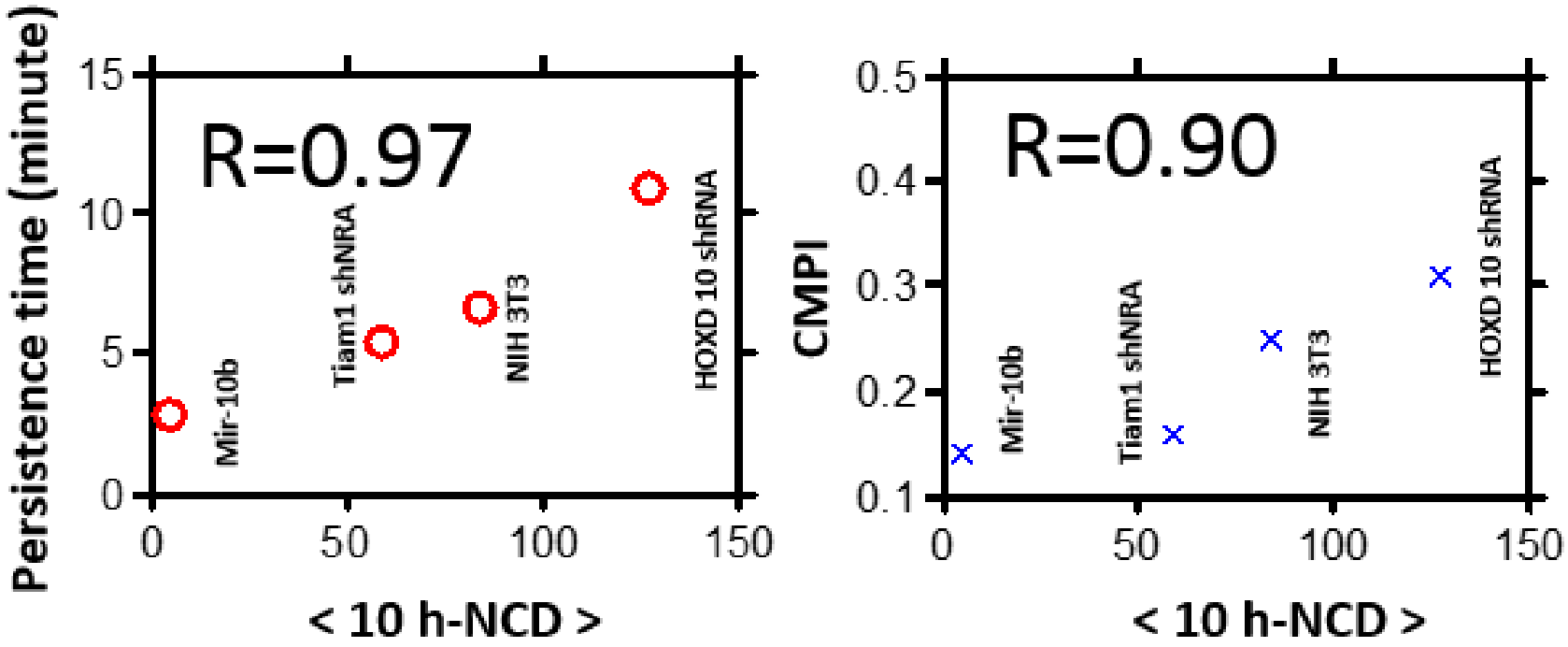

Figure 4-1. The correlation between persistence time or CMPI and 10 hour nucleus distance (<10 h-NCD>). To examine the effect of miR10b and its downstream proteins, HOXD10 and Tiam1, on cell migration, two approaches, persistence time and CMPI, are used to examine the migration capacity. Both estimation on migration capacity show good correlation, 0.97 and 0.9, with the 10 hour nucleus distance. Red circle and blue cross separately represent persistence time (Left) and CMPI (Right). The correlation coefficient (R) is determined by PPMC.

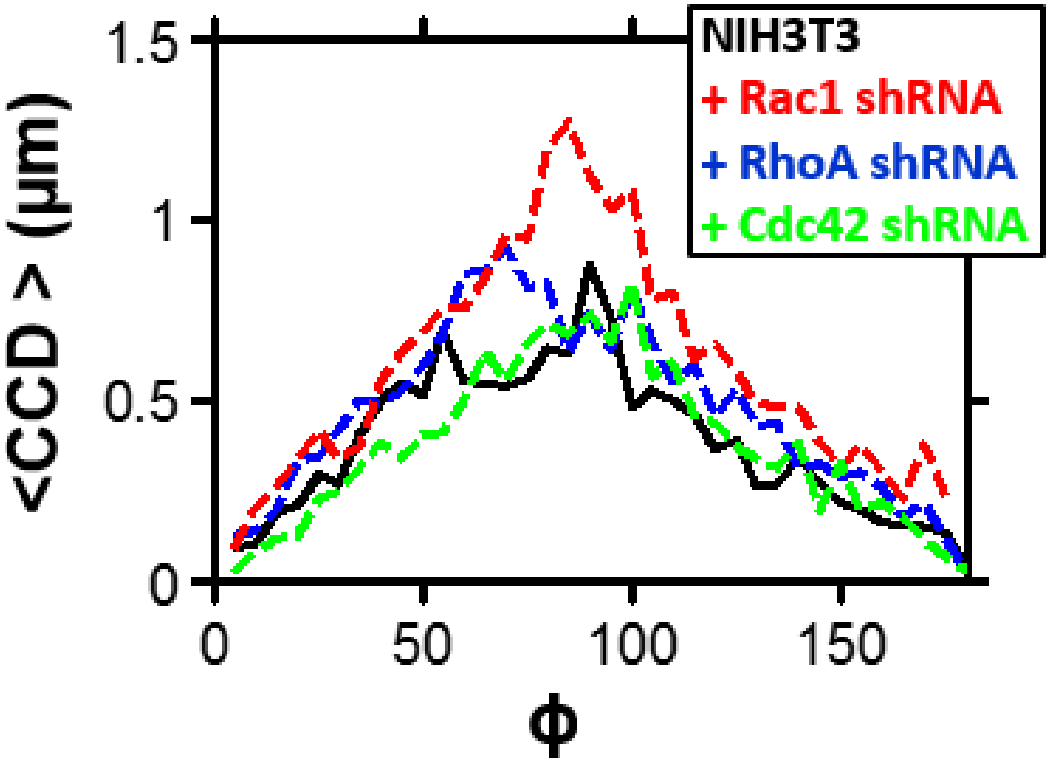

Figure 4-2. Rho GTPases pattern recognition. To eliminating the complexity in signaling pathways, a pattern recognition through Rho GTPases, the nodal proteins in cell migration, may give a clue to solve this issue. NIH 3T3 separately delivered with Rho GTPases shRNAs, including RhoA, Rac1, and Cdc42 shRNAs, was used to examine their single cell migration profile. Black solid line represents the wild type and the red, blue, and green dash lines separately represent the Rac1, RhoA, and Cdc42 shRNAs.

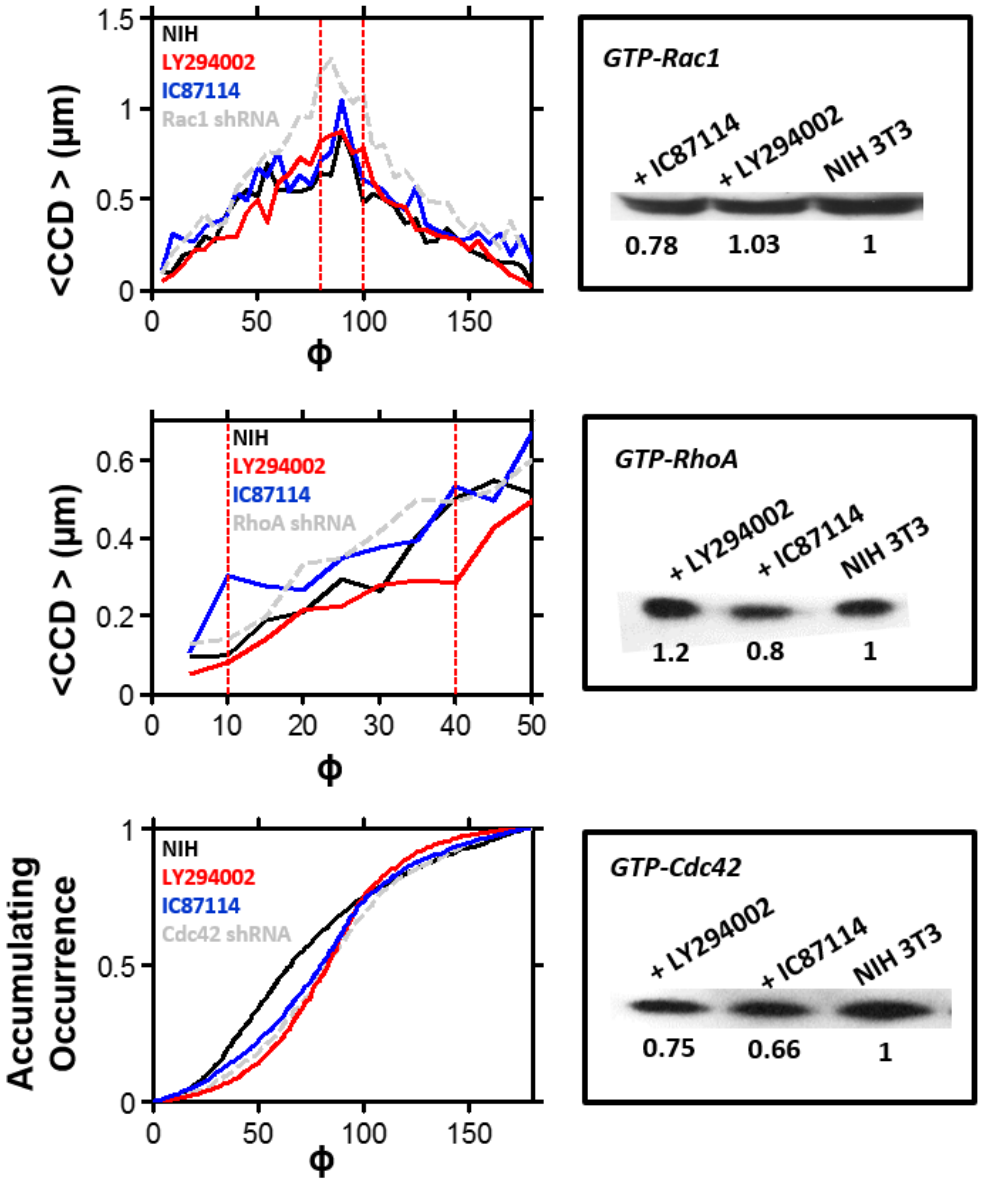

Figure 4-3. Rho GTPases activity estimation through pattern recognition. Through Rho GTPase pattern recognition, the change in Rho GTPase activity by PI3K inhibitor can be reveled through C-N correlation. From the C-N correlation, it shows that lower Rac1 activity has large magnitude around 80°-100° in m-CCD profile (Top panel). This suggests that the IC87114 treated NIH 3T3 has the less Rac1 activity comparing with wild type and Ly294002 treated NIH3T3. For RhoA activity, it also suggested a higher magnitude around 10°-40° in m-CCD profile corresponding to lower RhoA activity (middle panel). This suggests that Ly294002 and IC87114 separately promote and reduced the RhoA activity. For Cdc42 estimation, lower Cdc42 activity will shift the distribution of the C-N correlation data from being skewed toward a smaller angle to more symmetry at 90° (Bottom panel). This suggests that both Ly294002 and IC87114 treated NIH 3T3 show less Cdc42 activity comparing with wild type.

LIST OF REFERENCES

Abercrombie, M., Heaysman, J. E. and Pegrum, S. M. (1970). The locomotion of fibroblasts in culture. 3. Movements of particles on the dorsal surface of the leading lamella. *Exp Cell Res* **62**, 389-98.

Abercrombie, M., Heaysman, J. E. and Pegrum, S. M. (1971). The locomotion of fibroblasts in culture. IV. Electron microscopy of the leading lamella. *Exp Cell Res* **67**, 359-67.

Arthur, W. T. and Burridge, K. (2001). RhoA inactivation by p190RhoGAP regulates cell spreading and migration by promoting membrane protrusion and polarity. *Mol Biol Cell* **12**, 2711-20.

Bacac, M. and Stamenkovic, I. (2008). Metastatic cancer cell. *Annual Review of Pathology-Mechanisms of Disease* **3**, 221-247.

Ballestrem, C., Hinz, B., Imhof, B. A. and Wehrle-Haller, B. (2001). Marching at the front and dragging behind: differential alphaVbeta3-integrin turnover regulates focal adhesion behavior. *J Cell Biol* **155**, 1319-32.

Barriga, E. H., Maxwell, P. H., Reyes, A. E. and Mayor, R. (2013). The hypoxia factor Hif-1α controls neural crest chemotaxis and epithelial to mesenchymal transition. *J Cell Biol* **201**, 759-76.

Bentwich, I., Avniel, A., Karov, Y., Aharonov, R., Gilad, S., Barad, O., Barzilai, A., Einat, P., Einav, U., Meiri, E. et al. (2005). Identification of hundreds of conserved and nonconserved human microRNAs. *Nat Genet* **37**, 766-70.

Bober, E., Franz, T., Arnold, H. H., Gruss, P. and Tremblay, P. (1994). Pax-3 is required for the development of limb muscles: a possible role for the migration of dermomyotomal muscle progenitor cells. *Development* **120**, 603-12.

Buck, C. A. and Horwitz, A. F. (1987). Cell surface receptors for extracellular matrix molecules. *Annu Rev Cell Biol* **3**, 179-205.

Buckley, A., Davidson, J. M., Kamerath, C. D., Wolt, T. B. and Woodward, S. C. (1985). Sustained release of epidermal growth factor accelerates wound repair. *Proc Natl Acad Sci U S A* **82**, 7340-4.

Burridge, K. and Wennerberg, K. (2004). Rho and Rac take center stage. *Cell* **116**, 167-79.

Chen, W. T. (1981a). Mechanism of retraction of the trailing edge during fibroblast movement. *J Cell Biol* **90**, 187-200.

Chen, W. T. (1981b). Surface changes during retraction-induced spreading of fibroblasts. *J Cell Sci* **49**, 1-13.

Crisp, M., Liu, Q., Roux, K., Rattner, J. B., Shanahan, C., Burke, B., Stahl, P. D. and Hodzic, D. (2006). Coupling of the nucleus and cytoplasm: role of the LINC complex. *J Cell Biol* **172**, 41-53.

Dickinson, R. B., McCarthy, J. B. and Tranquillo, R. T. (1993). Quantitative characterization of cell invasion in vitro: formulation and validation of a mathematical model of the collagen gel invasion assay. *Ann Biomed Eng* **21**, 679-97.

DiMilla, P. A., Barbee, K. and Lauffenburger, D. A. (1991). Mathematical model for the effects of adhesion and mechanics on cell migration speed. *Biophys J* **60**, 15-37.

Dunn, G. A. (1983). Characterising a kinesis response: time averaged measures of cell speed and directional persistence. *Agents Actions Suppl* **12**, 14-33.

Dunn, G. A. and Brown, A. F. (1987). A unified approach to analysing cell motility. *J Cell Sci Suppl* **8**, 81-102.

Ellard, K., Sunose, M., Bell, K., Ramsden, N., Bergamini, G. and Neubauer, G. (2012). Discovery of novel PI3Kγ/δ inhibitors as potential agents for inflammation. *Bioorg Med Chem Lett* **22**, 4546-9.

Ferreira, A. M., Isaacs, H., Hayflick, J. S., Rogers, K. A. and Sandig, M. (2006). The p110delta isoform of PI3K differentially regulates beta1 and beta2 integrin-mediated monocyte adhesion and spreading and modulates diapedesis. *Microcirculation* **13**, 439-56.

Gail, M. H. and Boone, C. W. (1970). The locomotion of mouse fibroblasts in tissue culture. *Biophys J* **10**, 980-93.

Gee, H. E., Camps, C., Buffa, F. M., Colella, S., Sheldon, H., Gleadle, J. M., Ragoussis, J. and Harris, A. L. (2008). MicroRNA-10b and breast cancer metastasis. *Nature* **455**, E8-9; author reply E9.

Ghigo, A., Damilano, F., Braccini, L. and Hirsch, E. (2010). PI3K inhibition in inflammation: Toward tailored therapies for specific diseases. *Bioessays* **32**, 185-96.

Gimona, M. (2008). The microfilament system in the formation of invasive adhesions. *Semin Cancer Biol* **18**, 23-34.

Gomes, E. R., Jani, S. and Gundersen, G. G. (2005). Nuclear movement regulated by Cdc42, MRCK, myosin, and actin flow establishes MTOC polarization in migrating cells. *Cell* **121**, 451-63.

Greenhalgh, D. G. (1996). The role of growth factors in wound healing. *J Trauma* **41**, 159-67.

Grose, R., Werner, S., Kessler, D., Tuckermann, J., Huggel, K., Durka, S. and Reichardt, H. M. (2002). A role for endogenous glucocorticoids in wound repair. *EMBO Rep* **3**, 575-82.

Gu, J., Tamura, M., Pankov, R., Danen, E. H., Takino, T., Matsumoto, K. and Yamada, K. M. (1999). Shc and FAK differentially regulate cell motility and directionality modulated by PTEN. *J Cell Biol* **146**, 389-403.

Hall, A. (1998). Rho GTPases and the actin cytoskeleton. *Science* **279**, 509-14.

Heasman, S. J. and Ridley, A. J. (2008). Mammalian Rho GTPases: new insights into their functions from in vivo studies. *Nat Rev Mol Cell Biol* **9**, 690-701.

Huttenlocher, A., Sandborg, R. R. and Horwitz, A. F. (1995). Adhesion in cell migration. *Curr Opin Cell Biol* **7**, 697-706.

Jones, G. E. (2000). Cellular signaling in macrophage migration and chemotaxis. *J Leukoc Biol* **68**, 593-602.

Kaverina, I., Krylyshkina, O. and Small, J. V. (1999). Microtubule targeting of substrate contacts promotes their relaxation and dissociation. *J Cell Biol* **146**, 1033-44.

Kaverina, I., Krylyshkina, O. and Small, J. V. (2002). Regulation of substrate adhesion dynamics during cell motility. *Int J Biochem Cell Biol* **34**, 746-61.

Khatau, S. B., Hale, C. M., Stewart-Hutchinson, P. J., Patel, M. S., Stewart, C. L., Searson, P. C., Hodzic, D. and Wirtz, D. (2009). A perinuclear actin cap regulates nuclear shape. *Proc Natl Acad Sci U S A* **106**, 19017-22.

Kim, Y. J., Sauer, C., Testa, K., Wahl, J. K., Svoboda, R. A., Johnson, K. R., Wheelock, M. J. and Knudsen, K. A. (2005). Modulating the strength of cadherin adhesion: evidence for a novel adhesion complex. *J Cell Sci* **118**, 3883-94.

Kurosaka, S. and Kashina, A. (2008). Cell biology of embryonic migration. *Birth Defects Res C Embryo Today* **84**, 102-22.

Lauffenburger, D. A. and Horwitz, A. F. (1996). Cell migration: a physically integrated molecular process. *Cell* **84**, 359-69.

Lee, H., Goetzl, E. J. and An, S. (2000). Lysophosphatidic acid and sphingosine 1-phosphate stimulate endothelial cell wound healing. *Am J Physiol Cell Physiol* **278**, C612-8.

Lee, J. S., Chang, M. I., Tseng, Y. and Wirtz, D. (2005). Cdc42 mediates nucleus movement and MTOC polarization in Swiss 3T3 fibroblasts under mechanical shear stress. *Mol Biol Cell* **16**, 871-80.

Li, L., Nørrelykke, S. F. and Cox, E. C. (2008). Persistent cell motion in the absence of external signals: a search strategy for eukaryotic cells. *PLoS One* **3**, e2093.

Lipton, A., Klinger, I., Paul, D. and Holley, R. W. (1971). Migration of mouse 3T3 fibroblasts in response to a serum factor. *Proc Natl Acad Sci U S A* **68**, 2799-801.

Luxton, G. W., Gomes, E. R., Folker, E. S., Vintinner, E. and Gundersen, G. G. (2010). Linear arrays of nuclear envelope proteins harness retrograde actin flow for nuclear movement. *Science* **329**, 956-9.

Lynch, S. E., Colvin, R. B. and Antoniades, H. N. (1989). Growth factors in wound healing. Single and synergistic effects on partial thickness porcine skin wounds. *J Clin Invest* **84**, 640-6.

Lynch, S. E., Nixon, J. C., Colvin, R. B. and Antoniades, H. N. (1987). Role of platelet-derived growth factor in wound healing: synergistic effects with other growth factors. *Proc Natl Acad Sci U S A* **84**, 7696-700.

Ma, L., Teruya-Feldstein, J. and Weinberg, R. A. (2007). Tumour invasion and metastasis initiated by microRNA-10b in breast cancer. *Nature* **449**, 682-8.

MacDonald, I. C., Groom, A. C. and Chambers, A. F. (2002). Cancer spread and micrometastasis development: quantitative approaches for in vivo models. *Bioessays* **24**, 885-93.

Machacek, M., Hodgson, L., Welch, C., Elliott, H., Pertz, O., Nalbant, P., Abell, A., Johnson, G. L., Hahn, K. M. and Danuser, G. (2009). Coordination of Rho GTPase activities during cell protrusion. *Nature* **461**, 99-103.

Martin, P. and Parkhurst, S. (2004). Parallels between tissue repair and embryo morphogenesis. *Development* **131**, 3021-3034.

Mizoguchi, T., Verkade, H., Heath, J. K., Kuroiwa, A. and Kikuchi, Y. (2008). Sdf1/Cxcr4 signaling controls the dorsal migration of endodermal cells during zebrafish gastrulation. *Development* **135**, 2521-9.

Moriarty, C. H., Pursell, B. and Mercurio, A. M. (2010). miR-10b targets Tiam1: implications for Rac activation and carcinoma migration. *J Biol Chem* **285**, 20541-6.

Mullins, R. D., Heuser, J. A. and Pollard, T. D. (1998). The interaction of Arp2/3 complex with actin: nucleation, high affinity pointed end capping, and formation of branching networks of filaments. *Proc Natl Acad Sci U S A* **95**, 6181-6.

Nagel, M., Tahinci, E., Symes, K. and Winklbauer, R. (2004). Guidance of mesoderm cell migration in the Xenopus gastrula requires PDGF signaling. *Development* **131**, 2727-36.

Nath, C. and Gulati, S. C. (1998). Role of cytokines in healing chronic skin wounds. *Acta Haematol* **99**, 175-9.

Nimnual, A. S., Taylor, L. J. and Bar-Sagi, D. (2003). Redox-dependent downregulation of Rho by Rac. *Nat Cell Biol* **5**, 236-41.

Nobes, C. D. and Hall, A. (1995). Rho, rac, and cdc42 GTPases regulate the assembly of multimolecular focal complexes associated with actin stress fibers, lamellipodia, and filopodia. *Cell* **81**, 53-62.

Ohta, Y., Hartwig, J. H. and Stossel, T. P. (2006). FilGAP, a Rho- and ROCK-regulated GAP for Rac binds filamin A to control actin remodelling. *Nat Cell Biol* **8**, 803-14.

Oliver, T., Lee, J. and Jacobson, K. (1994). Forces exerted by locomoting cells. *Semin Cell Biol* **5**, 139-47.

Omelchenko, T., Vasiliev, J. M., Gelfand, I. M., Feder, H. H. and Bonder, E. M. (2002). Mechanisms of polarization of the shape of fibroblasts and epitheliocytes: Separation of the roles of microtubules and Rho-dependent actin-myosin contractility. *Proc Natl Acad Sci U S A* **99**, 10452-7.

Othmer, H. G., Dunbar, S. R. and Alt, W. (1988). Models of dispersal in biological systems. *J Math Biol* **26**, 263-98.

Palecek, S. P., Huttenlocher, A., Horwitz, A. F. and Lauffenburger, D. A. (1998). Physical and biochemical regulation of integrin release during rear detachment of migrating cells. *J Cell Sci* **111 (Pt 7)**, 929-40.

Pankov, R., Endo, Y., Even-Ram, S., Araki, M., Clark, K., Cukierman, E., Matsumoto, K. and Yamada, K. M. (2005). A Rac switch regulates random versus directionally persistent cell migration. *J Cell Biol* **170**, 793-802.

Panorchan, P., Thompson, M. S., Davis, K. J., Tseng, Y., Konstantopoulos, K. and Wirtz, D. (2006). Single-molecule analysis of cadherin-mediated cell-cell adhesion. *J Cell Sci* **119**, 66-74.

Papakonstanti, E. A., Ridley, A. J. and Vanhaesebroeck, B. (2007). The p110delta isoform of PI 3-kinase negatively controls RhoA and PTEN. *EMBO J* **26**, 3050-61.

Polizio, A. H., Chinchilla, P., Chen, X., Kim, S., Manning, D. R. and Riobo, N. A. (2011). Heterotrimeric Gi proteins link Hedgehog signaling to activation of Rho small GTPases to promote fibroblast migration. *J Biol Chem* **286**, 19589-96.

Ren, X. D., Kiosses, W. B. and Schwartz, M. A. (1999). Regulation of the small GTP-binding protein Rho by cell adhesion and the cytoskeleton. *EMBO J* **18**, 578-85.

Richardson, B. and Lehmann, R. (2010). Mechanisms guiding primordial germ cell migration: strategies from different organisms. *Nature Reviews Molecular Cell Biology* **11**, 37-49.

Rid, R., Schiefermeier, N., Grigoriev, I., Small, J. V. and Kaverina, I. (2005). The last but not the least: the origin and significance of trailing adhesions in fibroblastic cells. *Cell Motil Cytoskeleton* **61**, 161-71.

Ridley, A. J. and Hall, A. (1992). The small GTP-binding protein rho regulates the assembly of focal adhesions and actin stress fibers in response to growth factors. *Cell* **70**, 389-99.

Ridley, A. J., Paterson, H. F., Johnston, C. L., Diekmann, D. and Hall, A. (1992). The small GTP-binding protein rac regulates growth factor-induced membrane ruffling. *Cell* **70**, 401-10.

Rottner, K., Hall, A. and Small, J. V. (1999). Interplay between Rac and Rho in the control of substrate contact dynamics. *Curr Biol* **9**, 640-8.

Sahai, E. and Marshall, C. J. (2003). Differing modes of tumour cell invasion have distinct requirements for Rho/ROCK signalling and extracellular proteolysis. *Nat Cell Biol* **5**, 711-9.

Sander, E. E., ten Klooster, J. P., van Delft, S., van der Kammen, R. A. and Collard, J. G. (1999). Rac downregulates Rho activity: reciprocal balance between both GTPases determines cellular morphology and migratory behavior. *J Cell Biol* **147**, 1009-22.

Sanz-Moreno, V., Gadea, G., Ahn, J., Paterson, H., Marra, P., Pinner, S., Sahai, E. and Marshall, C. J. (2008). Rac activation and inactivation control plasticity of tumor cell movement. *Cell* **135**, 510-23.

Schmidt, C. E., Horwitz, A. F., Lauffenburger, D. A. and Sheetz, M. P. (1993). Integrin-cytoskeletal interactions in migrating fibroblasts are dynamic, asymmetric, and regulated. *J Cell Biol* **123**, 977-91.

Scita, G., Tenca, P., Frittoli, E., Tocchetti, A., Innocenti, M., Giardina, G. and Di Fiore, P. P. (2000). Signaling from Ras to Rac and beyond: not just a matter of GEFs. *Embo J* **19**, 2393-8.

Small, J. V., Rottner, K. and Kaverina, I. (1999). Functional design in the actin cytoskeleton. *Curr Opin Cell Biol* **11**, 54-60.

Stokes, C. L., Lauffenburger, D. A. and Williams, S. K. (1991). Migration of individual microvessel endothelial cells: stochastic model and parameter measurement. *J Cell Sci* **99 (Pt 2)**, 419-30.

Suraneni, P., Rubinstein, B., Unruh, J. R., Durnin, M., Hanein, D. and Li, R. (2012). The Arp2/3 complex is required for lamellipodia extension and directional fibroblast cell migration. *J Cell Biol* **197**, 239-51.

Swartz, M. E., Eberhart, J., Pasquale, E. B. and Krull, C. E. (2001). EphA4/ephrin-A5 interactions in muscle precursor cell migration in the avian forelimb. *Development* **128**, 4669-80.

Tamkun, J. W., DeSimone, D. W., Fonda, D., Patel, R. S., Buck, C., Horwitz, A. F. and Hynes, R. O. (1986). Structure of integrin, a glycoprotein involved in the transmembrane linkage between fibronectin and actin. *Cell* **46**, 271-82.

Theriot, J. A. (1994). Regulation of the actin cytoskeleton in living cells. *Semin Cell Biol* **5**, 193-9.

Todaro, G. J., Lazar, G. K. and Green, H. (1965). The initiation of cell division in a contact-inhibited mammalian cell line. *J Cell Physiol* **66**, 325-33.

Tonami, K., Kurihara, Y., Arima, S., Nishiyama, K., Uchijima, Y., Asano, T., Sorimachi, H. and Kurihara, H. (2011). Calpain-6, a microtubule-stabilizing protein, regulates Rac1 activity and cell motility through interaction with GEF-H1. *J Cell Sci* **124**, 1214-23.

Uehata, M., Ishizaki, T., Satoh, H., Ono, T., Kawahara, T., Morishita, T., Tamakawa, H., Yamagami, K., Inui, J., Maekawa, M. et al. (1997). Calcium sensitization of smooth muscle mediated by a Rho-associated protein kinase in hypertension. *Nature* **389**, 990-4.

van Leeuwen, F. N., van Delft, S., Kain, H. E., van der Kammen, R. A. and Collard, J. G. (1999). Rac regulates phosphorylation of the myosin-II heavy chain, actinomyosin disassembly and cell spreading. *Nat Cell Biol* **1**, 242-8.

Winklbauer, R. (1990). Mesodermal cell migration during Xenopus gastrulation. *Dev Biol* **142**, 155-68.

Witt, C. M., Raychaudhuri, S., Schaefer, B., Chakraborty, A. K. and Robey, E. A. (2005). Directed migration of positively selected thymocytes visualized in real time. *PLoS Biol* **3**, e160.

Wolf-Yadlin, A., Kumar, N., Zhang, Y., Hautaniemi, S., Zaman, M., Kim, H. D., Grantcharova, V., Lauffenburger, D. A. and White, F. M. (2006). Effects of HER2 overexpression on cell signaling networks governing proliferation and migration. *Mol Syst Biol* **2**, 54.

Wolf, K., Mazo, I., Leung, H., Engelke, K., von Andrian, U. H., Deryugina, E. I., Strongin, A. Y., Bröcker, E. B. and Friedl, P. (2003). Compensation mechanism in tumor cell migration: mesenchymal-amoeboid transition after blocking of pericellular proteolysis. *J Cell Biol* **160**, 267-77.

Woo, S., Housley, M. P., Weiner, O. D. and Stainier, D. Y. (2012). Nodal signaling regulates endodermal cell motility and actin dynamics via Rac1 and Prex1. *J Cell Biol* **198**, 941-52.

Yamazaki, D., Kurisu, S. and Takenawa, T. (2009). Involvement of Rac and Rho signaling in cancer cell motility in 3D substrates. *Oncogene* **28**, 1570-83.

Yoshida, K. and Soldati, T. (2006). Dissection of amoeboid movement into two mechanically distinct modes. *J Cell Sci* **119**, 3833-44.

Yoshizaki, H., Ohba, Y., Kurokawa, K., Itoh, R. E., Nakamura, T., Mochizuki, N., Nagashima, K. and Matsuda, M. (2003). Activity of Rho-family GTPases during cell division as visualized with FRET-based probes. *J Cell Biol* **162**, 223-32.

Zhang, J., Xu, X. K., Li, P., Zhang, K. and Small, M. (2011). Node importance for dynamical process on networks: A multiscale characterization. *Chaos* **21**, 016107.

BIOGRAPHICAL SKETCH

Shen-Hsiu was born in 1980 in Taipei, Taiwan. He is senior in his family with two younger sisters. After graduating from Yanping high school in 1998, he entered Chemical Engineering Department, National Chung Hsing University (NCHU). He earned his B.S. in 2002, and study graduate program, Chemical Engineering, in National Cheng Kung University (NCKU) from 2002 to 2004. Later, he served as second lieutenant in Taiwan Army Artillery and Missile School and had teaching assistant position in NCKU till 2007.

In 2007 fall, he enrolled in the Master program in the Department of Chemical Engineering at University of Florida. He joined Dr. Yiider Tseng's research group and focused on cellular biophysical approach from 2009-2013. He earned his Doctor of Philosophy degree in chemical engineering in August 2013.